Design of an Aerobatics Air Race Aircraft

Design a light, manoeuvrable, fast and customisable aerobatics aircraft to compete in the Red Bull Air Race World Championship.

J.A.P. Borst	4088239	P. Poudel	4094352
M.L. Hoogendoorn	4103963	S. Sachdeva	4092805
J. Kaminski	4171004	J. Spans	4170113
S.B. Latooij	1396951	S. Tandon	4160975
M.J. van der Lelij	4139062	J.A. Tuitert	4083652

Final Report

Design Synthesis Excercise

TU Delft Delft University of Technology

Aerospace Engineering

July 1, 2014

[This page is intentionally left blank]

Revision Index

Revision Number	Pages Affected	Description	Date
v0.8	All pages	First draft	12/06/2014
v0.9	All Pages	Second draft	20/06/2014
v1.0	All Pages	Final version	01/07/2014

Preface

This document is the final technical report of the design synthesis exercise 'Design of an aerobatic air race aircraft'. This report discusses the aircraft conceptual design of Avinya and serves to provide the principal tutor, coaches, clients, members of the faculty, and other interested parties with a formal briefing on the progress of the project. On the 22^{nd} of April 2014, group 13 received the exercise to 'Design a light, manoeuvrable, fast and customisable aerobatics aircraft to compete in the Red Bull Air Race World Championship'. As the project evolved, the mission need statement was adapted in agreement with the client to: 'Design a lightweight and customisable aerobatic race aircraft with performance characteristics that exceed those of current competitors.' Avinya, a word from Pali language used 2500 years ago, means to achieve the miraculous or extraordinary which cannot be achieved by ordinary intelligence or perception. Therefore, it fits our mission need statement.

Readers interested in the design process of the Avinya aircraft are referred to part I in which the requirements, constraints, final concept description and interaction of the technical departments are provided. The resource allocation and budget breakdown are discussed as well. Those interested in the details within the technical design process are referred to part II, which is subdivided in firstly a trajectory optimisation and sensitivity analysis and secondly a performance analysis. Subsequently, the aerodynamics, stability, control and structural analysis are performed. And lastly, all results leading to the detailed design are summarised and discussed. Finally, in part III, all project components associated with future development, such as requirement and feasibility analysis, manufacturing and assembly plan, project planning, RAMS, sustainability and technical risk are stated. Concluding this technical report, and with it the Design Synthesis Exercise and the Avinya project, the conclusion and recommendations on this project are provided.

Our team would like to thank our tutor Paul Roling and our coaches Sander Hartjes and Kristofer Jovanov for their guidance on various aspects of the Avinya project and feedback on the project process. We would also like to thank Christos Kassapoglou, Martin Orlita, Roland van Gent, Sonell Shroff, Dario Costa and Roelof Vos for their time and advice. Also we would like to thank Peter Wezenbeek for the provision of air race track details and his view on overall performance of aerobatic race aircraft. Furthermore we would like to thank the Delft University of Technology for providing us with the resources to perform the research and document our findings. The design synthesis project was a great learning experience with respect to both project management and engineering skills.

Contents

Nomenclature

Symbol	Description	Unit
b	Wing span	m
$\bar{c}$	Mean aerodynamic chord	m
c_r	Root chord	m
c_t	Tip chord	m
C_D	Drag coefficient	-
C_{D_0}	Zero lift drag coefficient	-
C_D	Induced drag coefficient	-
CFD	Computational fluid dynamics	-
C_{fe}	Friction coefficient	-
c.g.	Center of gravity	-
$C_{l_{d\alpha}}$	Aileron authority	-
$c_{l_{d\alpha}}$	Airfoil lift coefficient change due to δ_α	-
C_{l_β}	Roll moment coefficient due to sideslip	-
A	Aspect ratio	-
C_L	Lift coefficient	-
C_{L_h}	Horizontal tail lift coefficient	-
$C_{L_{max}}$	Maximum lift coefficient	-
C_{L_α}	Lift gradient	-
$C_{L_{\alpha_h}}$	Horizontal tail lift gradient	-
C_m	Pitching moment coefficient	-
$C_{m_{ac}}$	Aerodynamic centre moment coefficient	-
D_{rod}	Diameter of a rod	mm
DSE	Design synthesis exercise	-
EW	Empty weight	kg
f	Ratio W_L/W_{TO}	-
f_{h_f}	Fraction of fuselage height	-
f_{l_f}	Fraction of fuselage length	-
f_{w_f}	Fraction of fuselage width	-
FAA	Federal aviation administration	-
FBS	Functional breakdown structure	-
FFD	Functional flow diagram	-
G	Climb gradient	%
g	Gravitational constant	9.81 m/s^2
HDG	Heading	$^\circ$
h_{f_s}	Height of fuselage structure	mm
I_{yy}	Mass moment of inertia around y-axis	kgm^2
L_{f_s}	Length of fuselage structure	mm
l	Length of a general rod	m
l_h	Tail length	m
M	Mach number	-
MMOI	Mass moment of inertia	-
m_{struc}	Mass of the fuselage structure	kg
MTOW	Maximum take-off weight	kg
M_y	Moment around y-axis	Nm

Symbol	Description	Unit
n	Load factor	-
n_{max}	Maximum load factor	-
q	Pitch rate	$^\circ/s$
$\dot{q}$	Pitch acceleration	$^\circ/s^2$
R	Distance used for induced downwash	-
RAMS	Reliability, Availability, Maintainability and Safety	-
RBAR	Red Bull Air Race	-
ROC	Rate of climb	m/s
p	Roll rate	deg/s
P	Power	W
S	Surface area	m^2
S_h	Horizontal tail surface area	m^2
s_l	Landing distance	m
S.M.	Stability margin	-
S_{wet}	Wetted surface area	m^2
$T_c^{'}$	Thrust coefficient	[-]
TOP_{prop}	Take-off parameter	lb^2/ft^2hp
V	Air speed	kts
V_c	Cruise speed	kts
V_d	Dive speed	kts
$\frac{V_h}{V}$	Tail-wing airspeed ratio	-
V_m	Manoeuvre speed	kts
V_{ne}	Speed never exceed	kts
V_s	Stall speed	m/s
$V_{s_{land}}$	Landing speed	m/s
WFD	Work flow diagram	
w_{f_s}	Width of fuselage structure	mm
WBS	Work breakdown structure	
W_{TO}	Take-off weight	kg
$\frac{W}{S}$	Wing loading	N/m^2
$\bar{x}_{cg}$	Centre of gravity location	-
$\bar{x}_{ac}$	Aerodynamic centre location	-
$\frac{d\varepsilon}{d\alpha}$	Downwash gradient	-
$\frac{t}{c}$	airfoil thickness	-
γ	Flight path angle	rad
δ_a	Aileron deflection	$^\circ$
η	Throttle settings	-
η_p	Propeller efficiency	-
λ	Taper ratio	-
Λ	Sweep	$^\circ$
μ	Roll angle	rad
σ	Density ratio	-
ρ	Air density	kg/m^3
τ	Aileron effectiveness parameter	-
ϕ	Bank angle	rad
χ	Heading angle	rad

Summary

In order to design an aircraft capable of dominating the RBAR competition, the project statement was defined as: *Design a customisable aerobatic race aircraft, to win the Red Bull Air Race (RBAR) competition, by ten students within eleven weeks*. This resulted in a mission need statement: *Design a lightweight and customisable aerobatic aircraft with performance characteristics that exceed those of current competitors*.

In this, the final technical report, the Avinya concept's dimensions, performance characteristics and stability/controllability parameters are presented. Furthermore renderings of the 3D concept as well as technical drawings are provided to further illustrate the entire concept. In addition two wing planforms are incorporated into the aircraft and are part of the customisable and modular aspect of this design. Wing 1 is optimised for roll rate whereas wing 2 is optimised for aerodynamic efficiency and rate of climb. Due to the fact that these optimisations have contrasting geometrical requirements, the increase in aerodynamic efficiency and R.O.C. of wing 2 is at the expense of the roll rate. The performance characteristics of the aircraft with both wings, compared to those set by the client and competition are compared below in Table 2 in addition an illustrative sketch showing the geometrical differences is also provided in Fig. 1

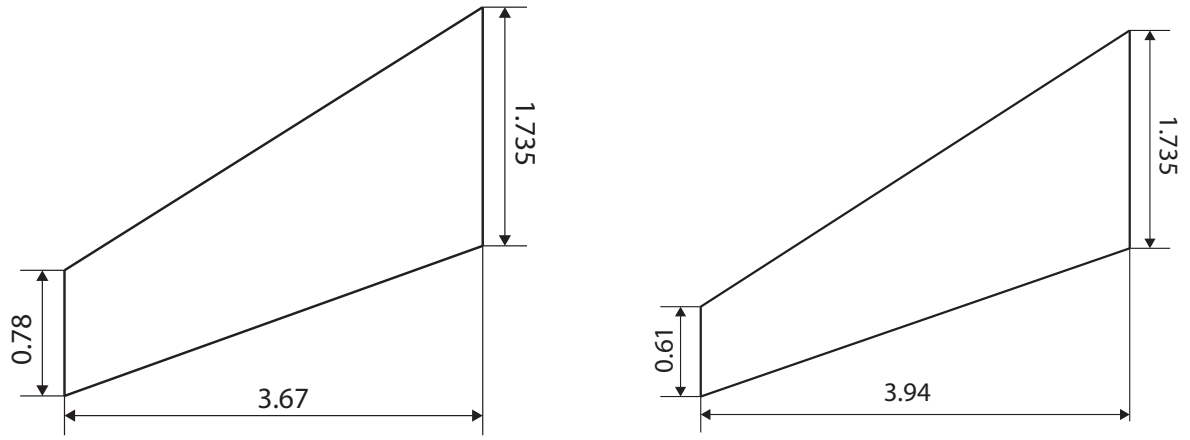

(a) Wing 1 **(b) Wing 2**

Figure 1: Sketch of wing 1 and wing 2, not to scale

As can be seen from Table 2 the concept equipped with wing 1 meets all the performance requirements whereas wing 2, which achieves a higher climb rate, does so at the expense of roll rate. The result is that the two wings can be interchanged on the aircraft to suit the track that is being flown. Thus for tighter tracks such as Abu Dhabi wing 1 (optimised for roll rate) achieves a better time than wing 2 which is optimised for rate of climb. Vice versa wing 2 excels at flying the sample track which has more straight sections and climbing manoeuvres such as the half-cuban eight. A summary of the actual times obtained are provided in Table 4

Table 2: Requirement compliance matrix

Requirement	Value	Wing 1	Wing 2
Maximum speed	$>$ 230kts	✓	✓
Maximum rate of climb	$>$ 4700 ft/min	✓	✓
Maximum roll rate	$>420^{\circ}$/s	✓	×
Maximum load factor	$\pm$10g	✓	✓
Empty mass	$<$ 700kg	✓	✓
Empty mass	$>$ 540kg	✓	✓
Race mass	$>$ 698kg	✓	✓
Stall speed	$<$ 61 kts	✓	✓
Take-off distance	$<$ 500m	✓	✓
Landing distance	$<$ 500m	✓	✓
Wing span	$7-8.5$m	✓	✓

The specific numerical values for the Avinya are shown below in Table 3:

Table 3: Parameters and performance characteristics of the final design

Parameter	Wing 1	Wing 2	Unit
OEW	560	567	kg
$MTOW$	708	715	kg
S_c	1.8	1.8	m^2
S	9.23	9.23	m^2
b	7.34	7.88	m
A	5.84	6.73	-
c_r	1.74	1.74	m
λ	0.45	0.36	-
p	420	398	$^{\circ}/s$
ROC	24.7	25.0	m/s
q	93.8	94.2	$^{\circ}/s$

Table 4: Results of two designed wings on two separate tracks

Wing	Track	Total time [sec]
Wing 1	Sample	29.6989
Wing 2	Sample	**29.4795**
Wing 1	Abu Dhabi	**24.1683**
Wing 2	Abu Dhabi	24.4462

The structural aspects of the aircraft are also analysed in more detail with a stress analysis conducted on the wing and the fuselage in order to size wingbox and internal truss structures for the aircraft. These stresses were verified and where possible validation data based on wing stress tests was used to validate the software. The subsequent wingbox and truss structure sizes are presented below, in Table 5.

Table 5: Dimensions, weight and cost of the wingbox structures

	Wing 1	Wing 2	Canard
Dimension	At root [mm]		
t_f	12.0	14.5	10.3
t_r	6.90	9.50	8.73
t_t	5.90	6.20	5.55
t_b	5.90	6.20	5.55
w_{root}	650	644	214
h_{root}	193	191	63.5
η	-37.4	-25.9	-3.56
ξ	0.00	0.00	0.00
X	-28.3	-24.1	-3.01
Z	0.00	0.00	0.00
$W_{wingbox}$ [kg]	41.2	44.4	9.55
$Cost_{wingbox}$ [€]	1281.81	1380.08	296.96

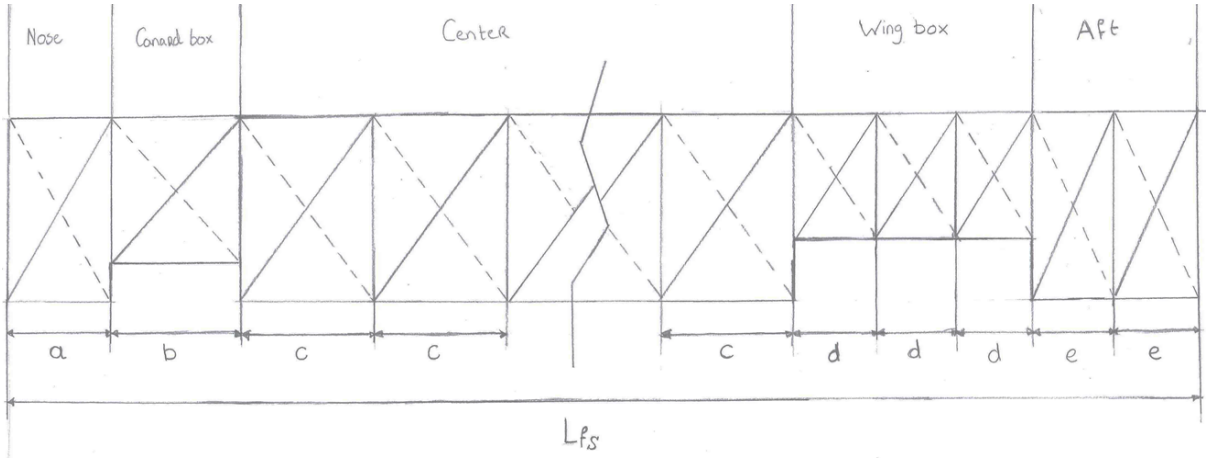

Figure 2: Drawing of the preliminary truss structure with the five parts indicated on the top

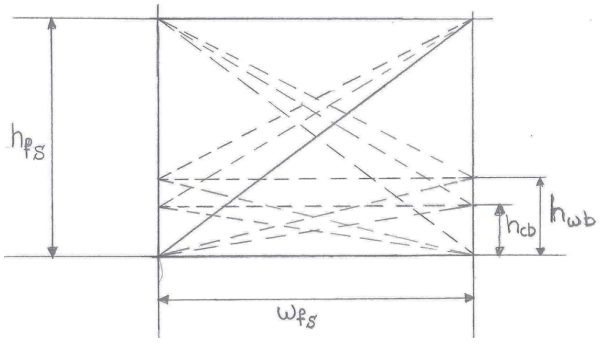

Figure 3: Drawing of the preliminary truss structure front view

Table 6: Main dimensions of the fuselage truss structure

Dimension	Value [mm]
h_{cb}	90.0
h_{wb}	196
h_{f_s}	540
w_{f_s}	600
L_{f_s}	4505
D_{rod}	11.0

With the stress analysis and dimensions of main structural components now known, the design itself can be discussed. The Avinya features a canard with an elevator in the front, followed by a sweptback main wing with

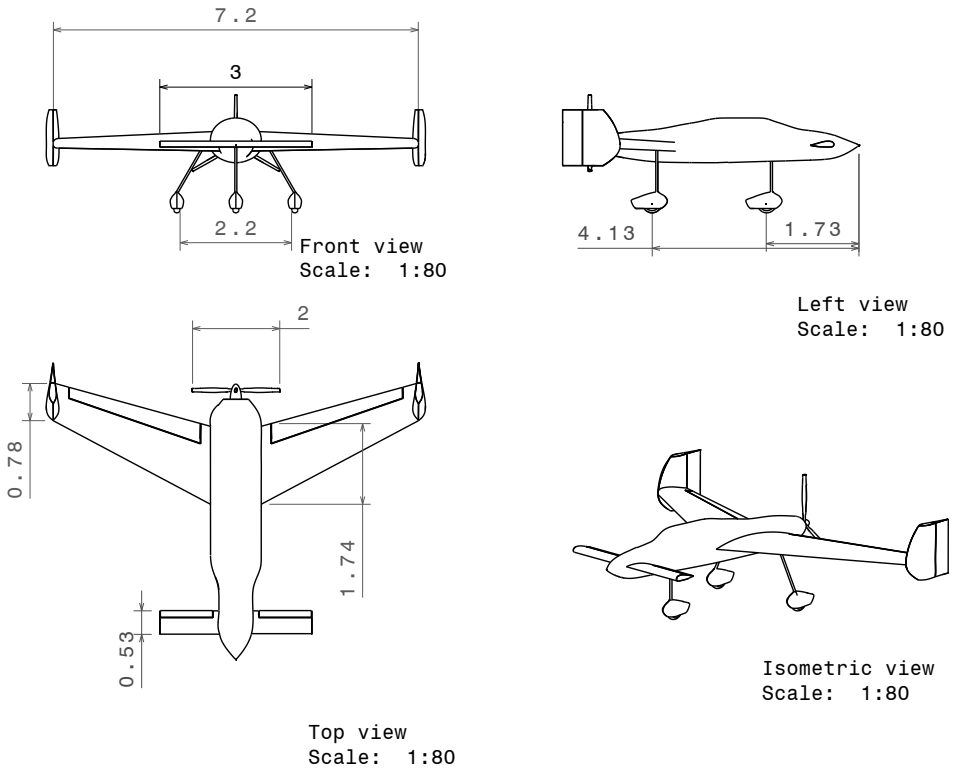

Figure 4: Technical drawing of final aircraft design

vertical tails mounted at the wingtips and a pusher propeller at the rear. The propeller is powered by a piston engine, which is standardised as per the RBAR regulations. The aircraft structure consists of a steel tubular space frame, while the skin and wings are made from carbon fibre composites. The approximate weight of the fuselage structure is equal to 71.6 kg, whereas the weight of the wingbox is estimated to be 43.7 kg. Avinya features a fixed tricycle landing gear with a nose wheel and aerodynamic fairings to reduce parasite drag.

The concept itself is presented below with 3D renderings and 2D technical drawings which outline the dimensions of the aircraft.

(a) Front view

(b) Back view

Figure 5: Front and back view renders of the final aircraft design

With the relevant sizing and performance parameters of the concept outlined, the report proceeds to discuss the future work to be undertaken as well as the sustainability considerations with regards to manufacturing, operations and end of life disposal. In particular a detailed manufacturing plan needs to be made which would then consist of all components, including nuts and bolts and joining methods - something which is beyond the scope of this project. Furthermore testing (a scale model) of the aircraft in a wind tunnel as well as structural testing in order to determine stability coefficients, lift distributions and limit loads will provide more accurate details of the aircraft's performance as well as validate the tools currently used to generate the concept. In terms of sustainability the manufacturing facilities and methods need to be carefully chosen to minimise pollution particularly since carbon fibre is applied throughout the structure and the associated processing of, for example, CFRP is particularly pollutive. In addition to this, preliminary analysis shows that an electric engine can be integrated into the aircraft without modification to the current structure. This requires further detailed research to determine what regulations would apply and how much endurance the batteries would have to provide for the competition. Another facet that can be made more sustainable in the entire RBAR would be to implement a water vapour or biodiesel based smoke generation system. The water vapour in particular would need extensive research and development given that no such system currently exists which is capable of delivering the amount of smoke required. Finally the end of life disposal seems promising, metal components are the easiest to recycle, whilst carbon fibre is much more difficult, even though methods are being developed and optimised that allow greater fibre percentage recovery and fibres of a higher quality.

Chapter 1 - Introduction

With the comeback of the Red Bull Air Races in 2014, Delft University of Technology has initiated a project in which a new aerobatic race aircraft is to be designed. The aircraft is required to exceed performance capabilities of current competitors while satisfying the expected regulations of 2020. This will allow it to dominate the Red Bull Air Races, in which pilots perform spectacular manoeuvres in the fastest possible time.

The primary purpose of this report is to provide detailed information about the Avinya project and the aircraft characteristics. The report includes an analysis on the sensitivity of aircraft performance characteristics on the lap times, a performance analysis which is used to optimise geometry for aircraft performance (roll rates, climb rates, pitch rates), aerodynamic characteristics (wing planform geometry, airfoils and fuselage shape) and structural analysis on the wingbox and fuselage (aerodynamic load cases and material characteristics). Based on these analyses, the report includes a detailed design which will perform the lap in the most optimal time and be able to beat the current competition.

In addition to the primary purpose, the report outlines the methodology that was used in order to arrive at the more detailed characteristics of Avinya. Furthermore the future development of this project is presented.

This report is split up into three parts: Process set-up, Technical design, Future development. Part I will include in chapter 2 the requirements and constraints. It shows the client requirements and the alterations made to the requirements and constraints that influenced the design process. In chapter 3 the baseline design of this technical report is presented with all the main features of Avinya, which were the result of the mid-term report. Hereafter the design process is presented and shows the relations between the departments which were set to achieve a good workflow. The resource allocation and budget breakdown for the project is presented in chapter 4 and in chapter 5 the logistics and operations from the start of this project up till end-of-life disposal is shown. Part II contains the technical design of Avinya. In chapters 6 to 10 the departments describe the methodology of their calculations and present what inputs were used from the other departments. These chapters will for example discuss planform decisions and the methodology behind the fuselage design etc.. Resulting is the detailed conceptual design in chapter 11 where all the final results of this report are presented including iteration values and a iteration walk-through. Part III is about the future development of the project which is started off by the requirements and feasibility analysis in chapter 12. A compliance matrix will be shown with an accompanying feasibility analysis. In chapters 13 and 14 the manufacturing and assembly plan is shown and the planning of future processes for Avinya from this point up till client delivery is presented. The future development part is concluded with the discussions on RAMS, sustainability considerations, the interface communication systems and a discussion on the technical risks of Avinya. Finally chapter 20 provides the conclusion for the final technical report and recommendations for the future design stages are suggested.

Part I

Process set-up

Chapter 2 - Requirements and constraints

At the beginning of the project, all requirements and constraints that influence the design were defined. These specifications originate from different stakeholders and vary in importance. Additionally, the mission profile and a break down structure of the functions that needed to be performed were generated. The final requirements and constraints, a combinations of stakeholder, mission and functional stipulations, were then combined into a requirements discovery tree. With the progression of the project, more insight into the subject was gained which lead to adjustments to the requirements, as it was discovered that some defined requirements were no longer according to the customers wishes or complying to the regulations.

This chapter gives an overview on the generation of the final requirements and constraints.

A stakeholder analysis was performed in which both the requirements as well as the importance and the influence of each stakeholder was determined. The requirements dictated by the four key stakeholders are summarised in Table 2.1. A complete list of stakeholders, their corresponding requirements and the interest-influence map used to determine their importance can be found in appendix A.

Table 2.1: Requirements of the four most important and influential stakeholders

Stakeholder	Requirements
DSE group	- The DSE group shall improve engineering, communication and presentation skills
	- The DSE group shall improve their skills in working as a team
Customers	- The aircraft shall win the competition
	- The aircraft shall fall within cost limits
	- The aircraft shall have better performance characteristics than the competing aircraft
Red Bull	- The competitive environment shall be such that the competition is successful
Red Bull Air Race	- The design shall comply with the Red Bull Air Race regulations
	- The aircraft shall promote motor-sports spirit

Simultaneously to the stakeholder analysis, the mission profile and scenarios were defined. Based on this, it was investigated which functions the aircraft had to fulfil over its whole lifetime, adding further requirements to be considered. Together with a more elaborated definition of the stakeholder requirements, these form the final requirements. For a better overview, the final requirements were split into technical requirements and constraints. The technical requirements specify the requirements that enable the aircraft to fulfil the technical functions and deliver the desired performance, while the constraints define the limitations within the design space. The latter are mostly due to the regulations of the Red Bull Air Race, but include additional limiting factors such as the clients wish for customisability.

The design defining requirements are summarised in Tables 2.2 and 2.3. It should be noted that this is not a complete list of all the requirements, but all information necessary for the design at this stage is displayed. The neglected requirements deal mostly with the limitations for the design options and the overall concept of the aircraft, discussed in more detail in the mid-term report. The final design from the mid-term report is presented in the next chapter. For the interested reader, the mission profile, the functional break down structure and the resulting requirements discovery tree are included in appendix A.

Table 2.2: Client performance requirements

Requirement	Value
Maximum speed	> 230
Maximum ROC	> 4700 ft/min
Maximum roll rate	$> 420^{\circ}$/s
Maximum load factor	± 10 g
Empty weight	< 700 kg

Table 2.3: Red Bull regulation constraints

Requirement	Value
Empty mass	> 540 kg
Race mass	> 698 kg
Stall speed	< 61 kts
Take-off distance	< 500 m
Landing distance	< 500 m
Wing span	$7 - 8.5$ m

Chapter 3 - Concept and design process description

Based on the most important requirements and constraints a preliminary concept was made. This design is presented again for the readers convenience. This concept serves as the starting point for the detailed technical design presented in Part II. The general layout of the Avinya design is presented in section 3.1. The choice for this design was not a straightforward one as the design is unconventional compared to the aircraft currently flying in the RBAR and does not fully comply to the current regulations. A justification for the choice of the Avinya concept is given in section 3.2.

3.1 General layout

In this section the general layout of the preliminary Avinya concept is presented. As it is a preliminary design, it is very likely to change over the course of the detailed design phase, mainly in terms of geometry. The design concept however, can be assumed not to change during the detailed design phase. A visual representation of the Avinya concept is given in Fig. 3.1. In this drawing only the geometrical parameters of the main wing and canard are given as more details were not available at the end of the preliminary design phase.

The major design feature of Avinya is its unconventional configuration with a canard, followed by the main wing and a propeller in pusher configuration at the back. The canard provides longitudinal stability and is equipped with an elevator to provide control about the pitch axis. The directional stability is provided by vertical tails mounted on the wingtips. On each vertical tail a rudder is mounted to provide the required yaw control. Due to take-off rotation considerations, the aircraft has a tricycle landing gear with a nose wheel. This undercarriage can not be retracted during flight.

The main wing and canard of Avinya feature two different airfoils. Both have in common however, that they are asymmetrical airfoils. The main aerodynamic parameters of the airfoils of the wing and the canard are presented in Table 3.1

During the course of the mid-term report, two versions of the Avinya concept were generated; one with a geometry optimised for rate of climb and one optimised for roll rate. The wing dimensions and corresponding performance characteristics of both versions are presented in Table 3.2.

Table 3.1: Avinya airfoil parameters summary

Component	**Airfoil**	**L/D** [-]	**Stall angle** [°]	**$C_{l_{max}}$** [-]	**LE-radius** [%]	**Camber** [%]	**Thickness** [%]
Wing	NACA 2412	125.8	21	1.92	3.0	2.0	14.0
Canard	NACA 2.5411	120.7	21	1.87	2.3	2.5	11.0

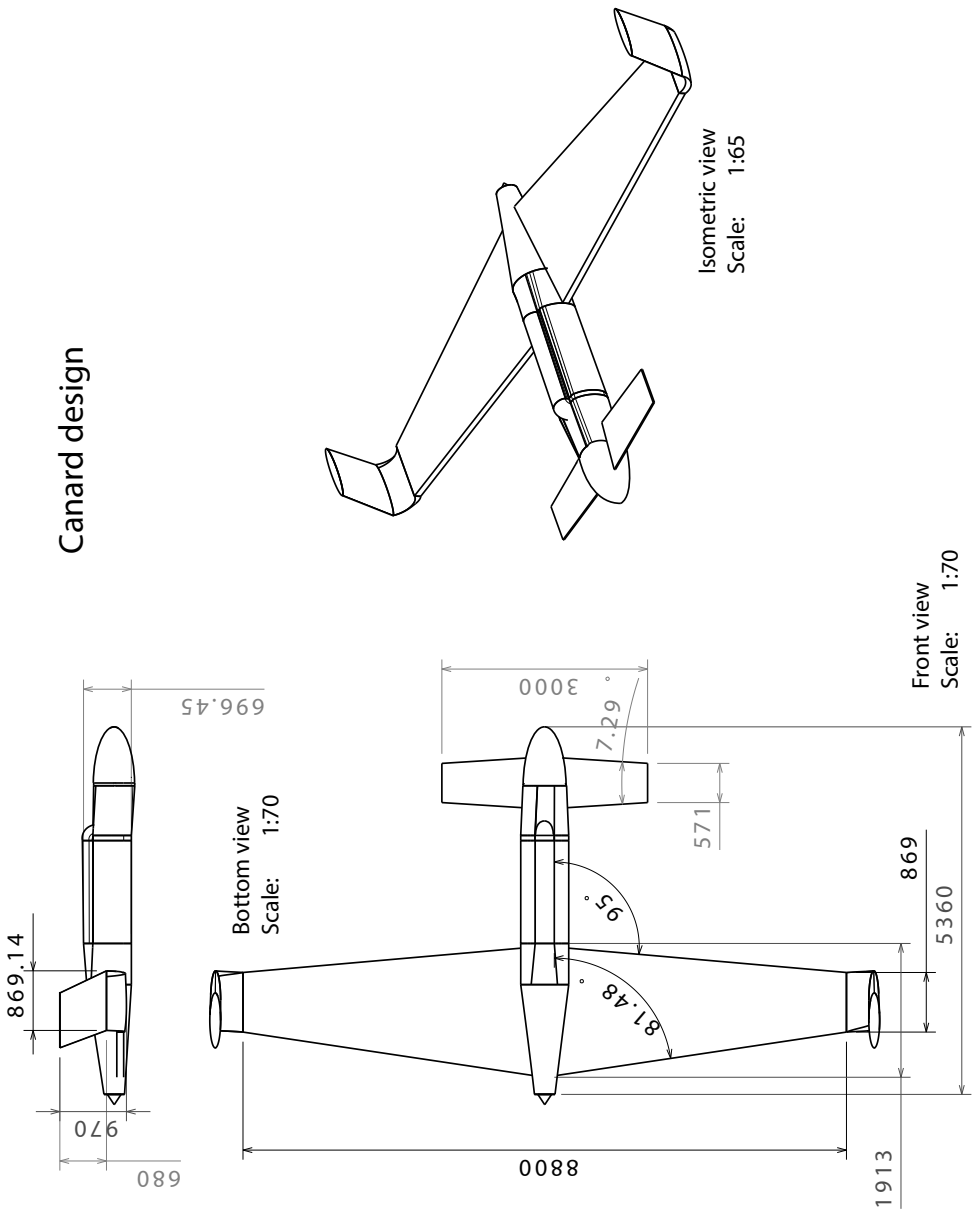

Figure 3.1: Technical drawing of the Avinya concept optimised for rate of climb with detailed main wing dimensions

Table 3.2: Wing dimensions and corresponding performance characteristics of the Avinya concept, optimised for roll rate and rate of climb.

		Optimised for roll rate	Optimised for rate of climb
OEW	[kg]	541.83	541.83
Wing loading (W/S)	[N/m^2]	635.83	575.31
Aspect ratio (A)	[-]	4.61	6.00
Wing span (b)	[m]	7.00	8.40
Wing surface area (S)	[m^2]	10.64	11.76
Wing sweep angle (quarter chord) ($\Lambda_{1/4}$)	[°]	5.00	5.00
Wing taper ratio (λ)	[-]	0.45	0.45
Wing root chord (c_r)	[m]	2.10	1.93
Wing tip chord (c_t)	[m]	0.94	0.87
Max. lift coefficient ($C_{L_{max}}$)	[-]	1.65	1.65
Max. airfoil thickness ($\frac{t}{c}$)	[-]	0.14	0.14
Stall speed (V_{stall})	[m/s]	25.08	23.86
Roll rate (p)	[°/s]	447.36	372.76
Rate of climb (ROC)	[m/s]	25.82	26.25

3.2 Regulation compliance

The choice for the Avinya concept can be considered a challenging one, as the design does not comply with the current RBAR regulations. According to these regulations it is not allowed to have an aircraft with an unconventional (pusher and canard) configuration. Furthermore, the asymmetrical airfoils featured in the design of Avinya are not allowed [1]. The choice for this concept was made because it is believed that the design will give superior performance compared to the aircraft currently allowed in the RBAR. Having the aircraft allowed to enter the competition will require convincing the RBAR officials that such a design will be of added value to the show aspect of the races, while not compromising safety. The aim of the project is to enter the competition in 2020, by which the regulations must have been adapted in a way that Avinya is allowed to enter the competition.

It can be considered that the regulations of an event like the RBAR exist because of two reasons. Firstly, to ensure that the competition between the different aircraft is fair. The regulations make sure that the pilots race each other on a level playing field and that no pilot has an unfair advantage because of the aircraft he is flying. The second and most important reason is to ensure the safety of the pilot and the spectators. The regulations contain restrictions on for example the OEW, to ensure that despite the quest of the race teams to keep the aircraft as light as possible, pilot safety is not compromised.

In order to have the design allowed to enter the RBAR, the final design phase of Avinya will need to be conducted while maintaining close contact with the race committee. This is the case for any new aircraft that wishes to enter the RBAR, but especially for an unconventional aircraft like Avinya [1]. Extensive flight testing will be needed to show that the aircraft meets all airworthiness requirements in all possible racing conditions. One aspect of the design that greatly differs from the aircraft currently flying the RBAR and that could pose a pilot safety hazard is the pusher propeller behind the pilot. In the case of an emergency the pilot would need to exit the aircraft during flight, there is a significant risk of hitting the propeller. It will be necessary to design a safety mechanism that reduces the probability and severity of this risk. This could be done by slowing down or stopping the rotation of the propeller when the pilot is about to exit the cockpit. This would reduce the suction of the propeller, reducing the probability of hitting the propeller and the severity of impact. Hitting a stationary propeller blade can be considered a safety hazard comparable to hitting a vertical or horizontal tailplane of a conventional aerobatic racing aircraft.

During the conceptual design of Avinya it is questioned why aircraft flying in the RBAR look the way that they do.

At the time the regulations were written, it was done in a way such that a certain range of existing aircraft were allowed to enter the competition. All the aircraft that have flown in the RBAR over the years are aerobatic aircraft, that had been used in aerobatics competitions and airshows before and were modified for aerobatic racing. These are all aerobatic monoplanes with wing planforms designed to have very predictable stall behaviour and uncoupled controls, in order to perform manoeuvres such as snap rolls, spins and inverted flight. It can be argued that it is not necessary for an aircraft flying in the RBAR to posses such flying qualities. That is exactly the reasoning behind the unconventional design of Avinya. It is not an aerobatic aircraft modified for racing, it is an aircraft purely designed for aerobatic racing. The choice for an asymmetrical airfoil might give the aircraft different characteristics when in inverted flight and it might therefore not be able to fly inverted for a long period of time. However, it does have superior aerodynamic efficiency for the largest part of its mission because of its cambered airfoil. In subsection 8.2.1 it will be shown that the aircraft is able to sustain inverted flight, at the expense of slightly larger drag for the short periods that occur during an air race. The same reasoning applies to the canard configuration, which has not been seen in aerobatics because of the unpredictable stall behaviour. Avinya will not be able to perform the classic aerobatic moves such as snap rolls and tailslides like the other aircraft in the RBAR, but those manoeuvres are not needed to fly the fastest time around an aerobatic race track.

Concluding, the Red Bull race committee will need to be convinced that the particular regulations that the Avinya concept does not comply with, do not compromise the safety of the pilot and the spectators. They need to be shown that having a completely different looking aircraft, with a unique flying style, competing with the aircraft currently flying the RBAR will greatly add to the show that the RBAR already is. Whether or not Avinya will enter the competition as part of a new class, or compete directly with the aircraft currently flying is a decision that needs to be made in consultation with the race committee. A possibility is that an experimental class where race teams have more freedom in their design choices and performance optimisation is added.

3.3 Design process

With the starting point based on the previous report clearly stated, the reader is guided through the holistic design process as it is conducted in during this design phase. Before going straight into the design of the aircraft on various aspects, a closer look is taken with regards to the design process. It is necessary to investigate the interaction between all departments to achieve a good work-flow and make sure that values of all parameters are communicated well. A general overview of the design process can be seen in Fig. 3.2. Detailed flowcharts showing relations and dependencies of the processes involved in each department will be shown in the introduction of the relevant chapters.

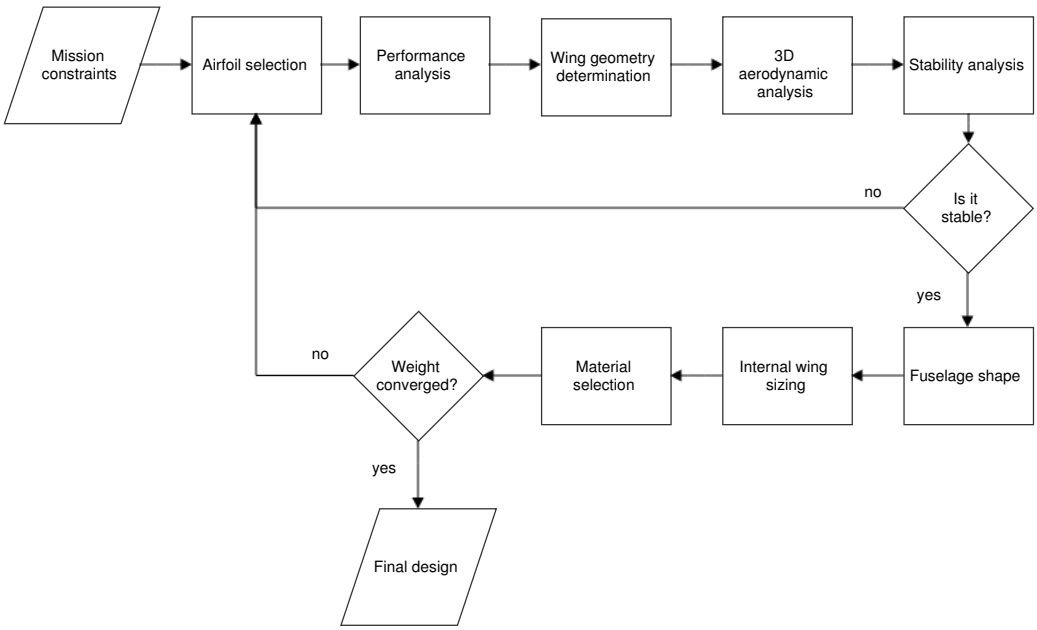

Figure 3.2: Design flow interaction between various disciplines

The design process starts off with mission constraints that provide requirements for stall speed, landing/take-off distance, rate of climb and roll rate. In order to achieve these requirements, a suitable airfoil must be selected in the beginning that can provide an optimum value of L/D and $C_{L_{max}}$ - whilst meeting other requirements such as stall speed, stall angle, landing/take-off distance - opening the route for analysing the performance of the aircraft. As a result of performance analysis, a design point is obtained and thereby values for wing loading and power loading are noted. Rate of climb and climb rate requirements are also used as defining factors for wing geometry and for sizing the control surfaces. With these values in hand, 3D geometry of the wing can be determined whose parameters include wing area, taper, aspect ratio, root chord, tip chord and wind span.

Now that the wing planform geometry is known, the 2D airfoil is modelled into a 3D wing and thus 3D wing analysis is performed using XFLR5 software. As a result of this aerodynamic analysis, polar graphs are obtained and thus the values of lift, drag and pitching moment coefficients are known for different angles of attack. These graphs and values, on one hand, help to optimise the performance characteristics of the aircraft, and on the other hand, provide information for stability analysis in order to size the canard dimensions such that the canard can produce enough vertical force and pitching moment to stabilise the aircraft. If the aircraft is not stable, then an iteration has to be done starting from the airfoil selection process. If the aircraft is stable, outputs of stability analysis such as c.g. position and fuselage length are used in designing the aircraft fuselage.

In terms of aerodynamics, the fuselage is designed in such a way that it has a high percentage of laminar flow, has an evenly spread pressure distribution throughout its length during cruise and causes least amount of induced drag to the wing. Moreover, pilot visibility and positioning is also considered during its design. From a structural point of view, the stress analysis is done for the fuselage to ensure that it can cope with loads ranging up to 15g. The same is true for the internal wing sizing and hence wing stress analysis is done in a similar manner.

Once sizing of the wing, canard and fuselage is complete, material selection is performed and weight convergence is checked. If it is positive, the design process is complete. If not, iteration is done until convergence is achieved.

Chapter 4 - Resource allocation and budget breakdown

The knowledge of the processes used to arrive at the aircraft design in the previous chapter allows the allocation of resources to take place. This is described in the chapter below by giving the budgets available and the major constraints assigned to the project.

- Design team: 10 people
- Design time: 11 weeks
- Cost: 1.25×Competitor cost
- Weight: 682 $< MTOW >$ 700 kg; $OEW >$ 540 kg

First the design team had to divide the tasks between the team members so that when the deadline was reached, all the tasks were completed in a structured way. In order to reach the final deadline, sub deadlines were set based on the project requirements as shown in Fig. 4.1. Furthermore each person had different technical tasks assigned within the group, this can be seen in Fig. 4.2. This task breakdown, allowed the group members to be more focused and efficiently complete the task. For the task breakdown after the conceptual design phase refer to chapter 14.

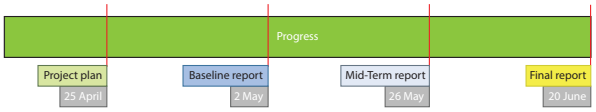

Figure 4.1: Timeline of design phase

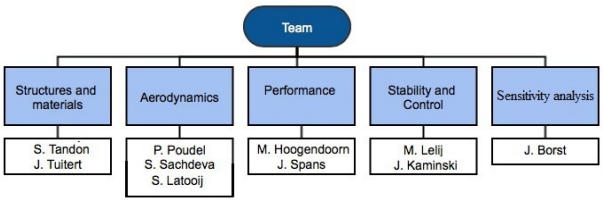

Figure 4.2: Task distribution

There are two other major constraints that have to be analysed, namely cost and weight. Based on reference aircraft it was found that the most expensive air race aircraft was that of the MXS-R which has a retail value of $410,000 (unit retail). Considering a profit margin of 40% the cost of production can be taken to be $293,000. This leads to a budget of $366,250 for Avinya's production (1.25*cost of MXS-R). This budget only applies to the production phase and ignores the cost of prototyping, testing and designing. Table 4.1 shows the budget breakdown, that the aircraft is expected to follow. The cost of the engine is fixed [2], as the engine is the same for every aircraft. The cost for the power and transmission is relatively low as the aircraft is mechanically powered and has limited electrical equipment. The cost of the material and machining is high due to the limited scale of production, so the equipment will be rented and the material will not be bought in bulk. Furthermore the costs of the on-board systems and instruments is based on the sensor/equipment requirements on-board the aircraft. Finally, the costs of labour and finishing the product are high as it is a small scale production and will be labour intensive, furthermore the production will be carried out here in Fokker aerostructures chapter 17 and salaries in the Netherlands are relatively high.

It is important to note that these costs are solely on the production of the product, there are also also other costs associated with the product, which will be described in chapter 15.

Table 4.1: Production Budget

Production phase	Cost
Engine	23,000
Power transmission	10,000
Structural materials/composites	75,000
Machining	25,000
Systems and hardware	15,000
Instrumentation	20,000
Finishing	14,000
Labour	75,000
Overhead	50,000
Total	$307,000.00

Table 4.2: Mass Breakdown

Component	Mass [kg]
Structural components	255
Fuselage	80
Wing	120
Canard	40
Vertical tailplane	15
Non-structural components	300
Engine	225
Flight control system	45
Landing gear	15
Instruments	15
OEW	555
Payload and fuel	141
Pilot	82
Camera and control system	15
G race suit and air system	8
Fuel	36
MTOW	696

As can be seen in Table 4.1 we are well within the provided budget of $366,250. However these are only estimates of what the costs will be, so the remainder can be kept for unforeseen circumstances that may arise in production.

The last major constraint is weight. Based on the expectations on performance, the constraints by the clients and Red Bull Air Race, weight is a very critical feature. In Table 4.2 the expected distribution is described, these values are based on the weights estimated in chapter 9.

The expected weight distribution does satisfy the regulations and constraints that are given. It is important to note that these are just expected weight estimates and are not accurate measurements.

These budgets will be used as guidelines during the design, however priority will be given to the performance and quality of the product such that the mission objective is met.

Chapter 5 - Logistics and operations

In the previous chapter the allocation of resources was described. In order to have a complete overview of all costs, it is important to considere the complete life cycle of the aircraft. For that reason the logistics and operations related to the mission are analysed in this chapter. In section 5.1 all operational phases and the actors involved in them are described, whereas section 5.2 eleborates on the logistics behind competing in the RBAR world championship.

5.1 Operations

The operations describe the interaction of the primary and secondary actors in each stage of the operations shown in the operational flow diagram, which can be found in Fig. 5.1. For each stage, first the primary and secondary actors are identified, then the initial and final states are defined, followed by a description of the interactions. A success and failure definition concludes the use case. The use cases have been based on information from the RBAR regulations [1].

Aircraft transportation

Primary actor:	DHL (Official Logistics Party)
Secondary actor:	Members of air race teams
Initial state:	Aircraft parked in hangar at airport 'A'
Final state:	Aircraft parked in hangar at airport 'B'
Description:	The aircraft used in the RBAR are transported from one competition location to the next location on the competition calendar by the Official Logistics Partner
Success:	Aircraft have been transported to the correct location within the allocated time without being damaged
Failure:	One or more parts are damaged or missing at the correct destination airport hanger

Aircraft assembly

Primary actor:	Team licensed technician
Secondary actor:	Technical steward, Technical Director
Initial state:	Aircraft in component parts in the hangar
Final state:	Fully assembled aircraft
Description:	Reassembly is supervised by the Technical Steward. The airworthiness and race worthiness staff for the race participation is given by the Technical Director according to Red Bull Air Race Regulations Part E 'Technical Regulations'
Success:	Aircraft has been assembled and has received an airworthiness and race worthiness certificate
Failure:	Airworthiness or race worthiness certificate is denied

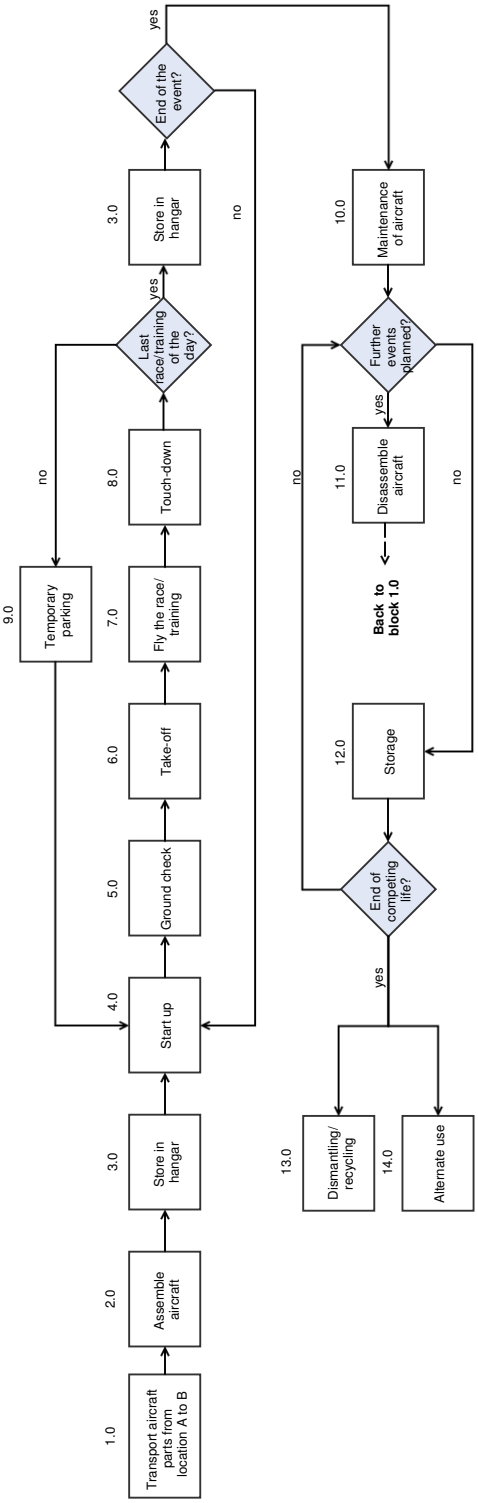

Figure 5.1: Operations flow diagram of the Avinya aircraft, from assembly to end-of-life disposal

Mounting of race specific equipment

Primary actor:	Technical staff nominated by the Director Aviation
Secondary actor:	Technical Director, member of respective Race Team
Initial state:	Aircraft without air race specific equipment installed
Final state:	Aircraft with air race specific equipment installed
Description:	The Air Race specific equipment, such as the data acquisition and telemetry box or the cameras and other necessary installations, is mounted in the Technical Hangar by technical staff nominated by the Technical Director or an assigned person. A member of the respective Race Team shall supervise the whole process and shall give written acceptance.
Success:	Air race specific equipment installed and working without damaging the aircraft within allocated time
Failure:	Damage to aircraft or non-functioning equipment

Initial race scrutinising

Primary actor:	Technical steward and Technical Director
Secondary actor:	Respective team member
Initial state:	Pre-inspected aircraft
Final state:	Post-inspected aircraft
Description:	After shipping, reassembly and mounting of the race specific equipment in the aircraft, technical scrutinising shall be performed with all participating race aircraft. This may include, but is not limited to, the following points: general, fuselage, wing, engine, propeller and race specific equipment.
Success:	Aircraft has passed initial race scrutinising
Failure:	Aircraft has failed initial race scrutinising

Pre and post race inspections

Primary actor:	Technical director
Secondary actor:	Team licensed technician
Initial state:	Aircraft has not been checked
Final state:	Aircraft has been checked
Description:	Before take off and after landing the race aircraft is subject to scrutinising checks. Also the race aircraft may be called to the weighing station at each location without prior notice.
Success:	The technical director signs off on the aircraft.
Failure:	Suspension for technical reasons imposed

Flying sessions

Primary actor:	Pilot
Secondary actor:	RBAR officials
Initial state:	Aircraft takes off
Final state:	Aircraft lands
Description:	An air race consists of the following flying sessions: training session, two qualifying sessions, wild card, top 12, super 8, final 4.
Success:	Aircraft and pilot are safe on the ground after completing respective flying session
Failure:	Everything else

Post Race Procedures

Primary actor:	Pilot
Secondary actor:	RBAR officials
Initial state:	Post race inspection
Final state:	Stored in hangar
Description:	Immediately after the final flying session of an event, the post race inspections are performed in the parc fermé for the top three ranked race aircraft as well as one randomly chosen race aircraft ranked lower than the third place. The top three ranked aircraft are presented for the ceremony after which they are returned to the hangars just as the race aircraft ranked lower than the third place.
Success:	Aircraft back in the hanger after passing post race check
Failure:	Non compliance with regulations

Aircraft Disassembly

Primary actor:	Team licensed technicians
Secondary actor:	-
Initial state:	Aircraft in assembled state
Final state:	Aircraft is in disassembled state
Description:	The disassembly of the race aircraft for transport to and from the race location shall be performed by a licensed aircraft A&P/EASA technician or equivalent. The technician will confirm proper reassembly according to the guidelines of the manufacturer and this shall be signed in the aircraft log book.
Success:	Aircraft has been disassembled correctly
Failure:	Damage of aircraft or non disassembled aircraft

5.2 Logistics

Concerning the logistics during the competing life of Avinya, transport of the disassembled components needs to be analysed. Using the final aircraft dimensions for the wing, vertical stabiliser and fuselage, as shown in Table 11.15, conclusions can be drawn with respect to the transportability of the aircraft.

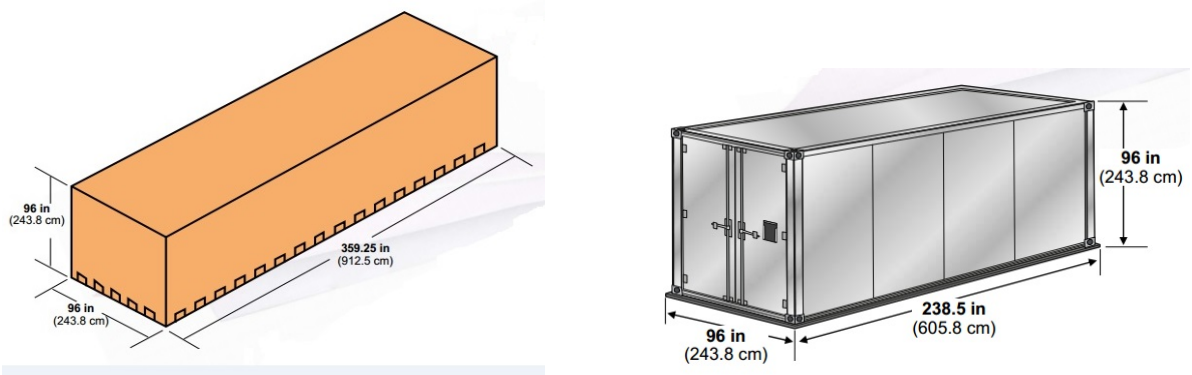

(a) 747F nose cargo **(b) AGA 20ft box container**

Figure 5.2: Unit load devices for aircraft transportation

[3]

All aircraft's and operational items concerning the RBAR are transported by train, ship and air [4] and during/in between races Red Bull allocates responsibility to a logistic team for the transport of the aircraft's. With restricted container space available the aircraft is disassembled into three major components, fuselage, wing and tail box,

where the wings are placed in eight-metre long boxes, the stabilisers and tail structure in separate padded boxes and the fuselage is strapped to a pallet. The design of Avinya's major components must be ensured to fit in the available space. The containers in which the wings and fuselage are transported are shown in Fig. 5.2, with their indicated sizes. Due to the high value of sweep, the wings do not fit in vertical or horizontal position in the standard containers and have to be inclined resulting in less efficient stacking, thus less efficient transport. In Table 5.1 the angle at which the wing needs to be inclined is given.

Table 5.1: Logistics parameters for transport of wing

	Wing 1	**Wing 2**
Required height wing [m]	2.730	2.728
Required length wing [m]	7.340	7.880
Angle of inclination [°]	26.68	26.75

Two fuselage's can fit without problems in the available containers as the track width of the landing gear is smaller than the available width of the containers. This is done with in a nose to tail configuration, where one fuselage is positioned backward with respect to the latter one. Also it is important to note that the design considered has multiple removable parts, including 2 vertical stabilisers, wings and canards, which have to be packaged separately and transported, this might cause problems in space management within the container. Overall, the Avinya aircraft will challenge the logistic team of the RBAR. To overcome these disadvantages, the costs and environmental impact of transport can be decreased, for example if the containers are transported by train instead of truck, which requires accurate planning, as it is slower, but does not require storage for longer periods of time [4].

A significant problem may also arise in logistics when the time and distance between races is small and/or it is decided to airlift the equipment or ferry each aircraft on its own. Since the Avinya aircraft has a very limited range, it is not able to be flown by itself to the next event and will have to be transported separately or fuel tanks have to be implemented or added. As the OEW and MTOW of the aircraft is not constrained during transport, an recommendation on adaptability of the design might be the inclusion of fuel tanks stored inside the fuselage, wing or as external tanks attached to the aircrafts outside. Stability and control analysis need to be performed to ensure the aircraft is stable and controllable when fuel tanks are added.

Part II

Technical design

Chapter 6 - Trajectory optimisation and sensitivity analysis

Previously, a trajectory optimisation tool was set-up for flying the concept aircraft around a set track. Now that this is in place, section 6.1 provides the set-up for a Red Bull air race track to measure the aircraft's performance. In addition, it is possible to analyse the most import design characteristics. This chapter elaborates on the method for screening the input parameters and introduces a set of design guidelines based on this screening, which is presented in section 6.3.

6.1 Abu Dhabi Red Bull race track

The track used so far was a sample track, which was used in the work of Van der Plas [5] for, amongst others, verification purposes. Now that the trajectory optimiser is set-up, an actual Red Bull air race track is used. The Abu Dhabi track was used, which was the first course to be flown in the 2014 championship. Peter Wezenbeek has provided the official GPS coordinates, which were used to model the track [6]. A top view is shown in Fig. 6.1 and all the coordinates and description of the gates can be found in Table 6.1. In addition, regulations were adhered to stating that an aircraft has to fly through a double gate between 15 and 25m [1].

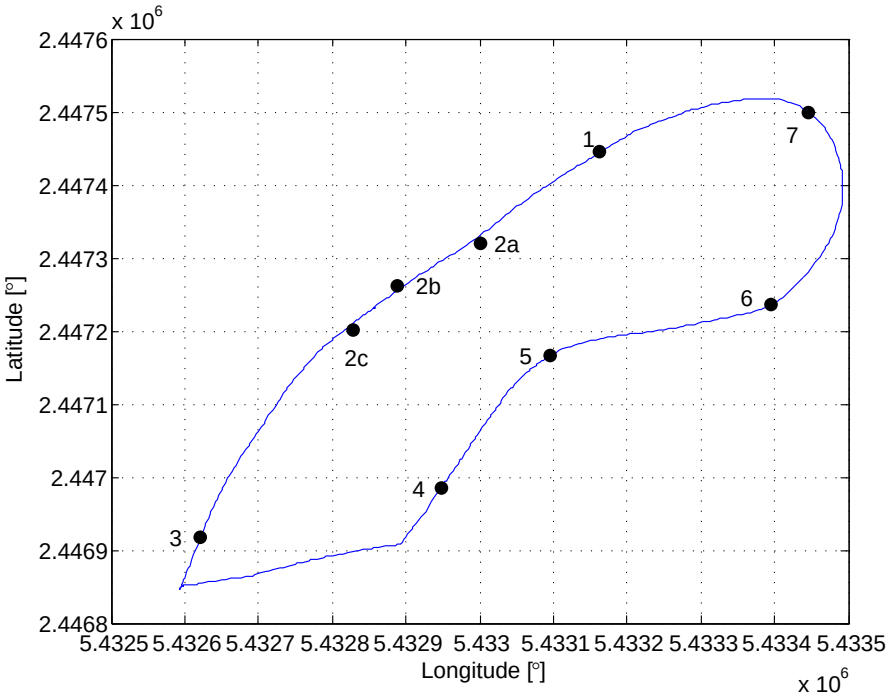

Figure 6.1: Abu Dhabi race track indicating all gates, top view

Table 6.1: Abu Dhabi race track pylon GPS positions

Gate #	Type	Longitude	Latitude	Heading	Phase
1	Double	24°28′28.01″N	54°19′53.88″E	HDG 247°	
2a	Single	2b + 125m on HDG 050°			Chicane
2b	Single	24°28′21.40″N	54°19′43.99″E	-	Chicane
2c	Single	2b - 125m on HDG 230°			Chicane
3	Double	24°28′8.99″N	54°19′34.34″E	HDG 230°	Half-cuban eight
4	Double	24°28′11.46″N	54°19′46.13″E	HDG 055°	Half-cuban eight
5	Double	24°28′17.95″N	54°19′51.42″E	HDG 053°	S-turn
6	Double	24°28′20.48″N	54°20′2.20″E	HDG 056°	S-turn
7	Single	24°28′29.96″N	54°20′4.09″E	-	180° turn

6.2 Verification and validation

To make sure that the trajectory optimiser outputs correct values, firstly verification is done. This has been done in the mid-term report, where the model's output is compared to the work of Van der Plas [5], which is assumed to be verified on itself.

During the development of the Abu Dhabi track, each phase (from one gate to the next) was modelled separately before multiple were combined. Before all phases were combined, separate manoeuvres were combined to make sure a solution could be found.

Even though verification of the model itself is done, it cannot be assumed to be validated. Especially due to the fact that another track is modelled, which is based upon other constraints (such as Red Bull regulations), this might give faulty outputs.

As an actual Red Bull race track is set-up, validation can be done as well. This will be done by comparing the race times of the trajectory optimiser with the race times of pilots during the 2014 championship. Unfortunately, not all data is available to do a perfect validation analysis. However, final times can be compared and will be done later in section 11.2.

6.3 Elementary effects method for input screening

Although it is valuable to see how well an aircraft competes on a set track, this does not directly give any insight in the focus points during the design of an aircraft. The process of finding these points is called input screening.

In order to identify the most important factors in the mathematical model of the trajectory, an analysis is done using the elementary effects (EE) method. This is a method introduced by Morris [7] and is widely used as a screening method for computational costly models or models that depend on large numbers of inputs. The method provides a qualitative sensitivity for a change in inputs, which allows for ranking of the input factors with regards to their importance.

The approach of the EE method is very basic. One simulation with an initial set of parameters is done, which - in this case - results in a total time the aircraft flies around a certain track. Using this as a basis, one input parameter is changed whilst all the other parameters remain unchanged. This is then done for various input parameters (preferably all) One-At-a-Time (OAT).

As all other parameters remain unchanged it thus assumes that the particular value can still be achieved whilst another has been changed, yet this might not always be realistic. For example, an aircraft's roll rate might not be achieved with a higher wing span. However, this method investigates the influence of parameters on the output and

not their plausibility. The methodology to calculate the feasibility of parameters are done in chapters 7 to 10.

An OAT approach could be done randomly, but also systematically where the sensitivity is analysed around an initial estimate. The latter was done here, where the initial estimate consisted of the aircraft's design parameters as set at the end of the mid-term technical report. The initial parameters are shown in Table 6.2 and will be referred to as the 'baseline parameter(s)'.

Table 6.2: Baseline aircraft parameters used as a basis for sensitivity analysis

Parameter	Value	Unit
OEW	541.83	kg
p	405.5 7	deg/s
q	90	deg/s
S	10.64	m^2
A	4.605	-
C_{D_0}	0.0209	-
ROC	25.9	m/s
V_{stall}	48.75	kts
V_{ne}	230	kts
Total time	31.4191	s

Following the OAT method, each parameter is changed independently through evaluating with the parameter sets shown in Table 6.3. The sensitivity on the output of the model for the parameters, is shown in Fig. 6.2. Here the y-axis indicates the absolute difference with respect to the baseline time and the x-axis indicates the difference from the base value. This base value is the respective baseline parameter value. Figure 6.2b shows a zoomed in version of Fig. 6.2a. Without creating too much clutter, as many parameters revolve around the same output range, the sensitivity of speeds V_{stall} and V_{ne} are plotted separately (Fig. 6.2c).

Table 6.3: Parameter input ranges

Parameter	Minimum	Step size	Maximum	Unit
p	200	25	500	deg/s
q	45	5	90	deg/s
A	3.0	0.5	10.0	-
OEW	500	25	700	kg
C_{D_0}	0.0100	0.0025	0.0400	-
V_{stall}	20	5	90	m/s
V_{ne}	150	10	250	kts

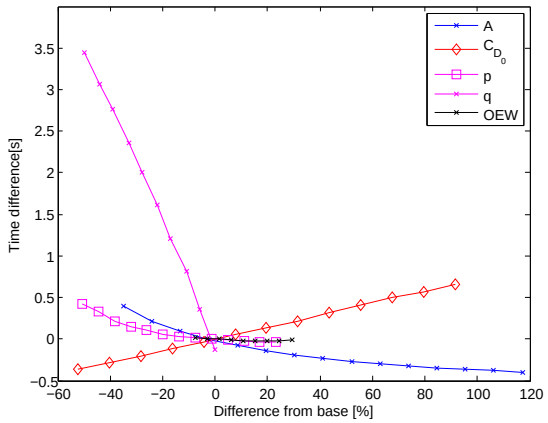

(a) A, C_{D_0}, p, q and OEW sensitivity

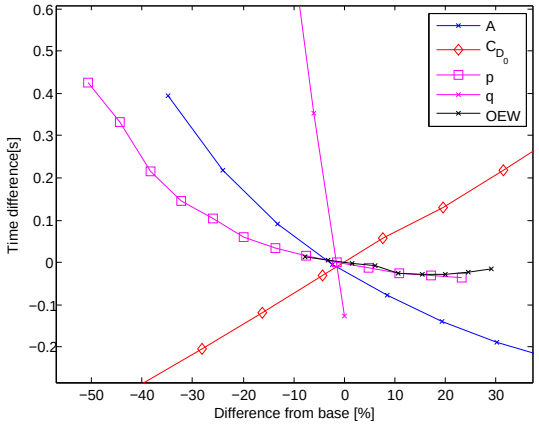

(b) Closer view of A, C_{D_0}, p and OEW sensitivity

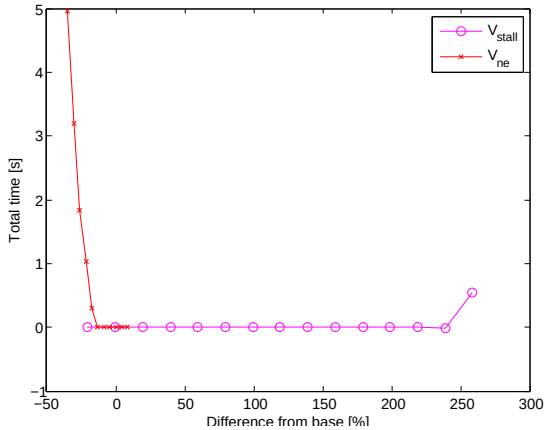

(c) V_{stall} and V_{ne} sensitivity

Figure 6.2: Input sensitivity on output of trajectory model

Preliminary, a few conclusions can be drawn. First of all, the speed does not have a major influence on the design if some boundaries are taken into account. The boundaries are: $V_{stall} < 80$ m/s and $V_{ne} > 200$ kts. From preliminary sizing, we found that both are easily achieved and thus are not the biggest driving parameters.

Additionally, it can be seen that the pitch rate q has the biggest influence with regards to time. However, note that here all other input parameters remain constant. Thus, it is not a valid conclusion to say that e.g. an increase in pitch rate will lead to this absolute decrease in time as an increase in pitch rate will likely also lead to an increase in drag. This relation is not shown in these figures.

In order to draw conclusions from these input sensitivities, some statistical analysis is done. According to Morris, the elementary effects method provides two sensitivity measures for each input factor, namely:

- μ: assesses the overall importance of an input parameter on the output
- σ: describes the non-linear effects and their interactions

The meaning of both μ and σ, comes from statistics. Herein μ is defined as the mean and σ is defined as the standard deviation. In order to compute these for a model, the so-called elementary effect $d_i(X)$ for each input factor is computed using Eq. (6.1). Here, Y is the output of the model (in this case time t), X_i are the inputs with a total of k parameters and Δ is the difference in input parameter X_i. Also, $\bar{X}$ indicates the baseline parameters.

Having computed the elementary effect, the mean and standard deviation are found using Eq. (6.2).

$$d_i(X) = \frac{Y(X_1,\ldots,X_{i-1},X_i+\Delta,X_{i+1},\ldots,X_k) - Y(\bar{X})}{\Delta}, \quad \text{where } \bar{X} = (X_1,X_2,\ldots,X_k) \tag{6.1}$$

$$\begin{aligned} \mu_i &= \frac{1}{r}\sum_{j=1}^{r} d_i\left(X^{(j)}\right) \\ \sigma_i &= \sqrt{\frac{1}{(r-1)}\sum_{j=1}^{r}\left(d_i\left(X^{(j)}\right)-\mu_i\right)^2} \end{aligned} \tag{6.2}$$

According to Morris, the importance of the parameters can be ordered by the mean value μ. However, Campolongo et al. [8] have shown that a better order is achieved when ordered by μ^*. Through this way, one does not need to compare both the mean and the standard deviation, but only one parameter. Nevertheless, judging the σ values regarding their non-linear effects and interactions is still valid. μ^* is computed using Eq. (6.3).

$$\mu_i^* = \frac{1}{r}\sum_{j=1}^{r}\left|d_i\left(X^{(j)}\right)\right| \tag{6.3}$$

An analysis was done on the following input parameters of the system: the roll rate p, pitch rate q, aspect ratio A, OEW, drag coefficient C_{D_0} and the speeds V_{stall} and V_{ne}. The results can be seen in Fig. 6.3 in terms of the mean and standard deviation. From this figure, the importance can be evaluated.

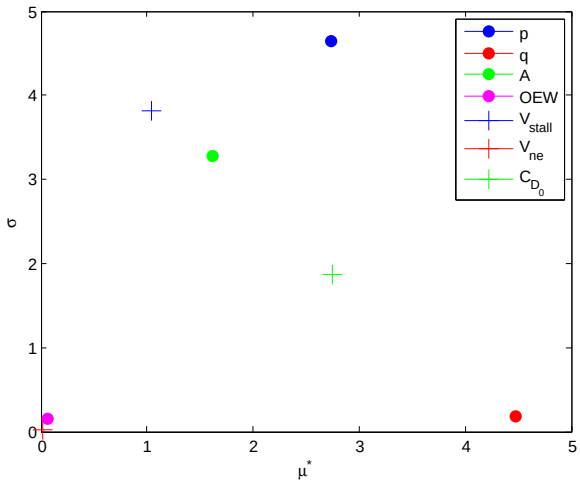

Figure 6.3: Mean and standard deviation of the input parameters on the output of the trajectory model

One can see that the most important parameters to base the design of the aircraft on are the pitch rate q, roll rate p, drag coefficient C_{D_0} and aspect ratio A based upon their mean value. From these, the roll rate and aspect ratio have a particularly large value for σ and thus can be concluded that their involvement is mostly non-linear and many interactions take place, whereas the pitch rate has a very linear involvement in the model.

6.4 Design guidelines

From the results of the input screening, some design guidelines are created to keep in mind when designing the aircraft. These guidelines are particularly effective to judge when it is feasible to actually implement a design feature. For example, one might want to improve the roll rate but this also results in a larger drag coefficient.

Using basic curve fitting of Fig. 6.2, the equivalent design equation is created as shown in Table 6.4 in order to judge a design feature. Here, one would input the change of a particular parameter and have the time penalty as the output. The time penalty is the amount of seconds the aircraft flies slower around a track; thus, a negative time penalty means the aircraft performs the track in a shorter amount of time.

Table 6.4: Design guidelines: time penalties on input parameter change

Time penalty	Input unit
$-0.0014\Delta p$	$^\circ$
$-0.079\Delta q$	$^\circ$
$0.026(\Delta A)^2 - 0.48\Delta A$	-
-0.0013ΔOEW	kg
$50\Delta C_{D_0}$	-

With this in mind, a methodology needs to be set-up to compute the parameters of the aircraft. The following chapter will elaborate on the performance analysis as a start for determining these.

Chapter 7 - Performance analysis

With the performance characteristics that have the largest influence on race times known from the previous chapter, the methodology used to determine the necessary wing geometry in order to realise the performance is presented. This chapter will explain the performance analysis method for Avinya. First the most important performance parameters and the method to determine them is described in section 7.1. Next the method used for sizing the wing and the control surfaces in order to meet the requirements on these parameters are treated. The sizing of the wing planform is explained in section 7.2, where actually two wing planforms are designed to allow for modularity. Finally the method used for sizing the control surfaces is explained in section 7.3.

The performance department has to work in a close relationship with the other departments since the performance is dependent on multiple factors from the other groups. The relationships can be seen in Fig. 7.1.

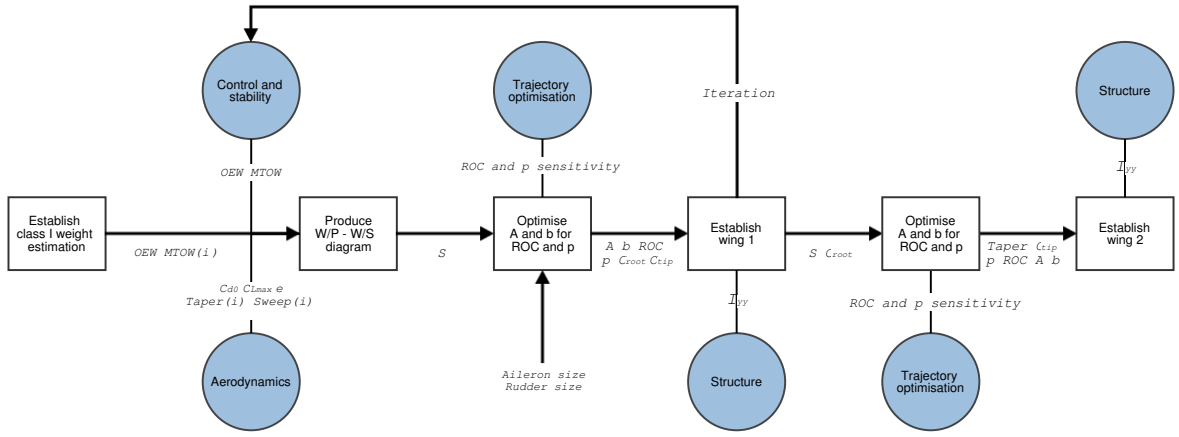

Figure 7.1: Relations and dependencies of the processes involved in the performance analysis

As the figure shows the performance department is linked with all the other departments. The class I weight estimation is the starting point for the entire iterative process. The initial weights (OEW and $MTOW$) are updated after the class II weight estimation which will be done by the control and stability department. The following steps will include the optimisation for ROC and roll rate using guidelines obtained in the sensitivity analysis (chapter 6) and establishing the two wings optimised one for roll rate and the second for rate of climb.

7.1 Performance parameters

In this section the main performance parameters, climb, roll and pitch rate are described. For each parameter the method used for estimating the aircraft performance and the related assumptions are discussed. Subsection 7.1.1 explains how the climb rate is calculated, while subsections 7.1.2 and 7.1.3 describe the calculation of the roll rate and pitch rate respectively.

7.1.1 Rate of climb

The rate of climb (ROC) is one of the most important requirements for the RBAR aircraft since it is necessary for almost all manoeuvres. The half-cuban eight is an example manoeuvre that is in almost every course and it is a manoeuvre where a race can be won or lost. Having a higher ROC than the competitors can just give the edge needed to complete a course in the fastest time. The ROC is calculated using Eq. (7.1), where C_{D0} is taken from the aerodynamics department and the Oswald factor (e) is assumed to be 0.9 in accordance with Roskam [9][Ch.

5]. The propulsive efficiency (η_p) is assumed to be 0.9, which is relatively high, but assumed to be valid as the propeller is a high performance model.

$$ROC = \frac{\eta_p}{W/P} - \frac{\sqrt{\frac{2(W/S)}{\rho}}}{\frac{1.345(Ae)^{3/4}}{C_{D0}^{1/4}}} \tag{7.1}$$

The design parameter that mainly drives the *ROC* is the aspect ratio. A higher aspect ratio will result in a higher ROC, which primarily is an effect of lower induced drag and hence a better L/D ratio. In section 7.2 the sizing of the planform is performed, where Eq. (7.1) will be used to ensure that the required *ROC* is achieved.

7.1.2 Roll rate

Another important performance parameter is the roll rate (p). Having a large maximum value for p allows the aircraft to fly fast turns and chicanes. The main driving parameters for p are the aileron authority ($C_{l_{d\alpha}}$) and the roll damping coefficient (C_{l_p}). The roll rate is calculated using Eq. (7.2), where the maximum aileron deflection (δ_α) is assumed to be 25° and V to be the design speed, equal to 170 kts.

$$p = -\frac{C_{l_{d\alpha}}}{C_{l_p}} \delta_\alpha \left(\frac{2V}{b}\right) \tag{7.2}$$

The maximum p is dependent on two design aspects. The roll damping coefficient, C_{l_p}, since it is mainly determined by the design of the planform while $C_{l_{d\alpha}}$ is driven by the sizing of the control surfaces. The latter is performed in section 7.3. In contrast to the *ROC*, p decreases with an increase in aspect ratio (and hence wingspan). This shows that these two performance parameters will be the subject of the major wing design trade-off. Whether a higher p or *ROC* is required mainly depends on the race track under consideration, which was shown using the trajectory optimisation software chapter 6.

7.1.3 Pitch rate

In the sensitivity analysis it was found that the pitch rate of the aircraft is critical in achieving fastest time and therefore it was decided to analyse the pitch rate. This is done by calculating the pitch rate with the dynamic equations. This equation is shown in Eq. (7.4) [10].

The aim for the pitch rate is dependent on the load factor at which the aircraft should be able to fly at a certain airspeed. This airspeed for the RBAR case was set as 170 kts and the load factor at ±10g as stated by the client requirements. The pitch rate 'requirement' can be calculated with Eq. (7.3) [11]. Using the load factor requirement and the design airspeed the pitch rate requirement was calculated as 1 rad/s which is equivalent to 57.2 $^\circ/s$.

$$q = \frac{g}{V_{des}}(n-1) \tag{7.3}$$

In order to get the pitch rate q of Avinya, the integral of the equation has to be taken of Eq. (7.5). The constant in Eq. (7.5) represents the pitch capabilities that the aircraft possesses at the design angle of attack. This value will be assumed to be zero at the beginning of a pull up manoeuvre.

M_y is calculated using the deflection of the canard elevators and the C_L value of the main wing (0.15) during the pull up manoeuvre which are taken from the aerodynamics department. The elevator deflection was taken

as 20° after talking to Martin Orlita, a aerobatic aircraft pilot. The other input, I_{yy} is taken from the structural department.

$$\dot{q} = \frac{M_y}{I_{yy}} \tag{7.4}$$

$$q = \frac{M_y}{I_{yy}} t + \text{constant} \tag{7.5}$$

As one can see, these equations are only based on pure dynamics of a rigid body under a torque. Therefore, the equation was changed by adding the pitch damping (C_{m_q} = -15.53, which was taken from the aerodynamics department) of the entire aircraft. This pitch rate decrease is calculated using Eq. (7.6) [11]. This δq is then added to Eq. (7.5) resulting in Eq. (7.7).

$$\delta q = \frac{1}{\frac{1}{2}\rho V S \bar{c}^2 C_{m_q}} \delta M_y \tag{7.6}$$

$$q = \frac{M_y}{I_{yy}} t + \frac{1}{\frac{1}{2}\rho V S \bar{c}^2 C_{m_q}} \Delta M_y \tag{7.7}$$

In this case, the ΔM_y is equal to M_y. The last variable that is left is t, the time duration of the stick input during the pull up manoeuvre to achieve high pitch rates. It is estimated as 0.9 s using the Abu Dhabi race track data [12] and the race optimisation tool. The final resulting value of the pitch rate is used in the race track optimisation to verify that it actually achieves a better or worse lap time.

7.2 Planform design

The determined performance parameters, will be the inputs used for the planform design. The design of the planform starts off by taking the operational empty weight (OEW) and the maximum take-off weight ($MTOW$) from the class II weight estimation performed by the control and stability department. These weights, together with an initial size of the canard are the inputs for the planform design.

In the next step the wing loading versus power loading diagram has to be produced for all the different phases in the mission profile (landing, manoeuvring, climb etc.). In the RBAR case, the engine is provided and therefore the power available (P_a) is known. This loading diagram will show the design space and design point for the aircraft, the wing loading at the given power loading. Combining the design space with the engine power and $MTOW$ will result in the design point and therefore the initial surface area (S). The S that is determined here is taken as the total surface area, hence of the wing and the canard combined, as both are lifting surfaces providing positive lift.

With the initial S, $MTOW$ and the P_a known, the optimisation for climb rate and roll rate can be performed. This is done by looking at all combinations possible for the aspect ratio with wing span that result in either the highest roll rate or climb rate (these values are almost inversely proportional). It is important to note that the RBAR regulations restrict the wingspan to be between 7 and 8.5 meters, which also restricts the possible aspect ratios. [1] Furthermore it is important to realise that the W/S-W/P diagrams are only valid for a certain aspect ratio and that the ultimately selected aspect ratio should be close to the aspect ratio used for generating the diagrams and the resulting W/S.

After the generation of all the combinations of the aspect ratio with wing span (within limits), the optimal combination has to be chosen (wing 1). The first wingspan is chosen such that both the climb- and roll rate requirements are met.

The next step is to find a second wing planform with the exact same root chord (c_r) and S to allow for modular wings. The choice for the second planform is based on the sensitivity analysis in chapter 6. Here it was found that an increase in climb performance and aerodynamic efficiency is more beneficial to the track time than the roll rate. For this reason the second planform has a larger aspect ratio (and wing span), resulting in better climb performance at the expense of the roll rate. Because c_r is the same as for wing 1, the taper ratio of wing 2 is lower, which has an effect on the spanwise lift distribution. It is ensured, however, that the difference between the taper ratios of wing 1 and 2 are small enough such that the earlier assumptions on for example oswald factor are still valid.

7.3 Control surface sizing

As soon as the planform design is concluded the control surface sizing will be done using the outputs from the planform design. The scope is limited to the lateral control surfaces only, as the size of the canard is mainly determined by longitudinal stability requirements and is therefore treated in chapter 9. In subsection 7.3.1 the sizing of the ailerons is explained, subsection 7.3.2 treats the sizing of the rudder and the initial elevator size is estimated to be proportional to the size of the ailerons. Finally, subsection 7.3.3 describes the balancing of the control surfaces.

7.3.1 Aileron sizing

Preliminary sizing of the aileron for the required roll performance is performed using a method proposed by Gudmundsson [13, Ch. 23]. The wing planform is used as an input to create an estimate for C_{l_p}. For a wing with straight taper, C_{l_p} is estimated using Eq. (7.8).

$$C_{l_p} = -\frac{(C_{L\alpha} + C_{D0})C_r b}{24S}(1+3\lambda) \tag{7.8}$$

In order to calculate $C_{l_{d\alpha}}$, first an estimate of the change in airfoil lift coefficient due to aileron deflection $c_{l_{d\alpha}}$ has to be made. This depends on the ratio of aileron chord over wing chord and the wing lift gradient. The chord of the aileron is assumed to be 27% of the local wing chord, which yields a value of 0.52 for the aileron effectiveness parameter τ, as can be found in Fig. 7.2. The chord length of the aileron is mainly determined by the position of the rear spar, which is at $0.3\frac{x}{c}$ from the trailing edge. The value of C_{L_α} is initially estimated and later updated with results from the aerodynamic analysis. The value of $c_{l_{d\alpha}}$ is calculated using Eq. (7.9) [14, Ch. 16]. The calculation of $C_{l_{d\alpha}}$ of a wing with straight taper is calculated using Eq. (7.10) [13, Ch. 23].

$$c_{l_{d\alpha}} = C_{l_\alpha}\tau \tag{7.9}$$

$$C_{l_{d\alpha}} = \frac{2c_{l_{d\alpha}}}{Sb}\left[\left(b_2^2 + b_1^2\right) + \frac{4(\lambda-1)}{3b}\left(b_2^3 + b_1^3\right)\right] \tag{7.10}$$

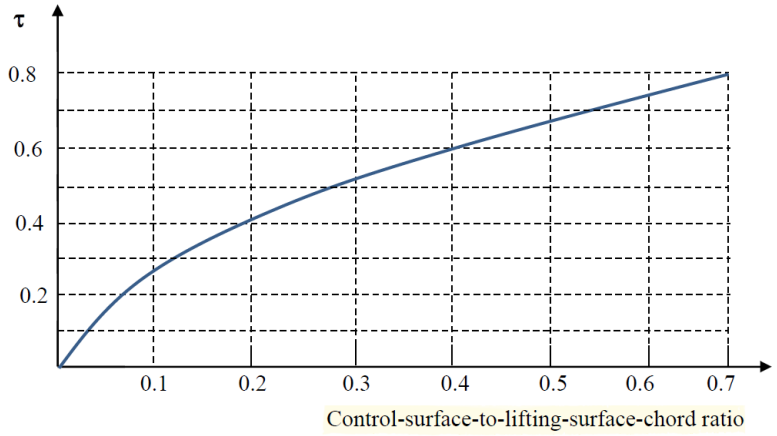

Figure 7.2: Control surface angle of attack effectiveness parameter [13, Ch. 12]

The span of the ailerons is iterated until the required roll rate p is achieved. The roll rate is calculated using Eq. (7.2), as presented in subsection 7.1.2. It is assumed that the ailerons can not deflect further than 25° in positive or negative direction. Due to the winglets it is not possible for the ailerons to cover the full span of the wing. However, for maximum effectiveness the endpoint of the aileron should be as close to the winglet as structurally possible. It was decided not to let the ailerons cover the full span on the inboard side because the inner parts of the ailerons produce relatively little rolling moment due to their short moment arm. The benefit that this part of the aileron brings to the roll performance does not outweigh the additional drag that these larger control surfaces cause, as this would significantly increase the bleed rate in turning manoeuvres. The sensitivity analysis in chapter 6 as well as the information provided by Peter Wezenbeek indicated that in terms of track times, it is better to keep the C_{D_0} (so the bleed rates low) rather than having a small increase in roll performance. Finally it was decided to let the ailerons start at 20% and end at 95% of the half span, taking into account local fuselage radius and positioning of the vertical stabiliser. Asides, this provided sufficient roll control without increasing the C_{D_0} too much.

7.3.2 Rudder sizing

The size of the rudder can be driven by different requirements, such as landing in crosswind conditions, spin recovery and the amount of yaw required for flying coordinated turns. In this stage the rudder sizing will be done based on the spin recovery requirement. This is because the spin recovery is the most critical requirement for an aerobatic aircraft. The rudder size should later be checked against the other requirements in the detailed design phase when more accurate estimates of the stability derivatives and aerodynamics are known. The sizing of the rudder for spin recovery is performed using Raymer's method. [15, Ch. 16]

To determine the required size of the rudder to stop the aircraft from spinning after it has entered a deep stall, first the spin recovery criterion (SRC) needs to be determined using Eq. (7.11). Another parameter that needs to be determined is the aircraft relative density parameter (μ). This is done using Eq. (7.14), after which the required tail damping power factor (TDPF) is taken from Fig. 7.3. The moments of inertia required for calculating the SRC are estimated using Eqs. (7.12) and (7.13), where $\bar{R}_x$ and $\bar{R}_y$ are assumed to be 0.25 and 0.38 respectively. Even though a more accurate estimation of I_{yy} is produced in subsection 7.1.3, it was decided to stick to Raymer's method for estimating the moments of inertia. This is because in the calculation of the SRC it is more important to find the difference of the inertia's (body heavy vs tail heavy), rather than having and accurate estimation of the value of the inertia. If the moments of inertia are overestimated using Raymer's method, the effect will cancel out as only the ratio is important in Eq. (7.11).

$$SRC = \frac{(I_{xx} - I_{yy})\, g}{b^2 MTOW} \tag{7.11}$$

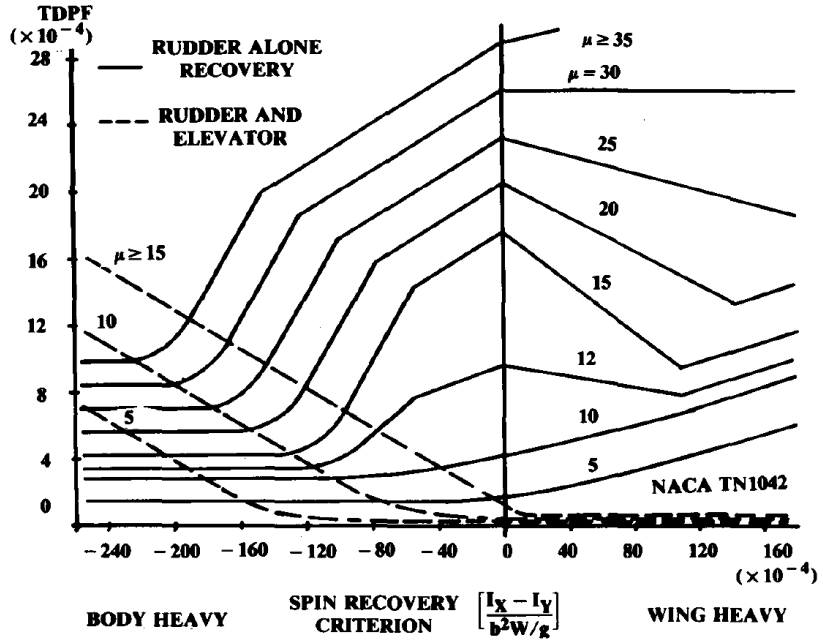

Figure 7.3: Spin recovery criteria [15, Ch. 16]

$$I_{xx} = \frac{b^2 MTOW \bar{R_x}^2}{4g} \tag{7.12}$$

$$I_{yy} = \frac{L^2 MTOW \bar{R_y}^2}{4g} \tag{7.13}$$

$$\mu = \frac{W/S}{\rho g b} \tag{7.14}$$

The TDPF that the aircraft should posses to overcome the spinning motion is calculated next. The TDPF depends on the tail damping ratio (TDR) and the unshielded rudder volume coefficient (URVC), which are calculated using Eqs. (7.15) and (7.16).

$$TDR = \frac{S_f L^2}{S_w (b/2)^2} \tag{7.15}$$

$$URVC = \frac{S_{R_1} L_1 + S_{R_2} L_2}{S_w (b/2)} \tag{7.16}$$

When the aircraft is spinning in a stalled condition, parts of the rudder become ineffective as they are deflected into stalled air and therefore can not produce any lift. In accordance to Raymer [15, Ch. 16], it is assumed that the region of stalled air is confined by a line of 30° from the trailing edge and a line of 60° from the leading edge. Given that the vertical tails are mounted on the wingtips, conventional winglets would be completely inside the wake of the stalled main wing. Therefore, in order to have effective rudder in a spin condition, it is necessary to have the vertical tails extend above and below the wingtips. This causes the vertical tails to be approximately symmetrical

about the wing tip, and therefore the side force produced by the rudders does not cause a large moment about the aircraft x-axis. This reduces the coupling between roll and yaw motions, which is beneficial for an aerobatic race aircraft. The rudder starts behind the chord of the wingtip, such that it can move freely through all deflections without interfering with the wing.

The method used for calculating TDR and URVC in Eqs. (7.15) and (7.16) is an adaption on the method explained in Raymer. The adaption is needed since the vertical tails are mounted on the wingtips, rather than in the middle of the horizontal stabiliser. As there are two vertical tails that work together to provide the required yaw control, one rudder will deflect inboard and the other outboard. As the aircraft is spinning in a stalled condition, the outboard deflecting rudder will deflect into the undisturbed airflow, while the other deflects into the wake of the main wing. The effective rudder area (S_{R_1}) is therefore equal to the total rudder area on one side and equal to the part that is outside of the wake on the other. The same holds for the area of the rest of the vertical tail (S_f). The TDPF of each vertical tail is calculated and then added as shown in Eq. (7.17)

$$TDPF = (TDR)\,(URVC) \tag{7.17}$$

The geometry of the vertical tails and rudders is iterated multiple the wing area, fuselage length and longitudinal wing location are changed throughout the process. In the end it is ensured that the TDPF of both vertical tails, as calculated in Eq. (7.17) is larger than the required TDPF as found in Fig. 7.3.

7.3.3 Balancing of control surfaces

Due to the high manoeuvrability requirements on the aircraft, the control surfaces are relatively large. Without properly addressing control surface balancing, the stick forces would become too high for the pilot to handle. Whether is actually happens was addressed in the stick force analysis in chapter 9. The challenging tracks in the RBAR require the pilots to change the attitude of the aircraft quickly and with high precision. For this reason the controls should not only be light, but also precise and with enough 'feel' for the position. This makes balancing a tedious task, as the size and position of the balances should be exactly right. Control surface balancing and the resulting feel for the controls depends on the pilots personal preference as well and therefore it is preferable to have customisable control balancing systems. As the primary control systems are required to be mechanically operated, the balancing systems should be as well [1].

For this reason, balancing spades are a good option for reducing the stick forces caused by the control surfaces. Balancing spades are flat plates attached to the aileron and are suspended below and in front of it. Balancing spades are widely used on aerobatic aircraft because they provide very effective balancing of control surfaces. The stick forces are relieved by the spades in two ways: Firstly by acting as a mass balance because they add weight in front of the aileron hinge line. Secondly, as the ailerons are deflected, the spades rotate into the flow and create an upwards or downwards lift force in front of the hinge line. This aides further deflection of the ailerons into the stream, acting as an aerodynamic balance. For the rudder, the stick forces will probably not be as high as for the ailerons and therefore a simpler mechanism that causes less drag, a horn for example, can be used.

As mentioned before, the sizing of balancing systems and horns are tedious tasks and depend on parameters such as gap size and hinge moment coefficients that are hard to estimate. Moreover, as the required feel of the ailerons is a personal preference of the pilot, the exact sizing of the spades should be done in a later stage. An advantage of the balancing spades is that they are easily modified, compared to balancing systems that are more integrated such as horns. This naturally progresses towards the aerodynamics to model the wing geometry and ensure the required aerodynamic coefficients are achieved.

Chapter 8 - Aerodynamic analysis

Analysis of wing geometry as determined in chapter 7 for performance will have a significant influence on the aerodynamics. An analysis is performed to find the required airfoil and check whether the assumed aerodynamic characteristics are achieved. The method and software used for this 2D and 3D wing analysis are described in the first section. Following this the design process is described for the aerodynamic analysis of the aircraft and all its subparts. The aerodynamic process also involves recurring iterations, Fig. 8.1 shows this process with the inputs and outputs from each section in the form of a flow chart.

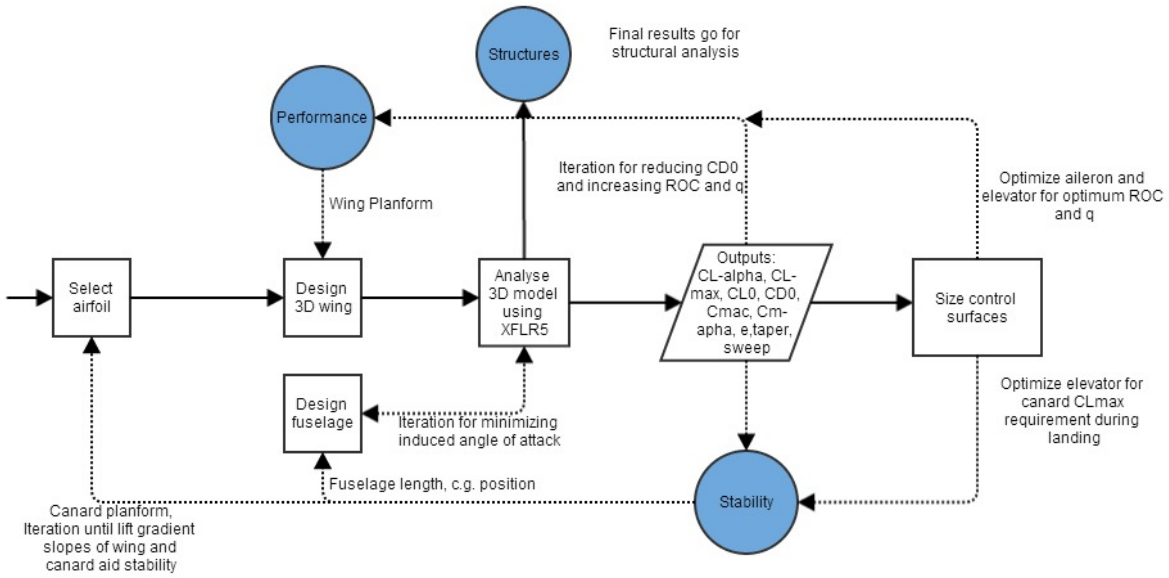

Figure 8.1: Relations and dependencies of the processes involved in the aerodynamic analysis

As can be seen in the flowchart the aerodynamic process involved is very iterative between the stability and performance departments. The process starts with the airfoil selection which is then analysed using the wing dimensions from the performance department for the 3D analysis. These results are then iterated with the fuselage design, the performance department and the stability department to generate a highly efficient aerodynamic design. The results from the final iteration are then provided to the structural department to get the ideal structural design of each subgroup.

8.1 Methodology

There are many methods and software tools present for performing a detailed aerodynamic analysis. In this section these methods will be briefly discussed and the method used in this report will be described.

There are two types of analyses that can be performed, the first is a two dimensional analysis which looks at airfoil geometry to create polar graphs, and the 3D model which looks at the aircraft geometry to get the complete aerodynamic analysis. For both these considerations a CFD model will be used. A CFD model changes the wing from a continuous problem domain to a discrete domain using a grid. There are mainly two types of methods that can be used for CFD analysis. A finite difference method uses the Taylor's series expansion to derive the discrete equations, and thus changing the differential equations to an algebraic one. The other method is that of finite volume, in this method the integral form of the conservation equations are applied to a finite volume (cell) to

get discrete equations. The number of grid points/cells defines how accurate the actual result the program outputs. In order to reduce the error an approach used by CFD tools is to perform multiple iterations and thus reduce the residual [16].

Due to time limitations to use extensive CFD tools, it has been decided to use a low-fidelity (performs lesser iterations and has more residual) software. Although this will decrease the accuracy of the result, the precision and ability to complete the task in the given time will be possible. This section will talk about the CFD methods and tools that can be used.

8.1.1 2D analysis

For the 2D analysis two programs have been considered, Javafoil and Xfoil. Both these programs are used for performing a CFD analysis of a 2D wing. However, Javafoil was only used as a secondary support and mainly results from Xfoil were used.

Xfoil is a free interactive program made by MIT used for the 2D analysis of airfoils. It uses a FORTRAN executable to analyse 2D airfoils at different angle of attack and Mach numbers. An inviscid linear-vorticity method is used which is highly efficient at predicting flow at low Reynolds number. A source distribution and wake permit model is used to analyse the interaction of the potential flow and the viscous layer. And finally the method uses the Global Newton method to solve the boundary layer and transition equations [17].

Although Xfoil does take into account the effect of separation bubbles and coupling, but can only handle limited amount of separated flow, and hence falls short in predicting an accurate stall angle. Eppler method is recommended for stall behaviour analysis. However Xfoil is incorporated in XFLR5 which will be used for the 3D analysis of the wing and thus Xfoil results are considered for the analysis.

8.1.2 3D analysis

For the 3D analysis also two software tools have been looked at namely, XFLR5 and Tornado. These softwares are both low-fidelity software, that are quick at performing the analysis, however do have a trade-off in accuracy.

Tornado

Tornado is a MATLAB based software which uses vortex lattice method (VLM) for linear aerodynamic wing design. Basically Tornado models the lifting surface as thin plates and gives the polars for each panel based on the geometry given. It is very fast paced and allows for multiple considerations such as different characteristics for each panel, different state conditions to analyse and also provides stability derivatives for the aircraft. However the program is limited in the design, as it only analyses lifting surfaces and cannot be used to analyse the fuselage. Below is a brief description of the vortex lattice method.
VLM: Vortex lattice method is a method that involves converting the wing into a 2D mesh grid. With each panel being a lifting surface and containing a single horse-shoe matrix. A bound vortex is located at the 1/4 chord position and by applying the surface flow boundary conditions the bound vortexes can be computed. Using a summation one can determine the complete performance of the wing. The VLM method however does have its limitations. The VLM method firstly calculates forces such as C_l based on integration of surface forces, and then uses it to calculate the viscous variables such as Cd, based on 2D data. This results in inaccuracies near the stall angles, where the polar curve is not straight. Furthermore the VLM method makes a small angle of attack approximation, this leads to the vortices not being aligned with the free-stream velocity. Overall VLM is a good method to analyse wings with high Reynolds numbers and difficult geometries, however is a bit weak in determining stall characteristics and drag coefficient [18].

XFLR5

XFLR5 is a program that combines the 2D drag polar analysis with the 3D aircraft analysis. For the 2D analysis, the program uses a C++ adaptation of Xfoil and a good graphical user interface to display the results. For the 3D analysis, XFLR5 allows VLM, lifting line theory (LLT) and 3D panel method. It is useful to know that these methods are accurate for low reynolds numbers. A description of the LLT method and the 3D panel method is given below.

LLT: Lifting line theory is a non linear 3D analysis method that simplifies the wing into a lifting line.Vortices are generated behind the wing and are proportional to the rate of change of the lift. Furthermore from the 2D analysis one can see the change in lift with a change in angle of attack. By analysing these 2 features one can get the lift distribution. Following this the polar mesh is altered based on washout and the drag, moment and performance factors can be computed. However the LLT is inaccurate when analysing wings with low aspect ratio and large amounts of sweep. Furthermore it is not possible to perform a non viscous LLT calculation, as the method requires the determination of α_0 and with viscous effects this value cannot be determined. Also the wing is only modelled on the xy plane, so these effects would not be properly analysed.

3D Panel Method: The 3D panel method attempts to incorporate the thickness of the wing into the design. The method involves representing the perturbations generated by the wing with a sum of doublet and sources distributed over the wing top and bottom surfaces. It is however not possible to model the wing as a thick surface with a fuselage present due to the absence of a 3D-CAD program in XFLR5. The method used will be that of a thin surface with horseshoe vortices. The wakes are modelled in approximately 2D (the distance between the upper wake and lower wake is infinitesimally small). Furthermore when the boundary layer is thick, the surface is staid to be stationary and the flow inviscid, non-rotational and also incompressible. This program is a good option for aircraft analysis and especially for the analysis with the fuselage [19] [20]. Note it still cannot calculate the drag coefficient of the fuselage and other components.

The aircraft operates with Reynolds number ranging from 4 million to 12 million (approximately). It is therefore accurate for the design, however it is not accurate for stall characteristics. It has been decided to use a combination of the VLM method and the 3D panel method for the 3D analysis of the aircraft. Specifically, for the wing the VLM method will be used, and due to the high accuracy of the 3D panel method for fuselage design, it will be incorporated in its design analysis. In order to analyse the stall angle and characteristics, the 2D graphs will be used. As XFLR5 has the possibility to analyse both the 2D design and incorporate both the VLM and 3D panel method, it will be the program that will be used. Furthermore it was realised that the drag polar could not be calculated for components other than the lifting surfaces accurately. Therefore an analytical method will be used, with equations that can be used to estimate the values.

8.2 Lifting surfaces design

The wing is the most critical component in terms of design. It is important to have a design that outputs the least drag and highest lift, furthermore it also has an impact on the pitching moment. The wing analysis has been subdivided into three sections, the airfoil selection, the planform shape and the control surfaces.

8.2.1 Airfoil selection

In order to conduct the airfoil selection (2D analysis) 2 aspects were considered, the performance and the feasibility. Both these aspects will be discussed below.

Performance

In the mid-term report the performance comparison was carried out, it involved firstly determining the performance characteristics of the airfoils. This can be seen in Table 8.1.

Table 8.1: Baseline main wing airfoil data

	NACA 2414	Eppler 1230	Gemini	Falcon	Clark Y
L/D	125.8	149.8	108.0	115.5	124.7
Stall angle [°]	21	17	20	19	20
$C_{l_{max}}$	1.92	1.79	1.71	1.77	1.91
Le-radius	3.0	2.6	1.3	1.3	1.2
Camber	2.0	3.6	2.2	1.6	3.4
Thickness	14.0	17.4	15.4	13.7	11.7
C_m during cruise	-0.052	-0.066	-0.040	-0.009	-0.082

Following this, depending on the mission profile and concept necessities a weighting factor is given and a score based on the performance is given to each airfoil. For the canard concept this process had to be performed twice, once for the canard and once for the main wing. The trade-off for the most suitable airfoil for the main wing is done in Table 8.2.

Table 8.2: Airfoil trade-off matrix for the main wing airfoils

Parameter with weighting	NACA 2414	Eppler 1230	Gemini	Falcon	Clark Y
High L/D (0-6)	4	6	2	3	4
High $C_{l_{max}}$ (0-5)	5	3	1	2	4
High stall angle (0-7)	7	3	6	5	6
Low camber (0-5)	4	1	3	5	2
High le-radius (0-4)	4	3	2	2	1
Low thickness (0-3)	1	0	1	2	3
Low C_m (0-7)	5	4	5	7	3
Total (0-37)	30	20	20	26	23

From Table 8.2 results one can see that NACA 2414 airfoil scores the highest total and was selected as the airfoil for the main wing. The reynolds number used for the analysis in the mid-term report was $8 \cdot 10^6$. A similar trade-off was carried for the canard wing, shown in Table 8.3 and Table 8.4.

Table 8.3: Aerodynamic performance characteristics for considered canard airfoils

	NACA 4412	GOE 796	AH 79-100A	NACA 2.5411	GOE 629
L/D	111.4	102.9	121.4	120.7	88.9
Stall angle [°]	18	21	20	20	20
$C_{l_{max}}$	1.85	1.85	2.00	1.87	1.61
Le-radius	1.0	1.6	1.3	2.3	4.0
Camber	4.0	3.7	3.7	2.5	2.8
Thickness	12.0	12.0	10.0	11.0	13.6
C_m during cruise	-0.098	-0.084	-0.150	-0.062	-0.068

Table 8.4: Airfoil trade-off matrix for the canard airfoils

Parameter with weighting	NACA 4412	GOE 796	AH-79-100 A	NACA 2.5411	GOE 629
High L/D (0-6)	5	4	6	6	2
High $C_{l_{max}}$ (0-5)	3	3	5	4	2
Optimum stall angle (0-10)	10	5	6	5	4
Low camber (0-5)	2	3	3	5	4
High le-radius (0-4)	1	1	1	2	4
Low thickness (0-3)	1	1	3	2	0
Low C_m (0-7)	4	5	2	6	7
Total (0-40)	26	22	26	30	23

From Table 8.4 results one can see that NACA 2.5411 airfoil scores the highest and is the best airfoil for the canard in terms of performance. For the canard the reynolds number selected was $2 \cdot 10^6$.

Feasibility

From the airfoil selection, it was found out that the best airfoil is slightly different from the norm, it has a slight camber. It is important to see the reason why other aircraft have no camber and whether it is possible to use it. Furthermore, it is important to look at the aircraft as a whole and ensure it is feasible. According to the Red Bull Air Race regulations the wing has to be symmetric. The reasoning for this is that a symmetrical airfoil has better inverted performance, as it provides the same lift [1]. The graphs shown in Fig. 8.2 are used in order to analyse the selected, slightly cambered airfoil in inverted flight.

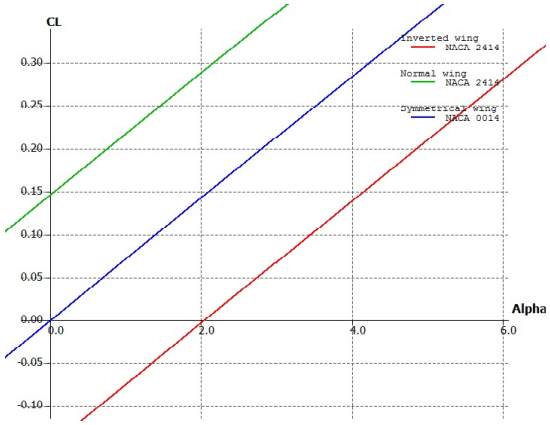

(a) C_L-α curve

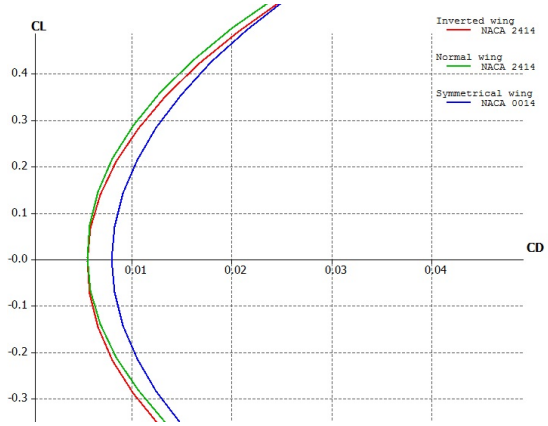

(b) Drag Polar

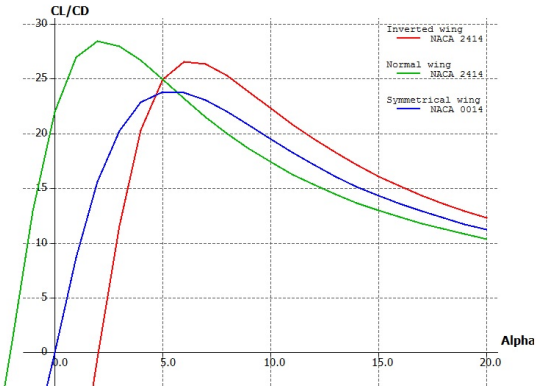

(c) C_L/C_D-α curve

Figure 8.2: Cambered airfoil inverted flight

In Fig. 8.2 a comparison is done with the symmetric wing, the cambered wing and the inverted cambered wing. One can see in the C_L-α curve in Fig. 8.2a that the normal cambered wing has a higher lift than that of a symmetrical wing (which is as expected). When this wing is inverted its lift mirrors itself on the symmetrical wing to give a lower lift. This can be expected as the camber is shaped to provide more lift in the normal layout. From this graph one can further see that for the design lift coefficient of 0.15 (maintain symmetric flight), the cambered wing is expected to fly at 0° angle of attack (AoA), the symmetrical wing at 2 AoA and the inverted cambered at 4 AoA. As the wing is only expected to be in inverted flight for 2 seconds and the aircraft seems to be on the most part capable of inverted flight lift considerations are not a major factor. Furthermore one can see that the drag polar in Fig. 8.2b shows that the drag for a cambered wing is better in the inverted and the normal position. For the C_l/C_D ratio one can see that the cambered airfoil in the normal position offers the best performance at low angle of attacks, and so would be best for the straight symmetrical flight regions, and for the inverted flight one can see that the cambered airfoil's performance is slightly worse. It is still feasible and comparable to the symmetrical wing. The combination of these two graphs can be seen in Fig. 8.2c and it can be seen that the three graphs are comparable in performance levels with respect to C_l/C_D, at different angle of attacks.

There are also two other aspects that have to be analysed when making the airfoil selection, namely the stall characteristics and the aircraft stability. For the stall of a canard, it is beneficial to have the canard stall before the main wing. The reason for this is that when the canard stalls, the pilot will have time to use the aircraft's wing and its control surfaces to get out of the stall. For desirable control and stability statistics, the airfoil geometry is very important. It is desirable for the airfoil of the main wing to have a CL_α curve similar to that of a canard. This has

been investigated later in chapter 9, it was found that the aircraft is not controllable with the current selection. It was therefore necessary to change the canard airfoil to NACA2414, the same airfoil as that of the main wing.

After analysing all the different concerns regarding the cambered wing, it is concluded that the cambered airfoil chosen is a feasible design consideration. Although it is outside the regulations, the performance considerations were able to outweigh it in the trade-off matrix in the mid-term report. As the clients have also given approval to the design, this regulation will be disregarded in the airfoil design.

8.2.2 3D wing analysis

The planform design as shown in Table 8.5 is generated primarily from the performance and stability departments and done to optimise aircraft performance factors. One can see the primary dimensions generated from this department for the mid-term report in chapter 3. However it was realised that some of these results were inaccurate and had to be modified. The alterations from the mid-term parameters for the wing and canard can be seen in Table 8.5:

Table 8.5: Changes from preliminary design to conceptual 1^{st} iteration of 3D wing analysis

Parameter	**Preliminary**		**Conceptual 1^{st} iteration**	
Wing				
	Roll	Climb	Roll	Climb
Surface area [m^2]	10.65	11.76	10.65	10.65
Aspect ratio	4.61	6	5.38	6.50
Taper	.45	.45	.45	.32
Sweep (1/4 chord [deg])	5	5	25	25
Canard				
Surface area [m^2]	1.713	1.713	2.34	2.34
Aspect ratio	5.25	5.25	6.5	6.5
Airfoil	NACA 2.5411	NACA 2.5411	NACA 2414	NACA 2414

When analysing the difference between 2D and 3D wing it was realised that the 3D wing has a linear $C_L - \alpha$ relation, and has a $C_{L_{max}}$ lower than that of the 2D wing. This is lower, due to the generation of vortices that change the effective angle of attack of the 3D wing and the inability of XFLR5 to properly analyse stall characteristics. Furthermore the canard has a higher gradient than that of the wing. This is the primarily due to the high aspect ratio of the canards. This gradient difference is highly important to ensure that the stability is maintained and the canard stalls first. Furthermore when combined, it can be seen that the total coefficient of lift is slightly higher than the current wing, which can be expected from a canard design (as both lifting surfaces provide lift). In the planform optimised for climb one can expect the lift of the wing to increase due to an increase in the aspect ratio. This will also result in the highest possible combined slope.

In terms of drag polar, at low C_L the drag is expected to be very similar, primarily due to the similarity in airfoil selection. At higher angle of attack one can relate to the C_L-α curve and expect the canard to cause a higher lift distribution. This also means that the canard can have a lower angle of attack to produce sufficient lift and thus reduce the total drag. When the canard is combined with the wing, the total drag will increase, however it is not added. This is because of the wing canard interaction, the canard reduces the induced drag at the roots as it blocks some of the airflow. Furthermore it is expected that the design optimised for climb will have a higher L/D ratio and the wing has greater contribution to the lift due to a longer span.

In a graph for pitching moment the canard causes an unstable moment as an increase in angle of attack would case the aircraft to pitch more up (as the canard is far ahead of the c.g). Furthermore the wing causes a highly stable

motion as it is behind. When combined, the design will be close to neutral stable (one of the design criteria). For the climb optimised design, the difference will be primarily of the wing's stand alone moment coefficient, this will change from highly stable to unstable, the reason for this is that the taper of the wing has changed so the c.g. of the wing moved forward. It however has little influence when performing the analysis on the whole aircraft. In order for a graphical representation of the 3D analysis refer to appendix B.

The 3D analysis gives guidelines to select the aerodynamic parameters for which the wing needs to be optimized for. A high $C_{L_{max}}$ value is undoubtedly one of the most important parameters needed for improving the performance of the aircraft. For the best aerodynamic efficiency, L/D ratio of the wing has to be optimized - not only for the design speed but also for performing effective aerobatic maneuvers. Another factor that needs to be considered is C_{D_0}, which needs to be as low as possible and can be optimized mostly by changing wing planform and fuselage shape. Finally for ensuring stability of the aircraft, values of lift curve slopes and pitching moment coefficients for both canard and the wing need to be looked upon. Iterations on these aerodynamics parameters needs to be performed in order to come up with the final design.

8.2.3 Control surfaces

This section will analyse the effect of control surfaces on the performance. The control surfaces that will be discussed are the elevators, ailerons and rudders. The sizing of these control surfaces has been done in section 7.3, and will be used for the analysis using XFLR5. The values obtained during this analysis are likely to be overestimated since XFLR5 does not take interference drag into account caused by wing and control surface connection. The primary purpose of ailerons is to cause the lift to increase locally, and thus cause a rolling moment. The ailerons as determined from the performance section will be positioned at the trailing edge of the wings and will cover 75% of the span and 25% of the chord length as discussed in chapter 11. Depending on the moment arm and the lift increment one can get the rolling moment of the aircraft. The effect of the aileron deflection at different angle of attacks on the lift coefficient can be seen in Fig. 8.3.

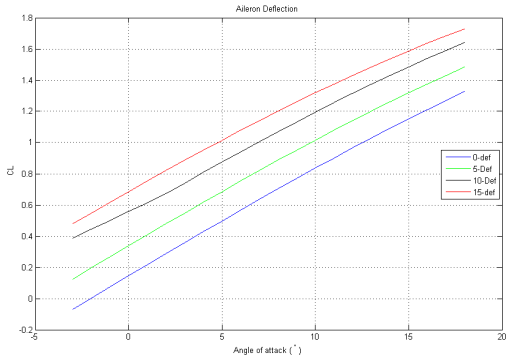

Figure 8.3: Aileron deflection on change in lift coefficient

As can be seen by changing the aileron deflection one can increase the lift provided quite significantly and thus cause a rolling moment. As can be seen in the graph a 5 degree deflection causes an increase of 0.18 C_L when compared to 0 deflection and this value goes up to 0.54 at 15 degree deflection. The maximum deflection of the aileron is 24 degree (stall limitations) and at this stage the expectation is that the effect on the C_L will be to the range of 0.88. Also one can see that at different angle of attacks the lift impact of the elevators is the same (from the baseline of 0 deg deflection), causing the lines to be parallel.

The elevators have a function of increasing the lift and rate of climb. For the concept, the elevators will be placed on the canards and will occupy 30% of the chord length and 70% of the span and will have an airfoil of NACA 0014, section 7.3. The effect of the elevators on the lift coefficient can be seen in Fig. 8.4.

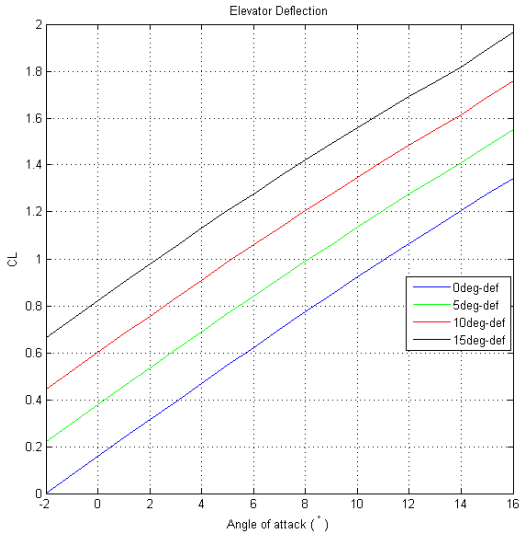

Figure 8.4: Elevator deflection on change in lift coefficient

As can be seen the elevator deflection of 5 degrees causes an increase of lift coefficient by approximately 0.2 for the canard. This is a significantly high efficiency as the canard gets undisturbed flow and so the low area elevators provide lift increments equal to that of the ailerons which are bigger and on the wing. Furthermore it is crucial to note that the max deflection is 20° as shown in subsection 7.1.3, at this point the change in C_L is expected to be 0.8 after analysing that the change is proportional.

Rudder is the last control surface that has to be analysed. Its goal is to cause a yawing moment by inducing a side force when deflected. Because of the geometry planform, this feature cannot be analysed using XFLR5 and so its aerodynamic characteristics is not possible to analyse. A more extensive CFD tool must be used for the analysis.

8.3 Fuselage design

The fuselage of Avinya is required to provide space for a pilot in the cockpit and space for the engine in the aft section of the aircraft. The fuselage also serves to position control and stabilisation surfaces in specific relationships to the lifting surfaces, required for aircraft stability and manoeuvrability. Conforming to the results of the sensitivity analysis in chapter 6, where it was found that an increase of the drag coefficient results in a large time penalty, the design of the fuselage will focus on minimising drag whilst still fulfilling the requirements of housing the pilot and engine, and positioning the stabilisation and control surfaces. In subsection 8.3.1 the ideal fuselage shape is examined and a fineness ratio determined, followed by an examination of the limiting dimensions and their location in section subsection 8.3.2. An initial design of the fuselage is presented in subsection 8.3.3 followed by a brief discussion on the method of optimization.

8.3.1 Ideal fuselage shape with respect to aerodynamic efficiency

This section focuses on the ideal fuselage shape for the minimisation of drag. The largest contribution of fuselage drag is the parasitic drag; drag not directly associated with the production of lift. Parasitic drag is composed of viscous pressure drag, also known as form drag, skin friction drag, and interference drag. Form drag and skin friction drag together make up the profile drag. In Fig. 8.5 the build up of the profile drag for an all-turbulent Airbus A300 and A300 with laminar lifting surfaces is depicted to show the percentage the fuselage makes up. Even though the A300 is a different class of aircraft, it serves to show the significance of designing the fuselage to have low profile drag. Reduction of skin friction drag can be achieved by having a body with natural laminar flow.

Past the transition point the flow becomes turbulent and the skin friction drag increases dramatically.

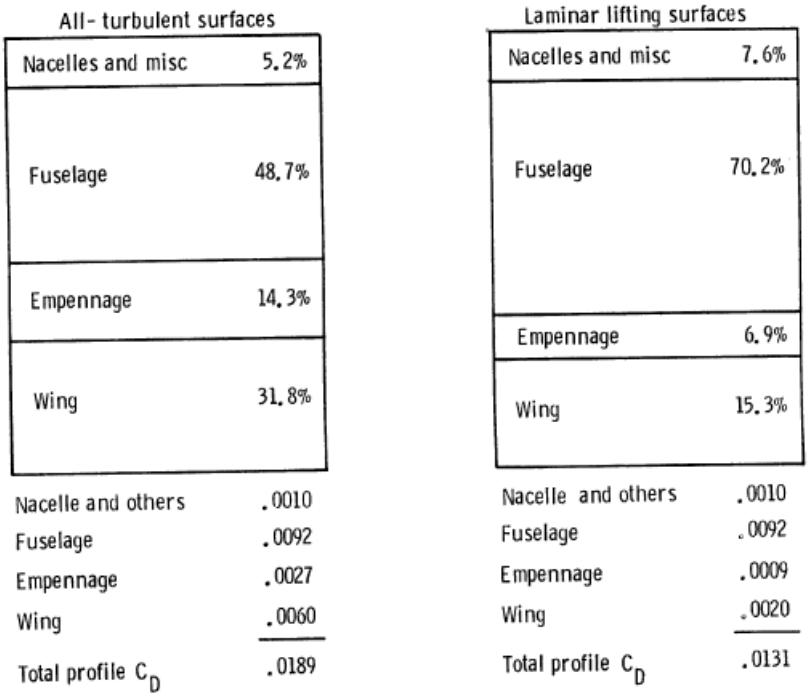

Figure 8.5: Build up of profile drag for all-turbulent Airbus A300 and A300 with laminar lifting surfaces [21]

According to Hoerner smooth fuselages may have a drag which is close to that of streamline bodies of rotation having the same fineness ratio [22]. The fineness ratio is the ratio of the length of a body to its maximum diameter. Hoerner argues that the ideal fineness ratio for a streamline body is 2.7. When using a streamline body for a fuselage the flow is disturbed by interference, due to additional bodies attached to the fuselage, such as wings, empennage, and landing gear. For such bodies the ideal fineness ratio value would be higher. Research by Lutz and Wagner shows that the ideal fineness ratio is dependent on the Reynolds number [23]. With increasing design Reynolds number the amount of favourable pressure gradient in the fore-body region has to be enlarged in order to delay transition. This can be done by either increasing the body diameter or by moving the maximum thickness point further foreward. It should be noted that enlarging the body diameter is limited by the maximum pressure recovery being possible without turbulent separation. The length Reynolds number for the fuselage is given by Eq. (8.1) in which L_f is the fuselage length, ρ the density of the fluid, V the velocity, and μ the kinematic viscosity of the fluid.

$$Re = \frac{\rho \cdot V \cdot L_f}{\mu} \tag{8.1}$$

The length of the fuselage is determined by the stability group in chapter 9; the initial value for the fuselage length was set at $6[m]$. Using ISA values for the density and kinematic viscosity, and a velocity of $77[m/s]$, a Reynolds number of $Re = 2.52 \cdot 10^7$ is found. From Lutz et al. an ideal fineness ratio of approximately 2.5 would be chosen for this design regime (Reynolds number), with a maximum thickness at 50% of the length. From the stability group the location of the pilot, and thus the widest point is approximately known. This limits the location of maximum thickness and affects the ideal fineness ratio. In subsection 8.3.2 the limiting dimensions are analysed in detail. Based on an analysis on drag reduction of airplane fuselages through shaping by the inverse method by

Zedan et al. [24] a fuselage with a fineness ratio of 5.5 to 6 and maximum thickness location of approximately 39% of the fuselage length is chosen for the design.

8.3.2 Fuselage shape limiting factors

The design of the ideal fuselage shape as a streamline body of rotation is an exercise in aerodynamic optimisation for minimum drag; it does not take into account the dimensions of the components the fuselage needs to contain and where these are located. The main components to consider, since they have the largest influence on the fuselage shape, are the pilot and engine, or propulsion system. The c.g. location relative to the nose datum line of both these components is determined by the stability group. For more information on the stability analysis the reader is referred to chapter 9.

Pilot

The dimensions of a '90-percentile, male' pilot are taken from tabulated data in Roskam [25, Ch.2]. The pilot is depicted in Fig. 8.6 with letters to indicate various dimensions. The main dimensions used for the pilot are: A=1900, B=990, F=430, G=515, H=1050; all values in millimeters. A table with the complete set of dimensions for the corresponding letters is included in appendix F.

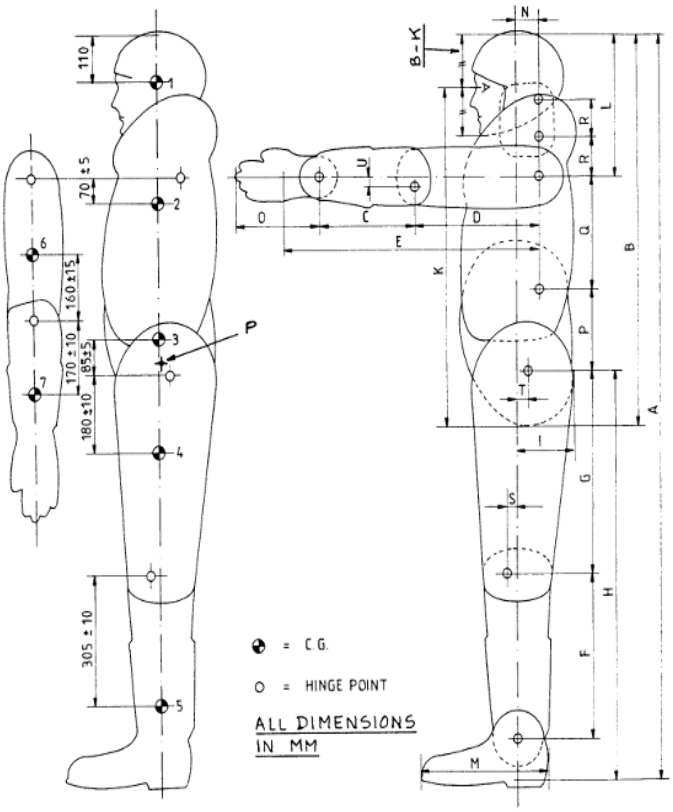

Figure 8.6: Dimensions of standing pilot as taken from Roskam [25, Ch.2]

Once the dimensions of the pilot have been set, the orientation or layout of the pilot within the cockpit needs to be determined. The Red Bull Air Race regulations state that: "The Race Pilot seat shall be designed in a way that the Race Pilot is sitting in the cockpit in an upright position in order to provide sufficient outside front view and side view for the Race Pilot. The Race Pilot lying on his back, front or side is prohibited. Therefore the seat recline angle shall be greater than 30°. This angle is measured between the thrust line and the backrest of the seat."

[1]. The inclination chosen for the Avinya concept is based on its direct competitors, this is a 45° reclined seat layback angle, for an optimal balance between pilot outside visibility, reduction of cockpit vertical clearance and thus frontal area and wetted surface, and accommodating physical effects whilst compying to the regulations [26]. The length wise position of the pilot c.g. in the fuselage is taken from the stability group. The pilot is modelled in the cockpit seating position as shown in Fig. 8.7, and the c.g of the pilot in the seating position is determined. The pilot is placed such that his c.g. location conforms to the stability calculations and the required cockpit dimensions to accomodate the pilot are calculated and then tabulated in Table 8.6. The position of the cross sections are relative to the nose datum line.

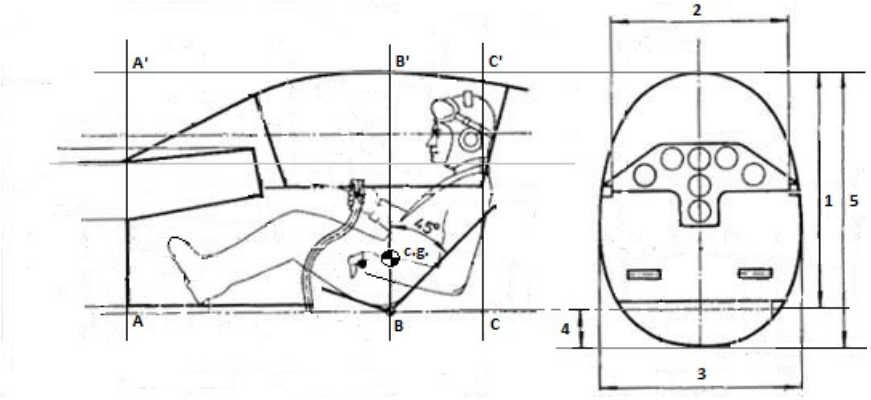

Figure 8.7: Cockpit seating position of pilot and corresponding cross section

Table 8.6: Cockpit cross-section dimensions in [mm]

Cross-section	Location	Clearance (1)	Internal width (2)	External width (3)	Depth (4)	External height (5)
AA'	780	597	680	780	120	717
BB'	1800	943	700	800	146	1089
CC'	2150	903	680	780	120	1023

The location of the pilots c.g is estimated based on the c.g. location of the limbs as shown in Fig. 8.6 and the corresponding weights in appendix F. Cross-section BB' coincides with the pilot c.g. location. The internal width is based on the width of the pilot (appendix F) with an added margin. The external width is equal to the internal width plus a 50$[mm]$ margin on either side to account for the aircraft structure. The clearance is the height of the cockpit as measured from the line running under the pilots seat parallel to the thrust line. The depth is the height underneath this line; this space is reserved for control system linkages such as push rods and electrical cables or similar.

A mock up of the cockpit should be made in the final design phase, assessing the visibility to the pilot, when doing the detailed design for the canopy and cockpit layout. For the conceptual design the assumption has been made that, qualitatively comparing the cockpit dimensions from Table 8.6 to those of the direct competition, the visibility of the pilot is sufficient.

Engine

The RBAR regulations state that the RBAR Race Aircraft to be used in the MASTER class will be equiped with a Standard Power Unit, including [12]:

- Lycoming/Thunderbolt 540-D "Red Bull Air Race" limited series engine
- Sky Dynamics 6 to 1 standard exhaust system
- Christen inverted oil lubrication system

The engines are supplied by Red Bull, and the safety implications of engine failures mean that performance tuning by individual teams is strictly limited in scope. As a result the engine dimensions can be considered constant and standard values from the manufacturers website are used [27]. The values of the enigne dimensions from the manufacturers website in inches, and the corresponding converted dimensions in SI units are presented in Table 8.7.

Table 8.7: Lycoming IO540-D engine dimensions

	Inches	Millimeters
Length	39.34	999.2
Width	33.37	847.6
Height	24.46	621.3

The engine is positioned by the stability group such that the most aft part of the engine coincides with the most aft part of the fuselage, with the propeller directly attached. The dimensions of the fuselage at the engine compartment are estimated based on the engine dimensions with a margin for the structure, a margin for engine subsystems, and space required for engine cooling. The width is estimated at 1000 mm and the height at 800 mm.

8.3.3 Optimisation of fuselage design

With an ideal fuselage shape and limiting dimensions known, the fuselage is modelled in XFLR5 and combined with the model of the wing and canard in order to perform a 3d analysis. It was requested by the 'wing aerodynamics group' that the fuselage design is tweaked in such a way as to minimise induced angle of attack. Following the 3D panel analysis performed in XFLR5, the fuselage splines are edited in the program, optimising pressure distribution along the fuselage, followed by another analysis in an iterative process. For more details on the 3D analysis of the wing fuselage combination and the results the reader is referred to chapter 11.

8.4 Other design influence

It is also important to look at the impact of other design considerations such as landing gear and propellers. These extra factors have significantly low impact on the overall aerodynamics of the aircraft, so will be done mainly analytically.

Landing gear

Landing gears are an important consideration for the aerodynamics and cannot be analysed using XFLR5. It has a significant impact on the zero lift drag of the aircraft. In order to better analyse it an analytical method will be used, shown in section 8.5. It is noted that having a landing gear with small dimensions is beneficial, as it means less obstruction of the streamlines. Adding fairings to the wheels really improves the drag performance, and thus is used in other aircraft's competing in the Red Bull Air Race and will be used in Avinya's design as well.

Propellers

As the vehicle is a pusher propeller it is important to analyse the effect of this configuration on the aerodynamics of the aircraft. Due to the pusher configuration, the angle of attack of the wing influences the position at which the streamlines hit the propeller. So for a high angle of attack the streamlines will mainly hit the bottom part of the prop causing an increase in the AoA. So for a downward rotating blade the thrust and torque will increase and for an upward rotating blade this will decrease [28]. An idea to resolve this could be to have an oval shaped rotation. However this has to be further when proceeding into a detailed design phase.

8.5 Analytical C_{D_0} calculation

Now that the wing and the fuselage have been designed, The C_{D_0} for the entire aircraft needs to be calculated. As mentioned earlier XFLR5 is not effective in calculating the drag coefficient for the entire aircraft, therefore in order to tackle this problem, an analytical method is used [29]. The inputs and outputs used in this solution method are given in Fig. 8.8. The inputs have been divided into control and variable inputs, the control inputs are the ones that always remain the same and the variable inputs have to be changed for each iteration.

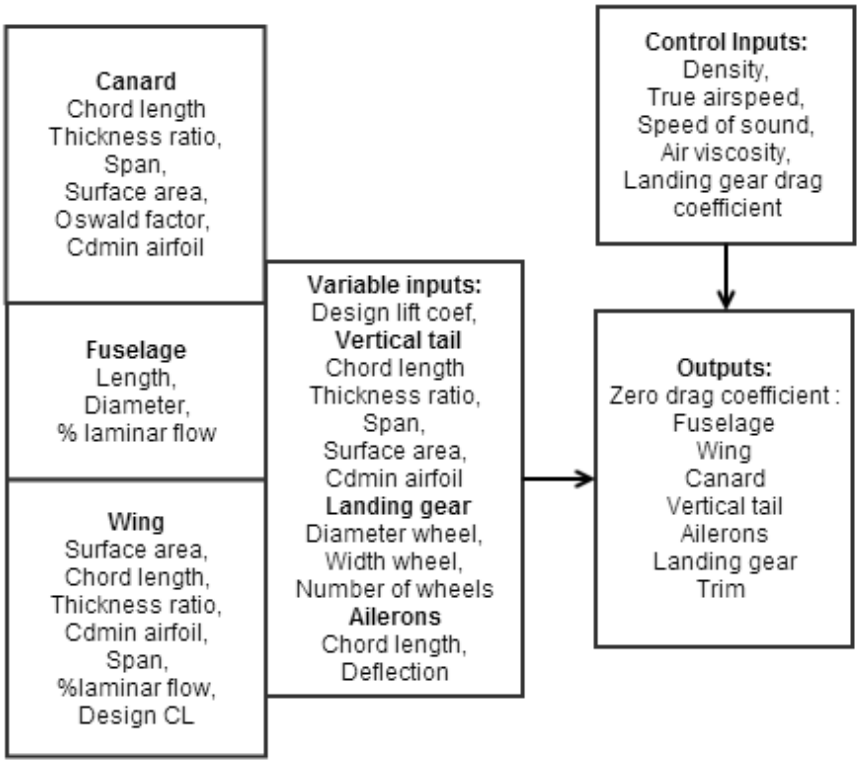

Figure 8.8: Inputs and outputs for aerodynamic calculations

Table 8.8 shows the functions and the final outputs computed for the first iteration optimised for roll rate.

Table 8.8: Analytical method of C_{D_0} calculation [29]

Component	Sub-functions	Final Function
Fuselage	$Re = \frac{\rho * V * l_{fues}}{\mu}$ $C_{f_l urb} = \frac{0.455}{(log_{10}Re)^{2.58}}$ $C_{f_l am} = \frac{1.327}{(log_{10}Re)^{2.58}}$ $f_{LD} = 1 + \frac{60}{(L/D)^3} + 0.0025(\frac{L}{D})$ $f_M = 1 - 0.08 * M^{1.45}$ $S_{wet} = 2[1 + 0.5(\frac{t}{c\,max})]b * C$	$C_{D_{0_f}} = f_{ld} * f_m * (\frac{S_{wet}}{Sw}) * Cf_f$
Wing	$f_{tc} = 1 + 2.7(\frac{t}{c\,max}) + 100(\frac{t}{c\,max})^4$	$C_{D_{0_w}} = C_{f_w} * f_M * f_{tc_w} * (\frac{S_{wet}}{Sw}) * (\frac{C_{D_{min_w}}}{0.004})^{0.4}$
Canard		$C_{D_{0_{ht}}} = C_{f_{ht}} * f_M * f_{tc_{ht}} * (\frac{S_{wet}}{Sw}) * (\frac{C_{D_{min_{ht}}}}{0.004})^{0.4}$
Tailplane		$C_{D_{0_{vt}}} = C_{f_{vt}} * f_M * f_{tc_{vt}} * (\frac{S_{wet}}{Sw}) * (\frac{C_{D_{min_{vt}}}}{0.004})^{0.4}$
Landing gear		$C_{D_{0_{lg}}} = N_{lg} * C_{D_{lg}} * (\frac{S_{lg}}{S})$
Aileron		$C_{D_{0_{ai}}} = (\frac{C_{ai}}{C_w}) * 0.0014 * (\delta_f)^{1.5}$
Trim	$K_t = \frac{1}{\pi * e_t * AR_t}$ $C_{L_t} = (C_L - C_{L_w}) * (\frac{S_t}{S})$	$C_{D_{0_{trim}}} = K_t * C_{l_t}^2 * (\frac{S_t}{S})$
Total		$C_{D_{0_{Total}}} = 1.06 * (C_{L_t} + C_{D_{0_{ai}}} + C_{D_{0_{ht}}} + C_{D_{0_{vt}}} + 1.04 * C_{D_{0_w}} + C_{D_{0_f}})$

Using this method one can calculate the total zero lift drag for each iteration and bypass the inability of XFLR5 to analyze multiple bodies drag influence. While calculating $C_{D_{0_{Total}}}$ one can see that $C_{D_{0_w}}$ has a factor of 1.04, this is to include the influence of wing fuselage interaction. Furthermore it can be seen that the total is multiplied by a factor of 1.06, this is to include factors not included in the calculation namely the cooling drag, surface roughness, antennas and pitot tubes, leakages and last but not least rivets and screws. Note this method is slightly inaccurate, but can be implemented with the results of XFLR5 to improve the drag values generated by the program, considering it is the most sensitive factor as shown in chapter 6. Furthermore it is important to note that for some variables, such as for determining wheel dimensions for the landing gear, reference aircraft data was used.

Chapter 9 - Stability and control analysis

The stability is determined based on updated aerodynamic choices such as airfoil as well as performance parameters such as sweep. This chapter will provide a detailed discussion on the stability analysis conducted during the design process of the Avinya race aircraft. Included in this analysis is the class II weight estimation, as the component weights are a required input for the determination of the range of the centre of gravity for which the aircraft has to be stable and controllable.

In section 9.1 the method used to estimate the component weights is described in detail, followed by an elaboration on the procedure used to determine the needed canard surface area and the longitudinal wing position in section 9.2. The chapter is concluded with the determination of the landing gear position, the required vertical tail surface area and the pilot control forces in sections 9.3 to 9.5.

In Fig. 9.1 a graphical overview of all aspects included in this analysis is given. It displays the inputs and outputs of every process as well as the dependencies on other departments.

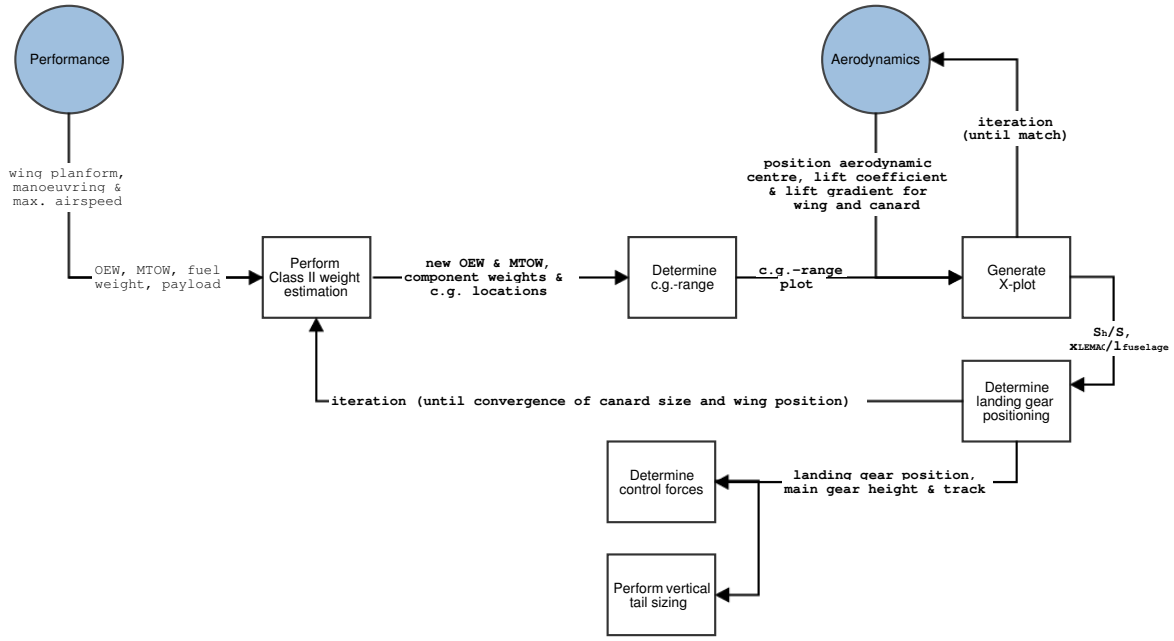

Figure 9.1: Relations and dependencies of the processes involved in the stability analysis

The class II weight estimation uses the main wing geometry supplied by the performance department and the estimates for the OEW and MTOW used therein. The required additional information about the aircraft dimensions needed for the class II estimation is known from previous iterations (in the first iteration, data from reference aircraft was used). Following the component weight estimation is the canard sizing and wing positioning. Included in this procedure is the generation of the c.g.-range and the X-plot, as well as the positioning of the landing gear. Naturally, a change in canard size will change the component weight, which in turn will shift the c.g. position. The weight estimation is thus updated and the new canard size and main wing position determined. Once these two parameters are converged, the surface area of the vertical tailplane that is required for directional stability and the control forces corresponding to the current canard are determined.

9.1 Class II weight estimation

The class II weight estimation is a key aspect of the sizing of the horizontal stabiliser for an aircraft. It determines the weight of the aircraft components which, combined with their c.g. locations, is used to find the centre of gravity of the aircraft at operational empty weight. This section will give an explanation on the method used for the class II weight estimation.

9.1.1 Estimation method

All methods used to estimate the component weights base their predictions on relations derived by complex regression analyses from reference aircraft. Because of the small demand for aerobatic aircraft, there are no methods available for public access that can be used to accurately predict the component weights. It was decided to select a method that was most probable to yield useful results and use the produced component weights as a first, rough, estimate. Once more information on the component dimensions (e.g. spar dimensions etc.) is available, the estimated component weight is replaced by the new, more accurate, prediction. The selected method was developed by the USAF and was taken from [30, Ch.5 - Ch.7]. It is valid for "light and utility type airplanes with performance up to about 300 kts" [30, p.68] which, while not exactly being applicable for aerobatic aircraft, was deemed the most accurate one available. To validate that the USAF method is indeed accurate enough to be used as a first estimate, the dimensions of the Zivko Edge 540 were used to predict their component weights. These estimates, as well as the resulting OEW, were then compared to the actual weights.

Table 9.1 shows the component weights as estimated by the USAF method, the actual weights and the difference in both kilograms and percentages. The real weight for the horizontal stabiliser is the summation of the summation of the horizontal and vertical stabiliser, therefore the difference is only 3kg.

Table 9.1: Comparison of estimated and actual component weights of the Zivko Edge 540, using the USAF method as explained in [30].

Component	Estimated weight [kg]	Real weight [kg]	Difference [kg]	Difference [%]
Horizontal stabiliser	20.00	29.00	3.00	11.58
Vertical stabiliser	12.00	N/A	N/A	N/A
Fuselage	100.00	88.00	12.00	18.38
Landing gear	39.00	38.00	1.00	3.05
Engine	313.00	229.80	83.20	36.16
Fuel system	10.00	N/A	N/A	N/A
Flight controls	48.00	35.00	13.00	37.24
Electrical & instrumentation	15.00	41.00	-26.00	-64.14
Other	0.00	0.00	0.00	0
Wing	103.00	78.00	25.00	31.45
OEW	659.00	540.00	119.00	22.13

At this stage the required accuracy of the weight prediction is 20 %, as the available information is not detailed enough to predict the exact weight of the structure. As such, it becomes apparent that there are four components for which the prediction is less accurate than allowed. The predictions for the weight of the engine, flight controls, electrical & instrumentation and the wing are all of by more than 30 %. Subsequently, the prediction for the total aircraft weight is off by about 22 %, which is at the limit of being unacceptably inaccurate. To refine the weight predictions the four components that were not predicted within the desired accuracy are investigated in more detail to determine why the prediction is off.

The prediction for the engine weight of the USAF method includes the weight of the air induction, the engine mounting structure and engine controls. Analysing the predicted weight of the fuselage in Table 9.1, it can be seen

that the prediction is too heavy again. To account for this it was decided that the engine component weight will consist of only the engine and propeller weight. The weight of the air intake, the engine mounting etc. is assumed to be included in the predicted fuselage weight.
Considering the flight control and the electrical & instrumentation components, it can be seen that the individual differences are large. However, comparing the combined weight of both components, the deviation is reduced to only about 17 %. The overall prediction of the aircraft weight will thus be accurate enough. As the component weights are relatively small, it is additionally assumed that the shift in the position of the centre of gravity due to the inaccurate prediction of the single component weight is negligibly small.
The last component whose prediction deviates substantially from the real weight is the main wing. The predicted weight is more than 30 % heavier than the actual wing. The cause for this is that the USAF method is applicable to light utility aircraft, whose wings are usually made of metal, opposed to the composite materials used in the Zivko. Additionally, the Zivko is optimised for the lowest weight possible. However, because of the placement of the rudders at the wing tips, it is assumed that the weight of the wings of the Avinya will be heavier than of the Zivko. Taking the increased weight because of the vertical tail into account, the accuracy of the wing weight is assumed to be accurate enough.

Overall, the modified weight prediction (reduced engine component weight) is deemed accurate enough to offer estimates of the component weights to be used in the following design.

9.1.2 First iteration

A complication in the first iteration was, that not all aircraft dimensions were known. Besides the wing planform and the canard and main wing airfoil, no detailed information was available. To enable the weight prediction, all data not yet determined was taken from reference aircraft. The aircraft taken were the Zivko Edge 540 as well as the Rutan Long-EZ. The former because it is the main competing aerobatic aircraft and the latter because it is a canard in approximately the same weight category (MTOW of the Long-EZ is 601 kg [31], compared to the 676 kg from the class I weight estimation determined in the mid-term report.
The aircraft dimensions used as a starting point for the class II weight estimation are displayed in Table 9.2 below.

Table 9.2: Aircraft dimensions used as starting point for the class II weight estimation

Parameter	**Main wing**	**Canard**	**Vertical tail**	**Unit**
Span	7.57	4.0	0.90	m
Root chord	1.94	0.64	0.87	m
Tip chord	0.87	0.64	0.68	m
MAC	1.47	0.64	0.76	m
Taper	0.45	1.0	0.72	-
LE sweep	28.0	0	-	deg
1/4 sweep	27.8	0	-	deg
Surface	10.7	2.56	0.675	m^2
Aspect ratio	5.38	6.25	1.20	-
Max t/c @ root	0.14	0.11	0.15	-
Parameter	**Fuselage**	**Unit**		
Tail length	-2.32	m		
Width	0.95	m		
Height	1.27	m		
Length	5.12	m		
Distance nose to root LE	3.18	m		

9.2 Canard sizing

After determining the component weights and the c.g. location of the aircraft, the horizontal stabiliser can be sized. One of the main challenges in designing a canard aircraft is guaranteeing safe operation over all c.g. ranges. During flight, the aircraft has to be stable, pitching down with a sudden increase in angle of attack. Especially for aircraft with reversible flight controls (such as general aviation and aerobatics aircraft) stability is extremely important. In case of a canard it is difficult to find the optimum compromise between the needed stability and the desired manoeuvrability. Additionally, the aircraft has to be controllable during landing where the slow airspeed requires the pilot to fly at large angles of attack. Both criteria (stability and controllability) set a limit for the position of the centre of gravity; the stability for the aft -, the controllability for the forward c.g. location.
To determine the optimum combination of canard surface area and longitudinal wing position, a plot of both the c.g.-range and the c.g.-limits is generated. By overlapping these plots the smallest feasible area ratio S_h/S and the corresponding wing position x_{LEMAC} can be determined. As this method is partially based on the class II weight estimation, an iteration has to be performed where the determined canard surface area and wing position are used to update the weight estimation. Once the weight estimation and the canard sizing converge, the determined surface area and wing position can be used for the further design.

9.2.1 C.g.-range

To determine the required surface area of the canard, it is important to know the range over which the c.g. will travel during operation of the aircraft. The position of the c.g. influences the arm over which the lift generated on the wing and on the canard will act, thus it has a large impact on the required canard size.

For the purpose of sizing the canard surface area, a plot of the travel of the c.g.-range is generated. It shows the location of the most forward and the most aft position of the c.g. as a function of the longitudinal position of the main wing. This plot will be used in combination with the X-plot (discussed in subsection 9.2.2) to determine the optimum combination of canard surface area and the longitudinal main wing position.

To generate this plot, the position of the most forward and the most aft aircraft c.g. location for three different main wing positions are determined. The first for the current aircraft layout, the other two with the main wing shifted by 10 % forward and aft respectively.

The first step is to determine the c.g. location of the aircraft at OEW. Since This will change dependent on the main wing position, the components are grouped into the fuselage and the wing group. The first group concists of all components that remain fixed for all wing positions, while the second groups components c.g. locations are dependent on the wing position.

The final location of the c.g. is determined with the aid of the component weights determined via the class II method detailed in section 9.1 and the c.g. locations of the individual components. For the vertical & horizontal tail, the fuselage and the main wing methods are available that estimate the location of their c.g. positions [30, Ch.8]. The locations for the other components are either estimated from reference aircraft or are selected favourably for the design.

After determining the c.g. location of the aircraft at OEW, the loading procedure of the aircraft is simulated to investigate the range over which the c.g. will travel. Dependent on the position of the pilot, fuel tanks and the storage place for eventual payload, the c.g. will either move forwards or backwards. Because of the position of the main wing and the engine at the back of the aircraft, it is assumed that the pilot as well as the fuel tank are located forward of the c.g. at OEW. The most forward c.g. location is thus at MTOW with both pilot and full fuel tanks on board. The most aft c.g. location is for the aircraft at OEW. However, dependent on the situation, the critical aft c.g. location is not at OEW. The stability is restricting the most aft c.g. location that is allowed during flight. Since the aircraft has to be piloted by a human being, it is unnecessary for the aircraft to be stable without the pilot on board. In this case, the aft c.g. is limited by the c.g. at MZFW.

9.2.2 X-plot

The second tool needed to determine the optimum combination of canard surface area and longitudinal wing position is the X-plot. It shows the ratio of canard surface area and wing surface area dependent on the position of the centre of gravity. The position of the c.g. is given in percentage of, and relative to the leading edge of the mean aerodynamic chord. It consists of two linear functions, one describing the limit due to the stability, the other due to the controllability criteria. The c.g.-range plot is then overlaid onto the X-plot and vertically shifted while keeping the y-axes aligned. Once the overlap of the c.g.-range and the c.g. limits matches, the optimum combination of canard surface area and longitudinal wing position are known.

Stability criteria The limit of the c.g. position from the stability criteria is the neutral point. A c.g. located at this point would result in no change in the pitching moment with a sudden change in angle of attack. Because of the need for high manoeuvrability, it is decided to design the Avinya for relaxed longitudinal stability. The position of the neutral point is found via Eq. (9.1).

$$\bar{x}_{cg} = \bar{x}_{ac} + \frac{C_{L\alpha_h}}{C_{L\alpha_{wf}}} \frac{S_h}{S} \frac{x_{cg} - x_h}{\bar{c}} \left(\frac{V_h}{V}\right)^2 \tag{9.1}$$

Note that the term correcting for the downwash usually encountered on the wing is neglected in Eq. (9.1). For a canard aircraft, this effect is an upwash encountered at the canard and is accounted for in the lift gradient of the main wing. The corrected lift gradient is determined via Eq. (9.2) [32].

$$C_{L\alpha_w}\Big|_{in\ canard\ downwash} = C_{L\alpha_w}\left(1 - \frac{2C_{L\alpha_h}\frac{S_h}{S}}{\pi A_w k}\right) \tag{9.2}$$

The factor k in Eq. (9.2) is a measure of the distance between the aerodynamic centre of the main wing and the canard. If this distance is at least twice the main wing root chord, the factor k is equal to one.

To get a function describing the canard surface area dependent on the c.g. location, Eq. (9.1) is rewritten into Eq. (9.3).

$$\frac{S_h}{S} = \frac{\bar{x}_{ac}}{\frac{C_{L\alpha_h}}{C_{L\alpha_{wf}}}\left(\frac{V_h}{V}\right)^2 \frac{x_{cg}-x_h}{\bar{c}}} - \frac{1}{\frac{C_{L\alpha_h}}{C_{L\alpha_{wf}}}\left(\frac{V_h}{V}\right)^2 \frac{x_{cg}-x_h}{\bar{c}}} \cdot \bar{x}_{cg} \tag{9.3}$$

Controllability criteria To ensure safe operation, the aircraft needs to be able to be trimmed at different angles of attack. The most critical situation is at low airspeeds, when the effectiveness of the tail is lowest. It was thus decided to select the landing configuration as the deciding factor for the controllabilty requirement. Even at these low airspeeds, the moment generated by the canard has to be strong enough to count the pitching moment generated by the main wing. From the moment balance, the following equation describing the c.g. position for the trimmed aircraft is derived.

$$\bar{x}_{cg} = \bar{x}_{ac} - \frac{C_{m_{ac}}}{C_{L_{A-h}}} + \frac{C_{L_h}}{C_{L_{A-h}}} \frac{S_h}{S} \frac{x_{cg} - x_h}{\bar{c}} \left(\frac{V_h}{V}\right)^2 \tag{9.4}$$

It can be noted that opposed to the location of the neutral point in Eq. (9.1), the trim point is dependent on the moment acting in the aerodynamic centre. Furthermore, while the neutral point is mainly a function of the lift

gradients, the trim point depends on the lift coefficients of the canard and main wing.

As with the equation describing the position of the neutral point, Eq. (9.4) is rewritten to show the dependency of S_h/S on the c.g. location. This is displayed in Eq. (9.5).

$$\frac{S_h}{S} = \frac{\bar{x}_a c - \frac{C_{m_{ac}}}{C_{L_w}}}{\frac{C_{L_h}}{C_{L_w}} \left(\frac{V_h}{V}\right) \frac{x_{cg} - x_h}{\bar{c}}} - \frac{1}{\frac{C_{L_h}}{C_{L_w}} \left(\frac{V_h}{V}\right) \frac{x_{cg} - x_h}{\bar{c}}} \cdot \bar{x}_{cg} \tag{9.5}$$

9.2.3 Influential parameters

Depending on the aerodynamic parameters of the canard and the main wing, the gap between the two lines, which indicates the available range between the c.g. limits, may be too small to be matched with the required c.g.-range. For the aircraft to be both stable and controllable, the shape of the X-plot has to be adjusted until a match is accomplished.

Analysing Eqs. (9.3) and (9.5), it can be seen that the slope of the stability curve is dependent on the ratio of the lift gradients $C_{L_{\alpha_h}}/C_{L_{\alpha_{wf}}}$ while the controllability curve depends on the ratio of lift coefficients C_{L_h}/C_{L_w}. Thus it is logical to influence these four paramters to change the X-plot into a desirable shape. Another parameter that can usually be used to change the shape of the X-plot is the stability margin. As the Avinya aircraft is already designed to be neutrally stable, this option cannot be further exploited without the aid of articifial stability.

A problem that presents itself is the interaction of the two requirements. To achieve a steep stability curve, the lift gradient of the main wing has to be as large as possible while the lift gradient of the canard should be as low as possible. On the other hand, to have the controllability curve as flat as possible, the lift coefficient of the main wing has to be lower than the lift coefficient of the canard.

To solve this problem it was decided to modify the elevators on the canard such that they can be used as simple flaps during landing. This allows the canard to be designed such that its lift gradient is as gradual as possible to enable stability during flight while artificially increasing its lift coefficient during landing. Due to this decision, a further parameter to influence the shape of the X-plot is introduced, the change in the lift coefficient due to the elevator/flap deflection ΔC_L.

For the purpose of using the elevators as flaps, an additional control mechanism will be installed that allows the pilot to deflect the elevators into the landing configuration without having to exert a force in the stick.

Once the shape of the X-plot is fixed, the problem of matching the c.g.-range and the c.g. limits is still present. Besides the aerodynamic parameters already mentioned, the component c.g. locations can be adjusted to favourably change the required c.g. range. These locations are limited mainly by the fuselage length, which is another parameter that can be influenced.

When using all these parameters it is possible to match the c.g.-range plot and the X-plot and thus determine the optimum canard surface area and corresponding longitudinal wing position.

9.2.4 Planform considerations

From the X-plot and c.g. range the surface area of the canard and the aircraft configuration are determined. The next step is to design the canard planform. The most important parameters are the aspect ratio, taper, sweep and dihedral angle.

The aspect ratio has to be as high as possible to reduce the induced drag. Also increasing the aspect ratio of

the canard does increase the lift curve slope, which should be similar to the wing lift curve slope [33, Ch.4]. A disadvantage of a high aspect ratio is the increased weight due to the larger moment arm. However, comparison with the Long EZ (aspect ratio of 10.2 [14, Ch.6]) shows that a high aspect ratio is favourable. Finally a high aspect ratio decreases the angle of attack at which the aircraft will stall. This is required because the canard has to stall before the main wing does [34, App.C2].

Besides the aspect ratio, the sweep and taper ratio do influence the stall angle of attack. Increasing either of the latter two does decrease the stall angle of attack. Since a sweep angle makes the required structure more complex and thus heavier it was chosen to have a taper ratio of 1, while not applying a sweep angle. This will lead to the lightest planform with the required stall angle of attack. Also solving the stall characteristics with a sweep angle will be harder than with taper ratio since sweep has minor effect on the lifting characteristics of a canard [35]. Comparing to general aviation aircraft, which usually have a taper ratio of 0.7 to 1, and the Long EZ, taper ratio of 1 and no sweep, this planform seems to be valid [14, Ch.6].

Finally a dihedral angle was considered. However, as for the main wing, this will increase the roll stability which is not needed. Also the highest maximum lift coefficient is found if no dihedral is applied [35]. Therefore no dihedral angle is applied.

9.3 Initial landing gear sizing

With the determined wing position it is now possible to position the landing gear. At this point, only the longitudinal and lateral position of the main and the nose landing gear, as well as the corresponding height and track, will be determined. The sizing of the actual dimensions of the landing gear is part of a later design stage.

9.3.1 Tip-over and ground clearance criteria

The position of the landing gear is subjected to three main constraints: the longitudinal and lateral tip-over criteria and the longitudinal ground clearance.

The tip over criteria ensure that the aircraft will remain balanced on its wheels for the whole c.g. range. Even in situations like the rotation at take-off, the c.g. has to be located in front of the main landing gear. Should this not be the case, the pilot would be required to suddenly change from a pulling to a pushing input on the stick, as the moment due to the weight would suddenly change. Taking the usual pitch angles during take-off into account, the longitudinal tip-over criteria is assumed to require the main landing gear to be located at an angle of 15 $^\circ$ behind the most aft centre of gravity [36, Ch.9].

To provide enough lateral ground stability, a tip-over criteria dependent on the landing gear base and track is applied. The angle between the line connecting the nose and one side of the main landing gear and the centre of gravity has to be below 55 $^\circ$ [36, Ch.9]. An illustration of the longitudinal and the lateral tip-over criteria is presented in Figs. 9.2a and 9.2b respectively.

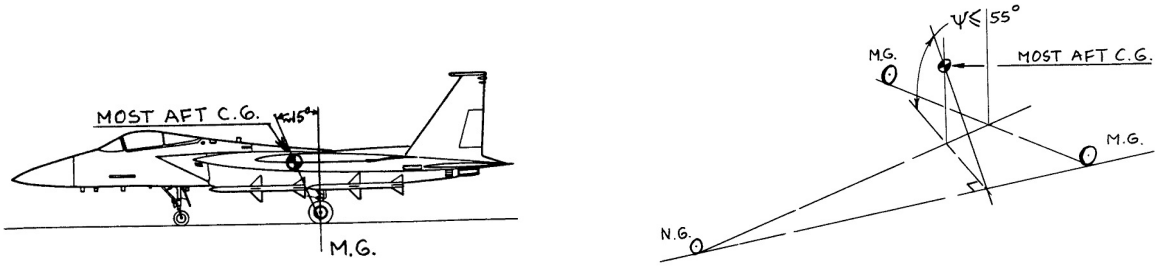

(a) Longitudinal tip-over criteria **(b) Lateral tip-over criteria**

Figure 9.2: Illustrations for tip-over criteria [36, Ch.9]

The last criteria is the ground clearance. During rotation at take-off and during landing the aircraft is at a certain pitch angle. This results in the aft part of the aircraft being closer to the ground. The landing gear has to be positioned such that at no point the aircraft will be damaged. The ground clearance angle of $\theta \approx 15°$ displayed in Fig. 9.3 is suggested by Roskam [36, Ch.9]. The actual angle used was selected based on the needed angle of attack during landing. A safety margin of 5 ° between landing angle of attack and ground clearance angle was selected to account for eventual turbulence. For the Avinya it has to be checked whether the propeller or the lower edge of the vertical tail on the wing tips is more critical. The propeller mounted at the end of the fuselage extends below the aircraft, increasing the necessary landing gear height. The same applies for the rudder, as it too extends downwards, in this case below the main wing.

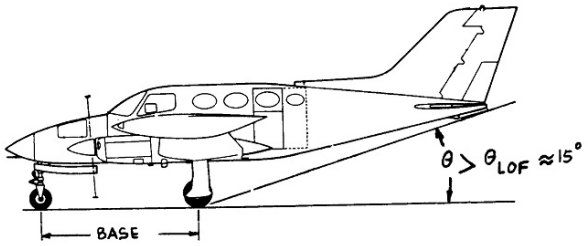

Figure 9.3: Illustration of longitudinal ground clearance criteria [36, Ch.9]

9.3.2 Main and nose gear positioning

The first step in determining the landing gear positioning is to find the required location of the main gear. It is positioned such, that it is located at an angle of 15 ° behind the most aft centre of gravity. Simultaneously, it is checked that the height is sufficient to guarantee the desired ground clearance angle of 5 ° more than than landing angle of attack.

Once the main landing gear position is known, the nose gear location is determined via a simple moment balance about the aft centre of gravity. Assuming a distribution of the total weight over the nose and main landing gear, the distance from the nose gear to the aft c.g. d_{nose} is determined via:

$$d_{nose} = \frac{percentage\ carried\ by\ main\ gear}{percentage\ carried\ by\ nose\ gear} \cdot d_{main} \tag{9.6}$$

where d_{main} is the horizontal distance from the main gear to the aft centre of gravity. When selecting the percentages

it has to be taken into account, that for sufficient ground manoeuvrability, at least 8 % of the take-off weight has to be carried by the nose gear [36, Ch.9].

With the longitudinal positions of both the nose and main gear fixed, the main gear track w_{lg} is determined. As shown in Fig. 9.2b, the angle between the line connecting the nose and main gear and the most aft c.g. has to be smaller than 55 °. To comply with this requirement the track was simply selected such that this requirement was met.

It has to be noted that, after determining the longitudinal landing gear positions, the new location of the centre of gravity of the combined landing gear was determined. For this purpose the weight estimate of the class II weight estimation was distributed over the nose and the main gear. The new c.g. location was then used to update the current estimate used in the weight estimation.

9.4 Vertical tail sizing

To get a first estimation of the vertical tail, reference aircraft were used. This tail size was used for a longitudinal stability analysis, which gave the length of the tail arm. This arm length is, in turn, used to achieve a more accurate tail size. The method used is described by Roskam [36, Ch.11]. The updated tail size is taken back into the class II weight estimation.

Roskam sizes the vertical tail with Eq. (9.7) [36, Ch .11].

$$C_{n_\beta} = C_{n_{\beta_{wb}}} + C_{L_{\alpha_v}} \frac{S_v}{S} \frac{l_v}{b} \tag{9.7}$$

In this equation $C_{n_{\beta_{wb}}}$ is the aerodynamic yawing moment coefficient of the wing-body. For the conceptual design, this value is assumed to be 0, as can be done according to Roskam [37, Ch.10]. The lift gradient of the vertical tail ($C_{L_{\alpha_v}}$) is an airfoil dependent parameter, it is found by the aerodynamics department. The value of l_h is estimated to be the distance between the c.g. of the entire aircraft and the c.g. of the vertical tail. This distance depends on the wing span and sweep and is thus changing with the longitudinal stability iterations. Finally to compute C_{n_β}, it has to be decided whether the aircraft is inherently stable or de-facto stable. Since the aircraft only has a mechanical control system, it has to be inherently stable which gives that C_{n_β} is 0.001 per degree [36, Ch .11]. Now all parameters from Eq. (9.7) are known and the vertical tail size is found.

9.5 Control forces

After stability was achieved and the control surfaces were sized, the forces on the control stick are calculated. These forces are calculated with a method for general aviation aircraft. However, in aerobatic aircraft the forces are usually lower due to the use of balancing spades as described for the ailerons in subsection 7.3.3. This is not taken into account here since the sizing of these parts is for the detailed design. Therefore the forces computed in this section are higher than those of the final design.

The general equation to calculate the stick force is:

$$F_e = \frac{d\delta_e}{ds_e} s_e \bar{c}_e \left(\frac{V_h}{V}\right)^2 \left(\frac{W}{S}\frac{C_{h_\delta}}{C_{m_{\delta_e}}}\frac{x_{cg} - x_{n_{free}}}{\bar{c}} - \frac{1}{2}\rho V^2 C_{h_{\delta_t}} \left(\delta_{t_e} - \delta_{t_{e_0}}\right)\right) \tag{9.8}$$

Several assumptions and estimations have to be made in order to solve this equation. Starting with the control gearing $\left(\frac{d\delta_e}{ds_e}\right)$, it is assumed that the elevator can deflect 10° upward and 20° downward. Furthermore it is assumed that the maximum stick deflection is 20 cm, leading to a control gear of 2.1 rad/m. The speed ratio, wing loading, elevator area (s_e) and elevator chord ($\bar{c}_e$) are found in sections 7.2 and 9.2 and subsection 7.1.3. Then the control

surface deflection moment (C_{h_δ}) has to be calculated, this is done with the method described by Roskam [37, Ch.10].

The corresponding equation is given in Eq. (9.9). Where the ratio of $C_{h_\delta}/C''_{h_\delta}$ is found from a graph [37, Ch.10] and C''_{h_δ} is found with Eq. (9.10).

$$C_{h_\delta} = \frac{C_{h_\delta} \cdot C''_{h_\delta}}{\sqrt{1-M^2}} \tag{9.9}$$

$$C''_{h_\delta} = \frac{C'_{h_\delta}}{C_{h_{\delta_{theory}}}} C_{h_{\delta_{theory}}} + 2C_{h_{\delta_{theory}}} \left(1 - \frac{C'_{h_\delta}}{C_{h_{\delta_{theory}}}}\right) \left(tan\left(\frac{\Phi''_{te}}{2}\right) - \frac{t}{c}\right) \tag{9.10}$$

In which the dimensionless coefficients and the coefficient ratios are found from the graphs in Roskam [37, Ch.10]. The value of t/c and c_f/c as needed for the graphs are computed by the aerodynamics department. The angle for Φ''_{te} is measured to be 18°.

The next coefficient which has to be found in order to solve Eq. (9.8) is the moment coefficient due to the elevator deflection ($C_{m_{\delta_e}}$).

$$C_{m_{\delta_e}} = \frac{C_N}{\Delta\delta_e} \frac{\Delta x_{cg}}{\bar{c}} \tag{9.11}$$

The value for C_N is approximated with the C_L of the main wing. The elevator deflection (δ_e) is found in subsection 7.1.3. The change in c.g. position due to the elevator deflection (Δx_{cg}) is very small and estimated to be 6% of the main wing chord length.

Finally the c.g. position of the stick free situation has to be calculated. From the class II weight estimation the c.g. position of the stick fixed case is known. Using Eq. (9.12) the stick free c.g. position is found.

$$\frac{x_{n_{free}} - x_{n_{fix}}}{\bar{c}} = -\frac{C_{n_{h_\delta}}}{C_{N_\alpha}} \frac{C_{h_\alpha}}{C_{h_\delta}} \left(1 - \frac{d\varepsilon}{d\alpha}\right) \left(\frac{V_h}{V}\right)^2 \frac{S_h l_h}{S\bar{c}} \tag{9.12}$$

Here C_{N_α} and $C_{n_{h_\delta}}$ are received from the aerodynamics. The value for $\frac{d\varepsilon}{d\alpha}$ is neglected since the canard is almost two root chords in front of the main wing. Furthermore C_{h_α} is found with the same method as C_{h_δ} and described by Roskam [37, Ch.10].

The last terms of Eq. (9.8) are neglected, since there will be no trim tab installed. There will be no trim tab since the first estimation of the control forces was about 1kg per degree deflection, which can be flown without trim tab. Though the option of a balancing spades stays, since it is beneficial to lower the forces during pitching.

Chapter 10 - Structural analysis and sizing

Given previous chapters focuses on performance, the structural draws attention to feasibility with stress analysis and sizing. Attention is provided to the structural sizing and stress analysis methods applied during the design of the wing, canard and fuselage. For each component the stresses were first modelled, these stresses were then used in conjunction with material considerations to size elements such that they could bear the loads expected during the mission. The main driver is mass reduction and compliance of structural integrity with the ultimate load factor. A discussion on sustainability, manufacturability and modularity is elaborated upon in chapters 13 and 17.

The internal relationships with respect to other departments and the requested input and output used in and resulting from the structural analysis and sizing are shown in Fig. 10.1.

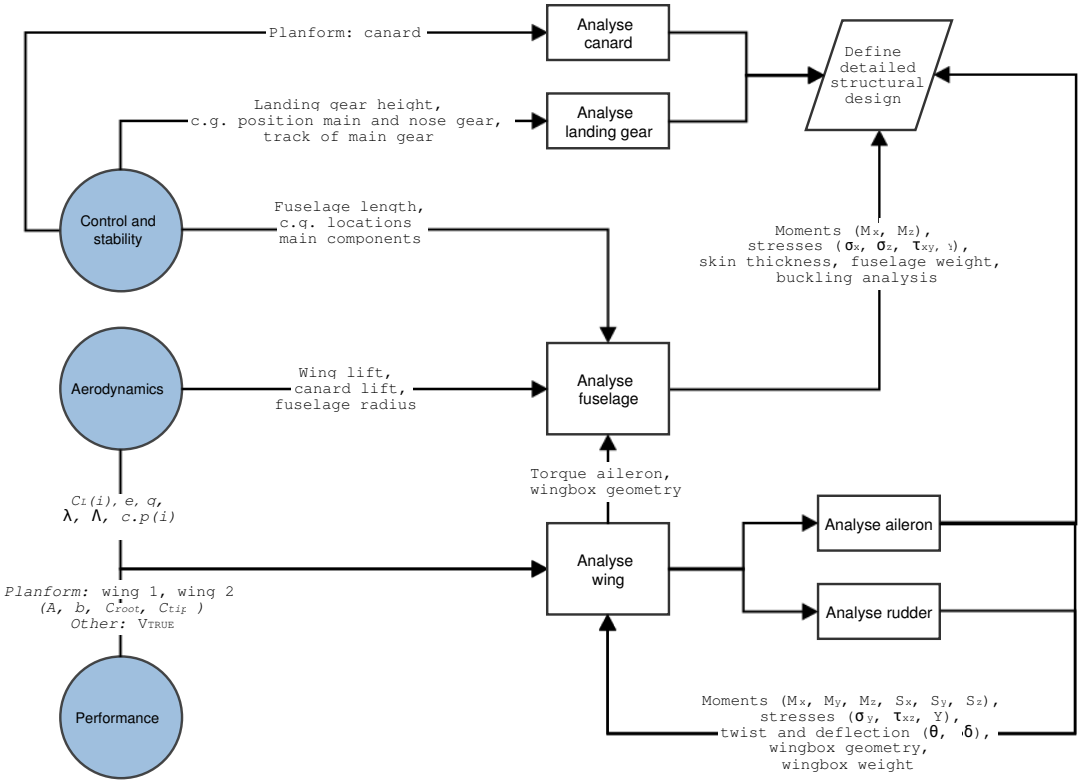

Figure 10.1: Relations and dependencies of the processes involved in the structural analysis

Firstly, in section 10.1 the internal structure of the main wing is analysed including the interaction with the aileron and rudder, followed by a discussion on the internal structure of the canard in section 10.2. The fuselage will conjoin the major components into one supporting structure which is explained in section 10.3. For all sections and structural components the assumptions used are stated and discussed. The subsequent section, section 10.4, elaborates upon the material selection, as performed in the mid-term report. To conclude this chapter an explanation on how the calculations and results are verified for the wingbox sizing and fuselage structure is give in section 10.5.

10.1 Wingbox sizing

The main component to be sized during wing design is the wingbox. The Avinya wing in particular is a complicated structure given the inclusion of wingtip rudders (in the absence of an aft horizontal tail, discussed in subsection 10.1.2) and large ailerons (discussed in subsection 10.1.1) which will introduce additional forces and moments. In addition, the wingbox geometry deviates from the wing geometry, as the wingbox runs straight through the fuselage, introducing additional stresses at the root.

The wing design as described in the mid-term report was subjected to multiple modifications. These adjustments were necessary, as the progression in the design process made more detailed information from the performance, aerodynamics, stability and control departments available. The major adjustments to the initial wing planform are stated below.

1. Increase in sweep angle $\Lambda_{0.25c}$ from 5° to 25° with respect to the design as described in the mid-term report. As a result a significant increase in bending moment around the longitudinal axis of the wing (y-axis) and thus, more wing twist is introduced.
2. Sizing of the vertical tail and rudder. Opposed to the mid-term report, the forces created by the rudder are now properly modelled as a distributed load. Additionally, the bending moments and shear forces acting at the wing - vertical tail intersection were included in the analysis.
3. Sizing of the ailerons. The change in forces and moments due to a deflection of the aileron was added to the simulation. Depending on the deflection of the aileron, this either results in a stress relief or increase.

During the conceptual design of the Avinya, some assumptions have to be made in order to facilitate the process of wingbox sizing, namely:

- Skin gradient between front and rear spars is linear and not curved.
- The wingbox is symmetrical about its horizontal axis, resulting in $I_{xz} = 0$.
- Wingbox front and rear spar positioned with constant chord ratio.
- The wingbox is positioned in accordance with airfoil geometry, with front spar at location of highest thickness over chord ratio for the chosen airfoil, at 29.5%, and rear spar at 70% of local chord.
- The lift distribution with respect to the horizontal axis of symmetry of the wing is assumed to be linear with respect to chord.
- The lift distribution with respect to the longitudinal axis along the wing, is approximated by a multiple degree polynomial.
- This lift distribution is modelled at maximum angle of attack ($\alpha = 18°$) without the occurrence of flow separation, resulting from analysis in section 8.1.
- Lift acts perpendicular to the horizontal axis and at 25% of chord (in front of the shear centre), resulting in a positive moment around the longitudinal and horizontal axis.
- Wing weight acts perpendicular to the horizontal axis and in the centroid (afterwards of the shear centre), resulting in a positive moment around the longitudinal axis and negative moment around the horizontal axis.
- Drag force acts through horizontal axis of symmetry of the wingbox, resulting in a negative moment around the vertical axis.

The structural design process continues with defining the limit load factor for the structural components. As stated in the regulations [1], the limit manoeuvring load factor for which the aircraft is designed and permitted to operate is ±10g with a minimum safety factor of 1.5. Therefore, the wing, empennage and control surface attachment structures have to be sized for an ultimate load factor of ±15g.

Initially, the main loads acting on the wing, being the lift force, drag force and wing weight itself, are mapped. These loads are determined from the weights determined in the class II weight estimation and the ultimate load

factor. The wing weight distribution is assumed to be parabolic, as the wing is tapered in both chord and thickness, with the weight of the vertical tail introduced as a point load at the wing tip. From the regulations [1] it is known that during the race no fuel may be stored in the wings. Thus there is no weight added to the wing due to stored fuel.

The lift distribution along the wingspan is determined by VLM. A detailed explanation on how and why this method is used can be found in section 8.1. A polynomial curve-fit on the lift coefficient as a function of induced angle of attack of one wing with respect to its semi-span is derived from the graphical data as obtained in section 8.1. The same approach is used in the determination of the drag distribution. In the stress analysis the wing is discretised into 500 nodes (N) which corresponds to 499 sections. For each section, the lift and drag are determined using Eqs. (10.1) and (10.2). .

$$L(i) = q_i \cdot C_L \cdot c(i) \cdot l_i \cdot n_{max}; \quad D(i) = q \cdot C_D \cdot c(i) \cdot l_i \tag{10.1}$$

$$C_D(i) = C_{D,0} + \frac{{C_{L,max}}^2}{\pi \cdot A \cdot e} \tag{10.2}$$

The local chord $c(i)$ and the semi-spanwise location $y(i)$ are calculated with Eq. (10.3). They are required for the calculation of the moments, torques and shear forces in subsection 10.1.3.

$$c(i) = c_t + \frac{2(c_r - c_t)}{b_{wing}} \cdot \left(\frac{b_{wing}}{2} - y(i) \right); \quad y(i) = \frac{b_{wing}}{2} - \frac{l_i}{2}(i-1) \tag{10.3}$$

As the stress analysis of the wingbox is performed numerically, the step size can be adapted in correspondence to accuracy required and computational run time available. The section length that is then used is defined in Eq. (10.4).

$$l_i = \frac{b_{wing}}{2(N-1)}; \quad (N = 500) \tag{10.4}$$

An discussion on the considered moments induced asides from those due to lift, drag and weight acting on the main wing is elaborated upon in subsections 10.1.1 and 10.1.2. The governing equations for the shear forces and moments (or torques) of any considered component are shown in Eqs. (10.5) and (10.6). These shear forces and bending moments are calculated from tip towards root. Starting at the tip of the vertical stabiliser and rudder, towards the wing tip and from there onward towards the root of the wing. The components, as shown in Table 10.2, after discussing the interaction of aileron and vertical stabiliser, are superimposed in order to gain the total shear forces and moments applied on the wingbox.

$$S_{x,comp} = \pm \sum_{i=1;}^{i=N-1;} F_{x,comp}(i); \quad S_{y,comp} = \pm \sum_{i=1;}^{i=N-1;} F_{y,comp}(i); \quad S_{z,comp} = \pm \sum_{i=1;}^{i=N-1;} F_{z,comp}(i) \tag{10.5}$$

For each component inducing torques or moments, different moment arms with respect to the shear centre have to be calculated. Along the wing and within each section these moment arms change value. Therefore, the variables constituting these moment arms, a_m are provided in section 10.1.

$$M_{x,comp} = \pm \sum_{i=1;}^{i=N-1;} F_{z,comp}(i) y_i; \quad M_{y,comp} = \pm \sum_{i=1;}^{i=N-1;} F_{z,comp}(i) a_{m,i}; \quad M_{z,comp} = \pm \sum_{i=1;}^{i=1:N} F_{x,comp}(i) \cdot y_i \tag{10.6}$$

Table 10.1: Moment arm

Component	$a_{m,i}$
Lift	$\frac{w_i}{2} + \eta_i + (0.295 - 0.25) \cdot c(i) + X_i$
Weight	η_i
Aileron	$\frac{w_i}{2} + X_i + \eta_i + 0.25 \cdot a_w c(i) \cdot$
Rudder	z_i

In order to apply the above moment arms and shear force and moments equations, the variables as stated in section 10.1 have to be defined. Therefore, the next step is to determine the centroid and the moments of inertia of the wingbox. This is done based on the simplified wingbox geometry shown in Fig. 10.2 via Eqs. (10.7) to (10.9). The geometry of the wingbox such as spar and skin thickness has a large influence on the stresses within. It is also dependent on the choice of material, as varying ultimate yield stresses may require for the geometry to be adapted. Hence, an iteration with respect to spar and skin thickness, resulting stresses and wingbox weight is conducted.

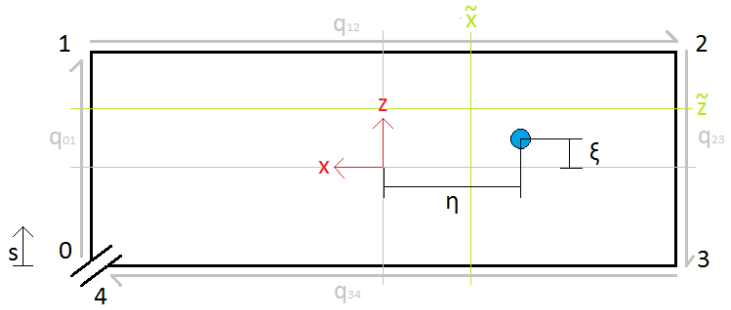

Figure 10.2: Wingbox section as located in the airfoil with cordinate system

$$X = \frac{\frac{w_i}{2} h_i \cdot (t_r - t_f)}{(t_t + t_b) w_i + (t_f + t_r) h_i}; \quad Z = \frac{\frac{h_i}{2} w_i \cdot (t_t - t_b)}{(t_t + t_b) w_i + (t_f + t_r) h_i} \tag{10.7}$$

$$I_{xx} = \frac{(t_f + t_r) \cdot {h_i}^3}{12} + Z^2 \cdot (t_f + t_r) \cdot h_i + \left(\frac{h_i}{2} - Z\right)^2 t_t \cdot w_i + \left(\frac{h_i}{2} + Z\right)^2 t_b \cdot w_i \tag{10.8}$$

$$I_{zz} = \frac{(t_t + t_b) \cdot {w_i}^3}{12} + X^2 \cdot (t_t + t_b) \cdot w_i + \left(\frac{w_i}{2} - X\right)^2 t_r \cdot h_i + \left(\frac{w_i}{2} + X\right)^2 t_f \cdot h_i \tag{10.9}$$

Since the thicknesses of the spars and skins can differ, the shear centre does not necessarily coincide with the wingbox' geometric centre. Determining the position of the shear centre is of great importance, as all forces and moments stated in subsection 10.1.3, are calculated with respect to this point. The shear centre is calculated using Eqs. (10.10) to (10.12). In case the shear forces are acting in both x- and z-direction, Eq. (10.10) will be applied twice to solve for η and ξ. To solve for the shear stresses, the constant and basic shear flow (Eqs. (10.11) and (10.12)) are superimposed with the shear due to torque as stated in Eq. (10.13).

$$S_x\eta - S_z\xi = \oint pq_{b,i} + 2Aq_{s,0} \tag{10.10}$$

$$q_{b,i} = -\left(\frac{S_xI_{xx} - S_zI_{xz}}{I_{xx}I_{zz} - {I_{xz}}^2}\right)\int_0^s t_i x ds - \left(\frac{S_zI_{zz} - S_xI_{xz}}{I_{xx}I_{zz} - {I_{xz}}^2}\right)\int_0^s t_i z ds \tag{10.11}$$

$$q_{s,0} = -\frac{\oint q_b ds}{\oint ds}; \quad q_T = -\frac{M_{y,i}}{2A}; \tag{10.12}$$

$$\tau_i = \frac{q_{b,i} + q_{s,0} + q_T}{t_i} \tag{10.13}$$

With the shear stresses, shear forces and moments known, the normal stress due to bending at each section is calculated via Eq. (10.14). These two stresses are then used to determine the Von Mises stress as shown in Eq. (10.15).

$$\sigma_{y,i} = \left(\frac{M_zI_{xx} - M_xI_{xz}}{I_{xx}I_{zz} - {I_{xz}}^2}\right)(x - X) + \left(\frac{M_xI_{zz} - M_zI_{xz}}{I_{xx}I_{zz} - {I_{xz}}^2}\right)(z - Z) \tag{10.14}$$

The determined Von Mises stress is then used to size the wingbox for minimum weight. This is done by determining the geometry required for different material choices and compare the respective weights. In this way it is guaranteed that the wingbox structure is as light as possible.

$$Y_i = \sqrt{\frac{1}{2}\left[(\sigma_x - \sigma_z)^2 + (\sigma_y - \sigma_z)^2 + (\sigma_z - \sigma_x)^2\right] + 3{\tau_{xy}}^2 + 3{\tau_{yz}}^2 + 3{\tau_{yz}}^2} \tag{10.15}$$

Now that the methodology is outlined, an short discussion on the influence of aileron and vertical stabiliser is provided. In addition, the assumptions not yet stated, specifically for the aileron and horizontal stabiliser are stated.

10.1.1 Aileron

The aileron induces both additional shear forces and bending moments when deflected upward or downward. The weight of the aileron is included in the class II wing weight estimation, and is therefore not considered as an individual weight component. It is located from 20% to 95% of the semi-span, from root to tip, and has a deflection range of $\pm 25°$. The lift distribution as generated by the aileron can be modelled, using the $C_{L_{d\alpha}}$ as derived in Eq. (7.10) from subsection 7.3.1.

The major simplification that is implemented is that the aileron only introduces a force in vertical direction with respect to the airfoil. No horizontal force is generated, like drag, which is an simplification that might influence the model's accuracy. The increase of drag due to deflection, or increase of profile drag, causes the aircraft to yaw, asides from rolling. But, the following statement justifies the simplification: an increase in drag due to maximum aileron deflection for aircraft with relatively short wingspan and large aileron, is considered of small influence on the rolling speed [13, Ch. 12]. Therefore, only the force that is causing the roll is taken into account with the structural analysis. The same assumption is made for the forces generated due to deflection of the rudder in subsection 10.1.2.

For the implementation of the aileron, the following assumptions were added:

- The aileron does not generate a force while in neutral position.
- Aileron force acts perpendicular to the horizontal axis and at 25% of aileron chord, causing either a positive or negative moment around the longitudinal and horizontal axis.
- The increase in drag due to maximum aileron deflection is negligible in comparison to the drag generated by the wing. Therefore, only the force that is causing the roll is taken into account with the structural analysis.

If fully deflected, the aileron generates a shear force parallel to the lift in either negative or positive direction. Additionally, either a positive or negative moment around both the horizontal and longitudinal axis of the wing is induced. The moment around the horizontal axis imposes a torque on the fuselage. This torque is taken into account while analysing the fuselage, as done in section 10.3.

The force generated by the aileron as a function of deflection and spanwise location are determined via Eqs. (7.9) and (7.10) from subsection 7.3.1.

10.1.2 Vertical stabiliser and rudder

For the vertical stabiliser located at the wing tip a symmetrical airfoil is used, being the NACA 0015. Due to this symmetrical airfoil, some additional assumptions can be applied with respect to the loads imposed. The rudder is located from 0% towards 100% of the vertical stabiliser height and has a deflection range of $\pm 25°$.

- The rudder does not generate lift or a force in longitudinal direction with respect to the main wing while in neutral position.
- With the rudder in neutral position, the airflow is assumed to hit the rudder with zero angle of attack with respect to the symmetrical airfoil.
- The vertical stabiliser is not symmetrical with respect to the horizontal axis of the wing. Therefore, if deflected, the rudder force distribution will have a resultant force generating a moment.
- Rudder force acts through the longitudinal axis of the wing at 25% of rudder chord, causing either a positive or negative moment around the vertical axis and horizontal axis.
- The force distribution as generated by the rudder is a uniform distributed load.
- The rudder length is defined as 30% of the maximum horizontal stabiliser chord.
- The drag distribution as generated by the vertical stabiliser will have a resultant drag generating a moment around the longitudinal axis of the wing.

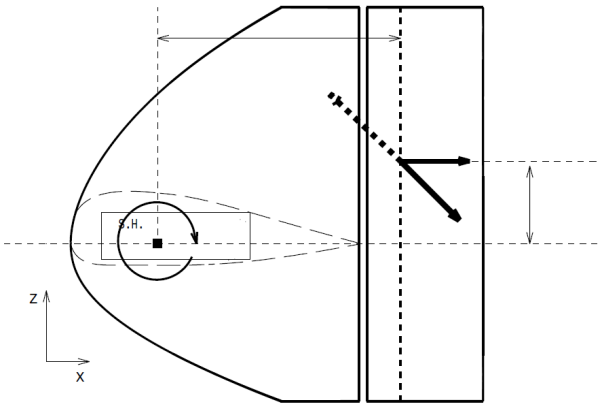

Figure 10.3: Sideview of rudder with resulting forces and moment arms

If fully deflected, the rudder generates a shear force perpendicular to xz-plane, as shown in Fig. 10.3. This shear force is translated into either a compressive or tensile force induced on the wingbox, depending on positive or negative deflection of the rudder. Additionally, this force introduces either a positive or negative moment around both the vertical and horizontal axis of the wing. The drag generated when deflecting the rudder is also inducing a moment about the longitudinal axis of the wing. An overview of the rudder geometry and the moment arms with respect to the wingbox shear centre is shown in Fig. 10.3. The rudder is discretised into nodes and sections ($N = 75$) and the same approach as for the wing and aileron is used to calculate shear forces and bending moments or torques acting on the wingbox. These are then superimposed with the forces and moments acting on the wing.

10.1.3 Rudder and aileron interaction

With the multiple components of forces and moments introduced on the wingbox, a distinction for the ultimate load combination has to be made. In Table 10.2 an overview of all forces and moments imposed is shown. The sign of the forces and moments due to the aileron and rudder can change, thus multiple load cases have to be analysed.

Table 10.2: Overview of all forces and moments present

Component	Type of load	
Wing	Shear forces [N]	$S_{x,drag}$
		$S_{z,lift}$
		$S_{z,weight}$
	Bending moments (torques) [Nm]	$M_{x,lift}$
		$M_{y,lift}$
		$M_{x,weight}$
		$M_{y,weight}$
		$M_{z,drag}$
Aileron	Shear forces [N]	$S_{z,aileron}$
	Bending moments (torques) [Nm]	$M_{x,aileron}$
		$M_{y,aileron}$
Vertical stabiliser	Shear forces [N]	$S_{x,drag}$
		$S_{y,rudder}$
	Bending moments (torques) [Nm]	$M_{x,rudder}$
		$M_{y,rudder}$
		$M_{z,rudder}$

A possible load case is illustrated in Fig. 10.4 for the right wing. The downward deflection of the aileron generates a positive force upward and positive moment around horizontal and longitudinal axis. The deflection of the rudder outward generates a force inward and positive moments around horizontal axis and negative moment around vertical axis. This specific load case results in the highest stresses and can be considered the load case for which the wingbox is sized. An opposite load case, with aileron deflected upward and rudder deflected inward provide stress relieve on the wingbox structure, as the moments induced counteract the moments resulting from the wing weight and lift distributions. For the explanation of moments the right wing was taken as an example.

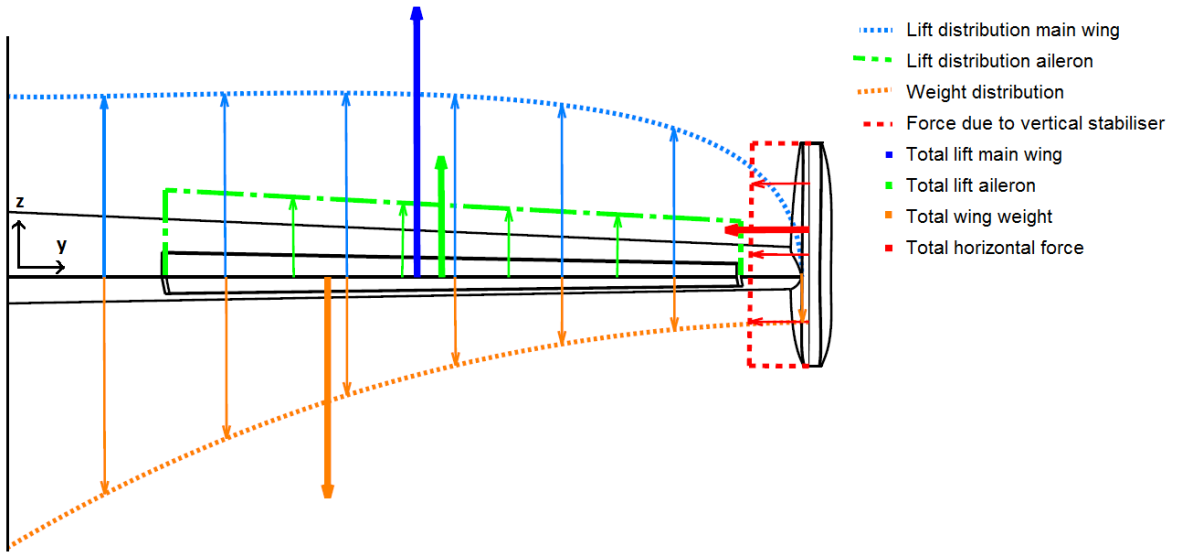

Figure 10.4: Ultimate load case, aileron deflected downward, rudder deflected outward, with indicated forces

After defining the ultimate load case, all shear forces and moments induced by all components within the wing can be superimposed to calculate the stresses along the wingbox. The equations used for this have been stated before in Eqs. (10.13) to (10.15). The results from the stress analysis, such as final wingbox dimensions, weight, cost and stresses, are stated in section 11.2.

10.2 Canard and elevator

For the canard the same tool as for the main wing is used, as it is subjected to the same types of loads and can be considered a smaller version of a wing. The main differences are the smaller dimensions of the canard, absence of sweep and vertical tail at the wing tips. Just as with the wing, the canard is equipped with a control surface along its trailing edge. The elevator extends from 30% to 100% of the canard semi-span, taking into account available semi-span due to local fuselage radius and required control surface for stability and controllability reasons. Whereas the aileron is able to deflect up and down $\pm 25^\circ$, the elevator has a range of 15° deflection downward. For the canard two modifications with respect to the mid-term report have been implemented:

- The canard has no sweep, thus no additional moments due to sweep are induced.
- The canard is not tapered, which changes the lift distribution.

With the canard planform and the corresponding lift- and drag distributions (from section 8.1) known, the shear forces and moments can be calculated using the same method as discussed before in section 10.1. The results for the wingbox of the canard, such as final wingbox dimensions, weight, cost and stresses, are not stated in section 11.2, as it is a repetition of the process and similar results in comparison with the main wing wingbox sizing. The results and discussion are however added in appendix D, for the interested reader.

10.3 Fuselage

In order to analyse the fuselage structure, the dimensions of the wingbox for both the canard and the wing, and the shear forces, moments and stresses acting at the connection of wingbox with fuselage have to be known. These loads introduce moments within the fuselage depending on their location within.

The fuselage structure consists of a skin placed over a truss structure. The analysis of the fuselage structure involves determining the stresses that occur throughout the structure, identifying locations with high stresses and using the stress analysis as a motivation for material choice. The purpose of this section is to present the methodology used

to determine stresses along with all assumptions that are applied. In addition a suitable skin material, thickness and truss structure sizing are determined from the stress analysis.

The assumptions applied during fuselage stress analysis and sizing are as follows:

- Skin is effective under shear
- Truss structure bears axial loads
- Fuselage is a thin walled structure
- Fuselage cross section shape can be approximated by a circle
- Fuselage is assumed to deform around its centre of gravity, where the c.g. is obtained from the class II weight estimations. The fuselage is thus modelled as being clamped at its c.g. (see Fig. 10.5)
- Wing and canard lift loads can be modelled as point loads at the quarter chord location of the aforementioned components
- Moments are introduced into the structure as a result of the wingbox being 'clamped' into the structure in the centre of the fuselage
- Aileron deflection causes larger lift in one wing and therefore introduces a torsion load in the fuselage
- The propeller thrust can be modelled as a direct stress along the longitudinal axis of the aircraft

To begin with the fuselage is modelled in MATLAB as a beam under point loads, namely the canard and wing lift. A visual representation of this is found in Fig. 10.5 below:

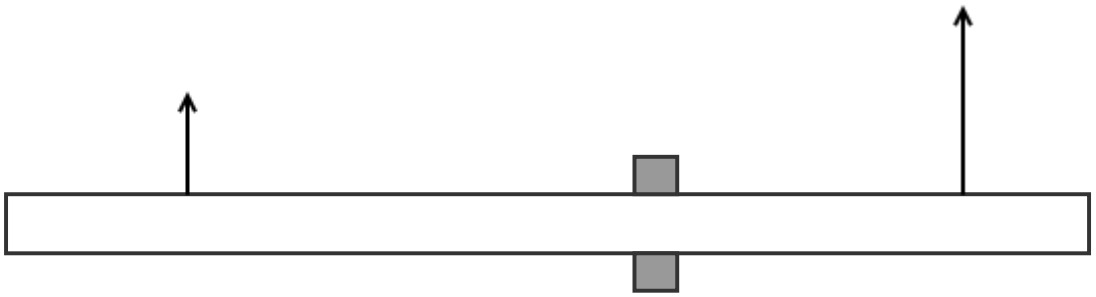

Figure 10.5: Fuselage cantilever beam model

The beam is divided into equal length sections from the nose to the tail and the stress in each section is determined. Similarly the circumference is broken up into piecewise sections and the stress at each point around the circumference computed. Furthermore the fuselage is given a linear taper from nose to tail given that the dimensions of the actual fuselage will also follow a similar change in dimensions towards the tail due to the engine situated in the rear.

Specifically the radius varies from 0.4 to 0.5m across the length of the fuselage. This can be seen in the 3D representation given below:

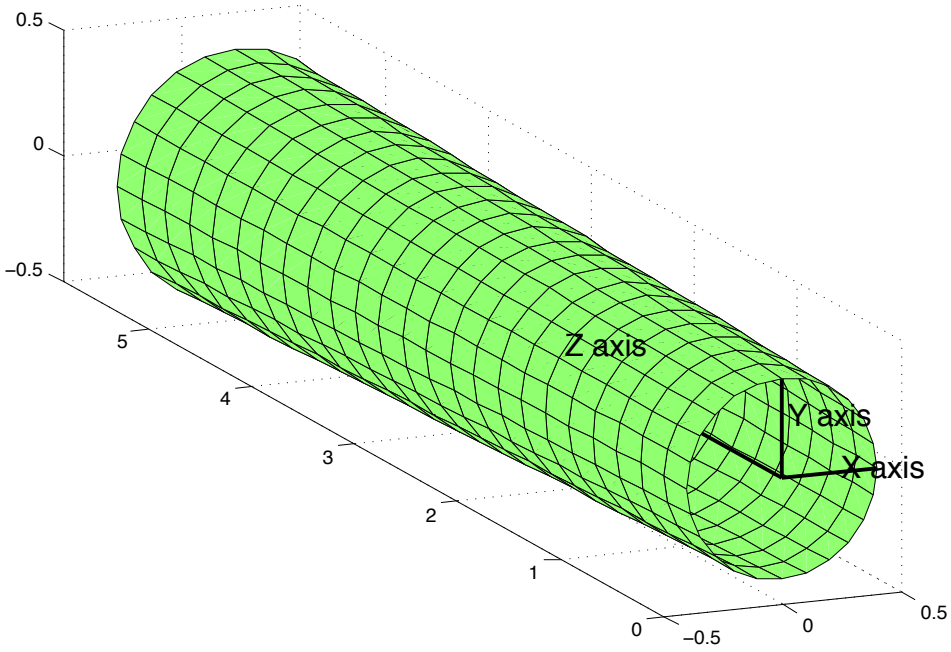

Figure 10.6: 3D fuselage model

The fuselage/beam is assumed to be clamped at its centre of gravity which is indicated by the rectangular grey blocks in Fig. 10.5, note that the c.g. location is taken from the class II weight estimations and thus not simply in the middle of the beam model. The lift forces from the canard and the wing are then multiplied by the moment arm to obtain a moment that increases linearly towards the c.g. of the fuselage.

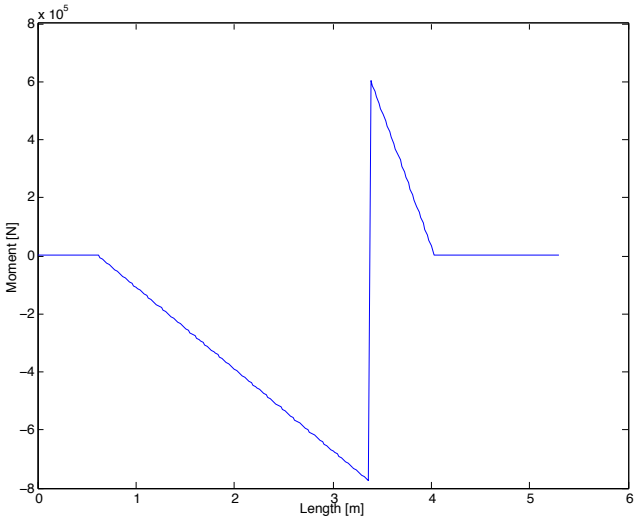

Figure 10.7: Moment over length due to lift of canard and wing

The moments in Fig. 10.7 need to be verified by hand to ensure that the correct moments (both magnitude and sign) are computed by the code. Once this verification is completed the stresses at select points are also verified using the

same equation as applied in the code:

$$\sigma_z = \frac{M_x y}{I_{xx}} \tag{10.16}$$

Where the moment of inertia computation is greatly simplified given the circular cross section:

$$I_{xx} = I_{yy} = \pi r^3 t \tag{10.17}$$

In addition to the moments due to the lift, a direct stress is applied as a result of the thrust generated by the engine and propeller. This is modelled as a direct stress and is super positioned on to the σ_z already obtained due to the lift bending moments. However given that this load is compressive, a buckling check has to be conducted in order to determine appropriate skin thickness. This is done by applying the following relation:

$$t_{buckling} = \frac{4FL^2}{\pi^3 E r^3} \tag{10.18}$$

Once the thickness of the fuselage skin has been determined, enough information is available to obtain the direct stress. This is done using the equation below :

$$\sigma_z = \frac{F}{A} \tag{10.19}$$

Note that the F denotes the thrust whereas A is the cross sectional area of the fuselage which is computed using:

$$A = \pi(r^2 - (r-t)^2) \tag{10.20}$$

Where r denotes the radius and t is the thickness determined due to Eq. (10.18)

The fuselage also experiences a torque which results from aileron deflection as discussed in subsection 10.1.1 and is incorporated as shear stress into the fuselage cross section. This torque is constant and therefore the shear stress only varies due to the change in area (as a result of fuselage taper).

The resulting shear flow is computed using Eq. (10.21), subsequently the shear stress is obtained by dividing the shear flow by the thickness of the skin as shown in Eq. (10.22):

$$q = \frac{T}{2Ar} \tag{10.21}$$

Note that Ar is the enclosed area and not the cross sectional area as used for the direct stress computation.

$$\tau = \frac{q}{t} \tag{10.22}$$

Finally, as a result of clamping the wingbox into the fuselage, a wing bending moment is present along the chord length of the wingbox. This results in a bending stress about the longitudinal or z-axis of the fuselage (as opposed to the bending stress about the lateral or x-axis). In case the axes referred to are not immediately clear the reader is referred to Fig. 10.6.

The equation applied in order to determine the stresses due to the clamped bending moment is almost identical to Eq. (10.16) where only subscripts have been changed:

$$\sigma_x = \frac{M_z y}{I_{zz}} \tag{10.23}$$

Due to the combined shear, bending and direct stresses a Von Mises stress analysis is used in order to find the points that have the most critical stress. It is important to note that the structure used in the fuselage is a truss structure and therefore the circular cross section shape should not be confused with a monocoque structure. It is merely used to represent the geometry and points of highest stress. It aids in, for example, sizing of a particular truss at a certain point. The equation used is Eq. (10.15).

10.3.1 Fuselage structure

In the mid-term report a trade-off was performed for the fuselage structure and the result of this was a semi-monocoque structure. This structure was chosen mainly because of its beneficial loading paths for complex structures. Since the current design does not have a complex structure and the advantages of the semi-monocoque at this this stage do not overcome the disadvantages, for example the difficult accessibility for maintenance, a truss structure is chosen.

A truss structure consists of a box frame made up of four longerons, running the length of the fuselage [38]. It is connected with vertical and horizontal members so as to form four trusses. At this stage it is important to reiterate that the truss structure was sized under the assumption that only moments were taken up by the trusses (whereas the skin was effective under shear).

This has to be done by dividing the entire length of the fuselage up into five parts: forward, canard box, centre, wingbox and the aft section, illustrated in Fig. 10.8. The length of the entire fuselage structure (L_{f_s}) is taken as a percentage of the entire fuselage length (as given by the control and stability department), to fit within the shape that is determined in section 8.3. This also holds for the height as well as the width of the fuselage structure, h_{f_s} and w_{f_s} respectively. The length of the centre section is taken from the control and stability department, it equals the length of the canards' arm to the leading edge of the MAC of the main wing. The wingbox and canard box sizes are determined in section 10.1.

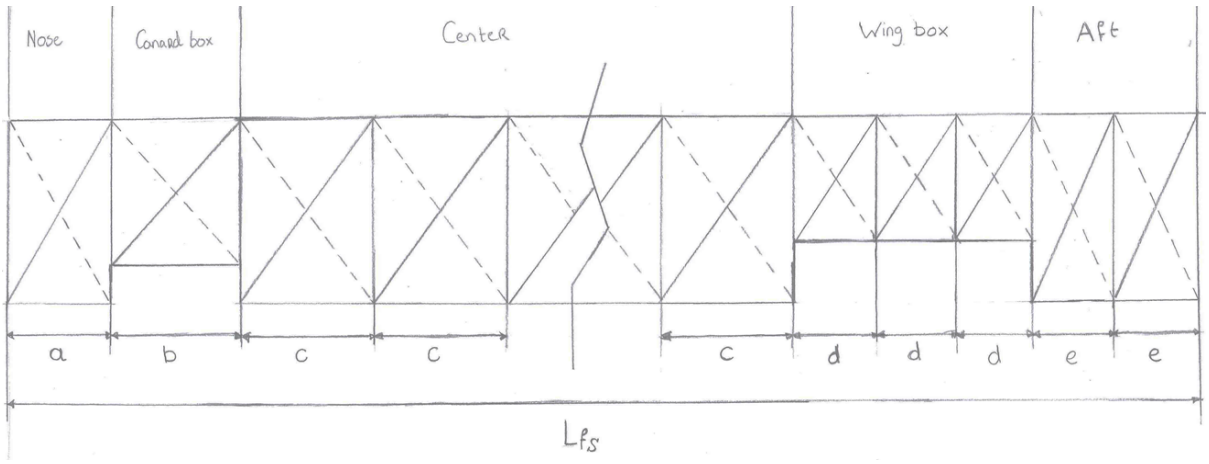

Figure 10.8: Drawing of the preliminary truss structure with the five parts indicated on the top

As can be seen in Fig. 10.8, the five parts have vertical rods that separates the parts in different sections. The width of each section within a part is constant. This can be seen in the figure with the indicated sections with a width 'a' up till 'e'. Within these five parts the number of sections is kept variable until the final dimensions are known.

Another parameter that has to be kept variable is the diameter of the rods. These rods are split up into three categories: horizontal, vertical and diagonal. The diameter of these rods can change with fuselage section and orientation. The final diameter of the rods will be based on the stresses that are present at the wingbox interaction as was explained in section 10.1.

In subsection 7.1.3 it was stated that the performance department will need the mass moment of inertia (MMOI) around the y-axis. After the preliminary variable lay-out of the truss structure is determined, the MMOI can be calculated. The I_{yy} is calculated using Eq. (10.24) which is simplified using the thin walled assumption to Eq. (10.25)[39].

$$I_{yy} = \int (x^2 + z^2) dm + m\,\mathrm{d}^2 \tag{10.24}$$

$$I_{yy} = \frac{1}{12} m l^2 + m\,\mathrm{d}^2 \tag{10.25}$$

The d in these equation represents the distance from each rods' center of gravity to the center of gravity of the entire aircraft.

Before this equation can be used, the masses of the different rods have to be calculated. This is done by first deciding on what material is used for the fuselage structure. In the RBAR case, the material chosen was in the mid-term report to be AISI Steel 4130 with a density of 7850 kg/m^3. It was selected because of its yield strength is higher than the ultimate tensile stress that will be present during its mission. This decision is supported by the fact that the sustainability of a steel truss structure is substantially higher than the sustainability of a composite structure.

After the masses of all the rods are calculated, the moment of inertia of each rod has to be determined using the first term of Eq. (10.24) (using thin walled assumption). The MMOI calculation for the truss structure is finalised by adding the Steiner terms for each rod (second term of the equation).

After the I_{yy} for the truss structure is calculated, only the canard, main wing and engine have to be added to get the I_{yy} for the entire aircraft. The method for both the canard and wing is exactly the same as for the truss structure, except that the wing has a more complex shape. In order to solve this, both the canard and wing have to be simplified to a solid rectangular shape. The size of these boxes was assumed to have the average area of the entire cross section of the wingbox. The width of the rectangle kept equal to the width of the canardbox or wingbox. The mass of the wing and canard was determined using the method stated in section 10.1 and can again be used in Eq. (10.24).

Finally, the mass moment of inertia of the engine has to be added. The inertia of the engine is calculated with the dimensions and the mass of the engine supplied by the manufacturer. The dimensions are shown in subsection 8.3.2 and the mass of the engine is known from [27]. The influence of the engine on the MMOI is significant, as its weight, including the propeller, is almost 1/3 of the MTOW.

Adding up all the MMOI of the different elements will result in the MMOI of the entire aircraft, I_{yy}

Since the mass of all the rods are calculated, the mass of the entire structure of the aircraft can be easily calculated and will be an output of this analysis(m_{truss}). This truss structure mass can then be compared with the structure weight as calculated in chapter 9.

10.4 Material selection

With stress analysis, sizing and structure of the wingbox (canard and main wing) and fuselage outlined the material choice is of significant influence on the final parameters of the structural analysis. The goal of the structural design is to develop the lightest possible structure able to withstand the loads encountered during its mission profile and those imposed by regulations. Therefore, the design of the aircraft structure is strongly influenced by the material selection. This section lists various aerospace materials and their respective characteristics asides from analysing which materials are most suitable for the selection.

Now that the dimensions, weights, and internal stresses within the main components of the Avinya aircraft are known, materials and structure sizes can be decided upon. By the use of CES Edupack 2013 [40], Table C.1 is generated, as can be seen in appendix C. The program provides a comprehensive database of materials and process information (used as well in chapter 13), and powerful materials software tools. Since CES gives a range of values for each material characteristic, to make the comparison realistic the average value was computed in Table C.1.

The main material selection criteria are:

- High specific strengths and moduli
- (Quasi-)isentropic, if loading is not uni-directional
- Anisotropic, if loading is highly directional and parallel to direction of ultimate strength
- High impact strenght, since safety is considered of importance
- Manufacturability, elaborated upon in chapter 13
- Sustainability, elaborated upon in chapter 17
- Cost, elaborated upon in chapter 4

The materials in Table C.1 are representative of materials used in aerospace applications. During detailed design the best alloy for metals and best ply, fibre/resin ratio, and weave for composites can be determined. But for the conceptual design of Avinya some favourable material characteristics, such as (quasi-)isotropic characteristics or impact strength can already guide the material choice with respect to its specific purpose.

10.5 Verification and validation

The structural analysis of the Avinya concept requires the use of MATLAB based code. However it is necessary that the code be verified and validated in order to ensure that the results are consistent with the real situations i.e. experimental results and the theory that is applied which includes certain assumptions. The section is structured such that the wingbox analysis is discussed first, followed by the fuselage stress analysis and finally the truss structure sizing.

Development of the wingbox stress analysis tool was based upon a MATLAB model as generated at the Delft University of Technology [41]. This tool has been adapted in order to take into account the vertical stabiliser and aileron. Therefore much of the tool has already been verified and validated using experimental data from test results on a wing. Similarly, hand verification was conducted on the base code to ensure that bending stresses due to lift and weight as well as shear stresses due to torsion are computed correctly.

Due to the addition of the aileron and rudder, these functions in the code also need to be verified. This process involved determining maximum moments and stresses at particular points and comparing it to the values obtained by the code. Section 10.5 below indicates the values for maximum shear forces and moments introduced by the vertical stabiliser and aileron amongst others. As mentioned earlier hand calculation was then used to verify that these forces and moments were correct and its influence was indeed clearly visible with respect to introduced stresses.

Table 10.3: Overview of all forces and moments present at their ultimate load case (due to interaction of rudder and aileron)

Component	Type of load	-	Wing 1	Wing 2
Wing	Shear forces [N]	$S_{x,drag}$	5930.9	5222.1
		$S_{z,lift}$	49027	48418
		$S_{z,weight}$	-8682	-9123
	Bending moments (torques) [Nm]	$M_{x,lift}$	89078	94671
		$M_{y,lift}$	16232	16398
		$M_{x,weight}$	-15869	-17151
		$M_{y,weight}$	-282.8	-209.6
		$M_{z,drag}$	-8400.7	-7711.2
Aileron	Shear forces [N]	$S_{z,aileron}$	10079	10066
	Bending moments (torques) [Nm]	$M_{x,aileron}$	22065	22898
		$M_{y,aileron}$	-5198.0	-4982.4
Rudder	Shear forces [N]	$S_{x,drag}$	5931.9	5222.1
		$S_{y,rudder}$	-4899.5	-4857.9
	Bending moments (torques) [Nm]	$M_{x,rudder}$	2006.7	1989.6
		$M_{y,rudder}$	55.00	52.80
		$M_{z,rudder}$	-3213.9	-2840.6

A simple calculation can be performed to check whether the moment created around the x-axis is in the right order, as shown in Eq. (10.26), where the results are compared with the moments as calculated by the numerical model in section 10.5. The difference is explained by the additional moments due to the presence of the rudder, aileron and wing weight. Concluding, the results are in the right order of magnitude and sign.

$$M_x = \frac{MTOW \cdot n_{max} \cdot g}{2} \cdot y_{MAC} \tag{10.26}$$

A visual representation of the vertical stabiliser and aileron influence on the stresses within the wingbox can be

Table 10.4: Verification of moment around x-axis

	Wing 1	Wing 2
$M_{x,verification}$	82927.85	87105.07
$M_{x,MATLAB}$	97380.35	102407.7

found in Figs. 10.9 and 10.10. In these figures the aileron is now deflected upward, resulting in stress relief and the rudder is deflected inward, opposite to the ultimate load case analysed. Indeed, the predicted stress relief occurs and is in the right order of magnitude.

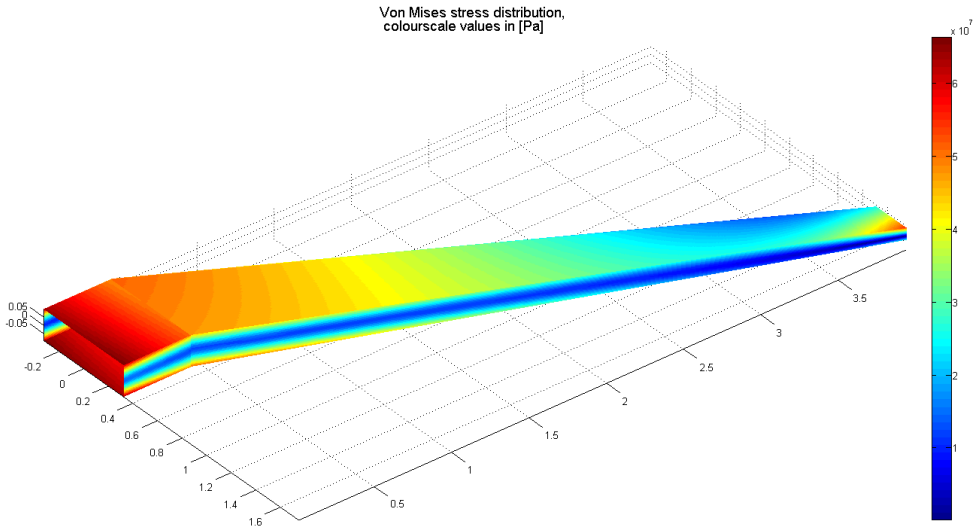

Figure 10.9: Von Mises stress in wingbox of wing 2 with opposite aileron and rudder deflection with respect to the ultimate load case

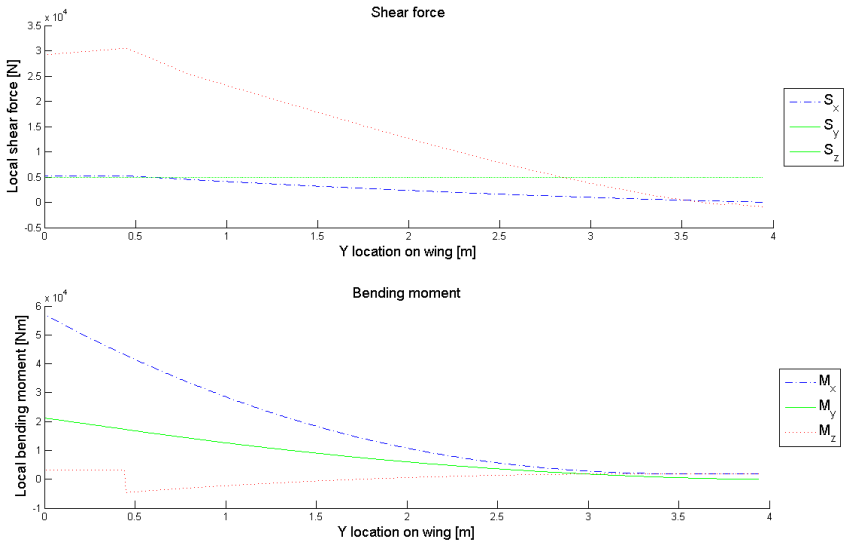

Figure 10.10: Shear forces and moments acting on the wingbox of wing 2 with opposite aileron and rudder deflection with respect to the ultimate load case

Another alteration to the existing program was the sweep angle, which had to be updated from the previous model given the need to use the quarter chord sweep (whereas previous the half chord sweep was used. To provide a quick check if the structural tool made use of the correct sweep angle to calculate the planform parameters (which were determined in the performance analysis) a verification was done, this is shown in Table 10.5. As can be seen these values do not differ significantly with the calculated values, and the small differences can be explained due to the planform parameters that assume a wing continuing into the fuselage under an angle, whereas this is not the case in reality. In fact the box runs perpendicular with respect to the longitudinal axis of the fuselage trough the aircraft.

Table 10.5: Planform geometry parameters

	Wing 1		**Wing 2**	
Dimension	Value from section 7.2	Value from model	Value from section 7.2	Value from model
S_{wing} $[m^2]$	9.230	9.230	9.230	9.239
A	5.835	5.837	6.725	6.721
λ	0.450	0.447	0.352	0.352

The wing introduces shear forces and moments on the fuselage, therefore, the next logical step was to analyse the fuselage structure code. Given the set-up of the code, with all loads applied and the subsequent stresses super positioned meant that hand verification for each separate load case was straightforward. The moment through the fuselage (modelled as a beam) diagram shown earlier Fig. 10.7 was compared to the moment values per length that were computed by hand. These distribution precisely matched the moment diagram produced by the code and thus was deemed verified.

The subsequent step was to determine if the moments were being correctly converted into stresses. Given that the stress analysis is in 3D, only three distinct points along the length and two circumference points at each length point were checked by hand. This was deemed the most efficient manner in which to verify such a complex stress distribution. Once the moments and their stresses were verified, the torsional loads and stresses as well as direct stresses were again checked at three specific cross sectional points along the length. Finally the Von Mises analysis was also verified at these points since all the data was already at hand. This concluded the verification for the fuselage software code. In terms of validation, no test data is available for the fuselage and has therefore been discussed as a future recommendations later in this report. However a sanity check was done by looking at the magnitude of the stresses and the resultant truss structure sizing which was similar to reference aircraft.

Finally, the fuselage truss structure was verified by calculating the mass moment of inertia for a simplified fuselage structure. This fuselage structure contained one section per part(nose, canardbox etc.) and a constant rod diameter throughout the structure. Hand calculations verified the model, it gave the right values for the highly simplified fuselage structure. Therefore it was assumed that the model gave the right outcomes for further complex fuselage structures. Validating the fuselage structure program could not be done using available validation data, since this kind of data was/is simply not available. The only way the program could be validated was by checking the outcome was in the same order of magnitude as the outcome of the primitive XFLR5 analysis. This method ‘validated’ the fuselage structure model.

Chapter 11 - Detailed conceptual design

Now the methods used during the conceptual design phase of Avinya are validated and verified, the results are presented. The structure of the section does not follow the outline of distinct departments as shown in the the methodology but rather takes the reader through the process in terms of the steps taken by the team during the actual design. The process is very iterative and a number of iterations are conducted to ensure realistic results, for example that a suitable lift coefficient is generated by the airfoil whilst maintaining longitudinal static stability of the aircraft.

Since all iterations follow the same process and methodology, whereby only the input values and resulting output values change, only one iteration, namely from the penultimate point to the final values, is shown here. This iteration is the final of three major iterations that took place in order to realise the final aircraft parameters. It should be stressed however that within the three large iterations, multiple small iterations took place between certain steps, these are highlighted during the forthcoming section where relevant. The penultimate values are those at the start of section 11.1; these values are applied as described in the various methodology sections in order to arrive at the final point. The reader will qualitatively be taken through the steps and processes used to arrive at the final values with the aid of figures and graphs where possible. Additionally the structure is analysed for stresses and load bearing components such as truss structures and wingboxes are sized. A race simulation is also conducted on multiple tracks in which the concept times are obtained. The section concludes with 2D technical drawings and a 3D render as well as tabulated geometry and performance characterstics that define the concept.

11.1 Iteration walk-through

The large number of values used in the final iteration step necessitate the use of a tabular form in order to present and display all parameters. Table 11.1 shows all the component weights and c.g. locations of the aircraft and Table 11.2 presents an overview of all the parameters, both at the penultimate design point. At the end of this section the same tables are presented with updated values so the reader can compare both values and see the effect of the iteration.

Table 11.1: Component weights for the penultimate design point

	Wing 1		Wing 2	
Component	**Weight [kg]**	**c.g. [m]**	**Weight [kg]**	**c.g. [m]**
Canard	44	0.68	44	0.68
Fuselage	77	2.44	77	2.44
Engine	225	4.8	225	4.8
Fuel system	11	3.65	11	3.65
Flight controls	47	2.88	48	2.88
Electrical & instrumentation	15	1.8	15	1.8
Wing	105	4.22	112	4.22
Landing gear	18	3.59	18	3.59
Vertical tail	12	4.82	12	4.31
OEW	555	3.72	562	3.72
MTOW	703	3.37	710	3.38

Table 11.2: Parameters for the penultimate design point

Parameter	Wing 1	Wing 2	Unit
Aerodynamics			
$C_{L_{max}}$	1.52	1.54	-
C_{D_0}	0.0254	0.0263	-
C_{L_α} (wing)	0.0691	0.0704	1/°
$C_{m_{ac}}$ (wing)	-0.038	-0.041	-
C_{L_0} (wing)	0.149	0.150	-
C_{L_α} (canard)	0.0726	0.0726	1/°
C_{L_w} (landing)	0.88	0.89	-
C_{L_c} (landing)	1.3	1.31	-
ΔC_{L_c}	0.35	0.36	-
$\alpha_{landing}$	12	12	°
δ_e	10	10	°
Wing			
S	8.6	8.6	m^2
b	7.21	7.8	m
c_r	1.65	1.65	m
c_t	0.740	0.545	m
A	6.05	7.08	-
λ	0.45	0.33	-
$\Lambda_{1/4}$	25	25	°
x_{LEMAC}	3.71	3.71	m

Parameter	Wing 1	Wing 2	Unit
Canard			
S_c	1.376		m^2
b_c	3.1		m
c_{r_c}	0.44		m
c_{t_c}	0.44		m
A_c	6.98		-
λ_c	1		-
Λ_c	0		°
Landing gear			
x_{ng}	1.62		m
x_{mg}	4.085		m
h_{lg}	1.38		m
w_{lg}	2.3		m
Vertical tail			
S_v	0.73	0.7	m^2
b_v	0.9	0.7	m
c_{r_v}	1.05	1.05	m
c_{t_v}	0.515	0.515	m
λ_v	0.49	0.49	-
Stick force			
F_e	136.3	143.6	N

In Table 11.1 the values are given for wing 1 and wing 2. These two wings signify the different wing planform geometries and shapes that were determined to comply with the requirement of aircraft customisability. Specifically wing 1 was optimised for the roll rate whereas wing 2 was optimised for rate of climb and aerodynamic efficiency.

Upon arriving at these design specifications, it was decided that there was room to improve the performance such as stall speed, landing distance and rate of climb of the aircraft by obtaining a higher $C_{L_{max}}$. In order to produce this change in $C_{L_{max}}$ the design team can either:

- Select a different airfoil
- Modify the wing geometry

In earlier iteration steps the airfoil was changed when a (significantly) higher value for $C_{L_{max}}$ was needed. Given that that the final iteration was being conducted, in which the desired increment of change was small, the wing geometry was changed in order to achieve an increase in $C_{L_{max}}$ and the airfoil kept constant.

The starting point for the wing geometry, as described in section 7.2, was the wing vs. power loading diagram (see Fig. 11.1), from which a new design point was chosen. This design point was used together with the $MTOW$ to generate a new surface area and aspect ratio required to achieve the performance characteristics. The surface area that was used here was that of the wing and canard combined due to the fact that a canard provides useful lift during flight. The value of the canard area from the previous iteration was subtracted from this value to determine wing specific geometry in order to proceed with the design.

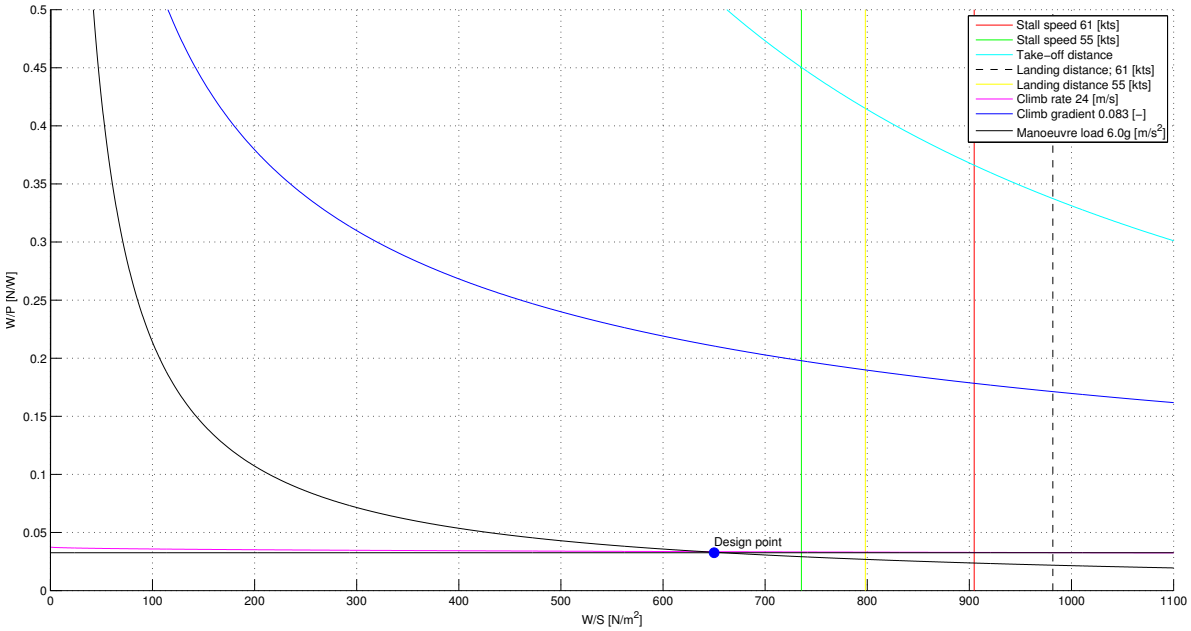

Figure 11.1: Wing loading versus power loading diagram for choosing the design point

Having determined the design point based on the graphs in Fig. 11.1 the wing geometry itself was altered in order to achieve the desired $C_{L_{max}}$. The chosen geometry was not only driven by the $C_{L_{max}}$ value targeted but also performance requirements such as roll rate and climb rate. Furthermore the aerodynamic efficiency of the wing, which was not an explicit requirement, was factored in. This was based on results from the sensitivity analysis found in chapter 6 where higher aerodynamic efficiency provided a significant time benefit. With this in mind the taper ratio for wing 1 was fixed at 0.45, closely approximating the elliptical distribution and therefore giving the highest oswald factor and reduction of induced drag. The root and tip chord were geometrically constrained due to the fixed taper ratio updated surface area and span.

In contrast wing 2 had a fixed root chord, due to the fact that the wing needs to be mounted on the same aircraft for the same structural design. Given the need to increase the aspect ratio with a fixed surface area resulted in the taper ratio as the variable for this wing planform. As a result the tip chord of wing 2 differs from to that of wing 1. A visual representation is given in Fig. 11.2.

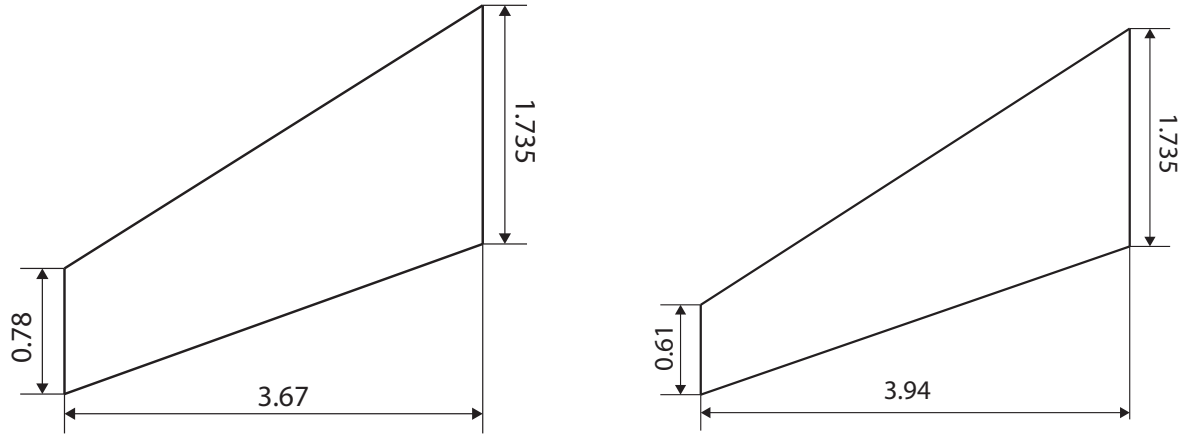

(a) Wing 1 **(b) Wing 2**

Figure 11.2: Sketch of wing 1 and wing 2, not to scale

For the 3D wing analysis the new planforms were input into XFLR5 and plots were generated to check characteristics such as lift distributions, $C_{L_{max}}$, and C_{D_0} values. Should the characteristics be unsuitable or insufficient the planform was updated again, thus this is a crucial step in the iteration. The results of the aerodynamics section can be summarised in the polar graphs shown in Fig. 11.3. The graphs are obtained by modelling the wing and canard together in XFLR5. This has been done for both wing configurations - optimised for roll and climb i.e. wing 1 and 2 respectively.

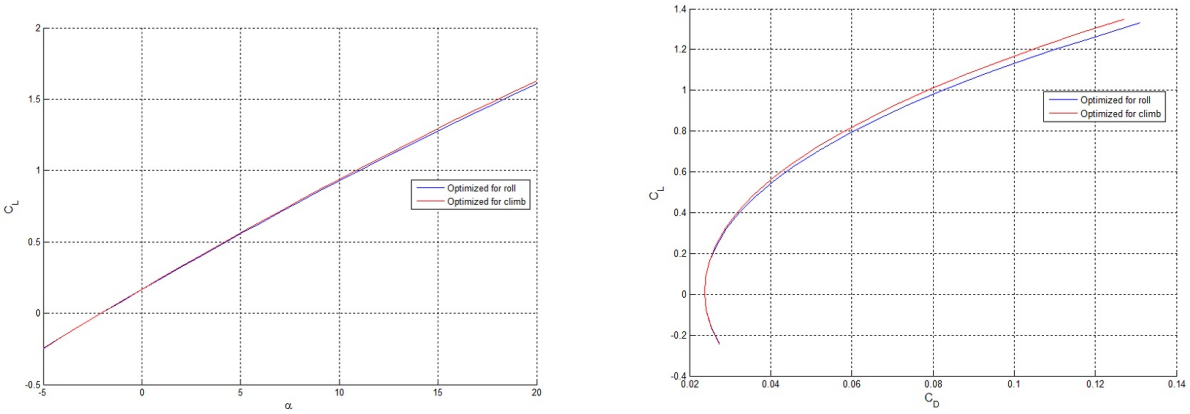

(a) C_L-α **(b)** C_L-C_D

Figure 11.3: Polar graphs showing aerodynamic performance

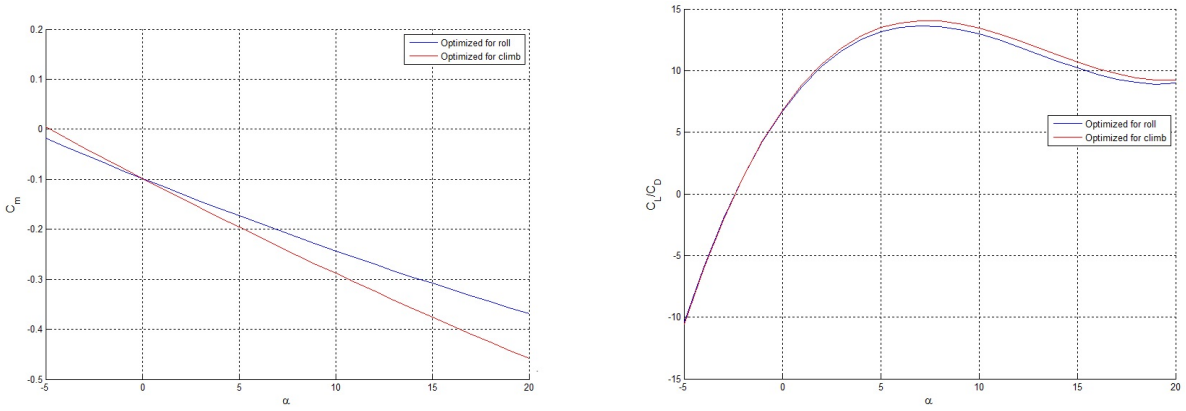

(c) C_m-α **(d)** C_L/C_D-α

Figure 11.3: Polar graphs showing aerodynamic performance

Figure 11.3a shows change of lift coefficient values with varying angles of attack. Due to the limitations of XFLR5, the exact stall angle cannot be determined for the 3D wing. The stall prediction from XFOIL for the 2D airfoil is 21° for NACA 2414. Keeping a safety margin of 5%, stall for the wing has been estimated to be at 20°. With these assumptions, the value of $C_{L_{max}}$ for the final design as seen in Fig. 11.3a is 1.6 which is an increase of 6.67% from the value that had been considered at the start point. The lift slope for wing 2 is higher than that of wing 1 as expected. This is mainly due to the use of longer span and thus higher aspect ratio for the former configuration.

The drag polar for both wing configurations can be seen in Fig. 11.3b. For the configuration optimised for climb, C_{D_0} is 0.0237 which is almost the same compared to wing 1(difference of 0.42%). Both wings have the same surface area and sweep, and hence the profile drag is similar. However, for the climb optimised configuration the aspect ratio is higher and hence induced drag is lower. This is reflected in the graph as a lower drag curve.

Figure 11.4c illustrates the change in C_m with respect to angle of attack for wing plus canard configuration. The pitching moment gradient $\frac{dC_m}{d\alpha}$ is negative indicating that the aircraft is stable together with the canard. The $C_m - \alpha$ curve for the entire aircraft, i.e. incorporating the fuselage and propeller contribution to stability, might be different; it can not be analysed with the programs used and thus is left as future recommendation.

The L/D ratio plotted against angle of attack is shown in Fig. 11.4d. The average value of L/D taken in the range of angles of attack for aerobatic manoeuvres (up to 17.5°)[42] is 12.6 for climb optimised configuration and 12.1 for roll optimised configuration. The L/D for $C_{L_{des}}$ value of 0.2 is 7.5 which corresponds to AoA of 1°. The value obtained must be checked more thoroughly since XFLR5 is unable to give the drag polar for the entire aircraft and thus drag calculations were performed analytically as discussed in section 8.5.

On a further note, pressure and lift distribution for the entire aircraft modelled in XFLR5 after optimizing the flow over the wing and fuselage is shown in Fig. 11.4

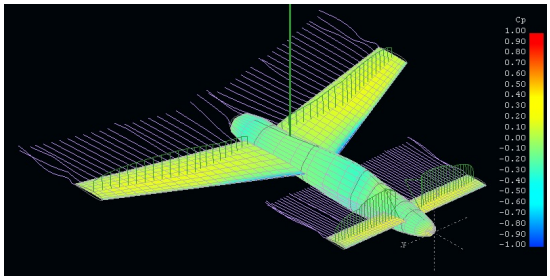

(e) Isometric view

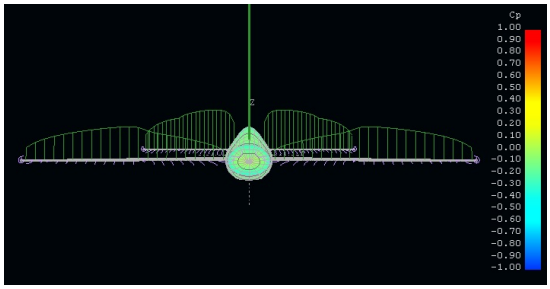

(f) Front view

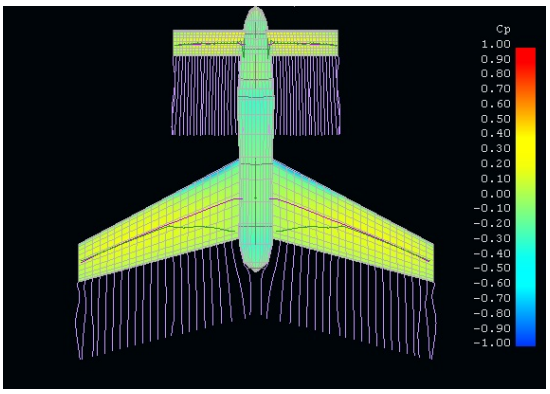

(g) Top view

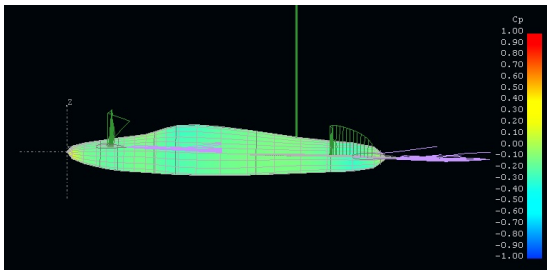

(h) Side view

Figure 11.4: Pressure and lift distribution during cruise flight

Once the wing geometry has been iterated and the 3D analysis indicates that it has the correct characteristics, the class II weight estimation methods could be applied to generate a new OEW and $MTOW$. Furthermore the component weights, primarily that of the wing, were updated along with the overall c.g. position of the whole aircraft. The reader can find the starting component weights in Table 11.1. During the iteration, some component weights along with their c.g. positions changed in order to make the aircraft stable. These new values can be seen in Table 11.14, which shows all the updated component weight along with their c.g. positions for both wing configurations. In addition, the OEW and $MTOW$ have been updated as well.

With the wing planform geometry as well as component weights and subsequent c.g. location updated, the next step was to ensure static longitudinal stability for the concept. It was at this step that the c.g. range, scissor and wing location plots were produced. With the aid of these plots the stability was determined - with the aim of being as close to neutrally stable as possible. At this stage the canard area and geometry were updated based on stability as well as total lift required. Should it be found that the aircraft can not be made stable with its geometry, the loop goes back to the beginning and the $C_{L_{max}}$ and wing geometry need to be updated (along with a new 3D wing analysis).

Figures 11.5 and 11.6 display the matched c.g.-range and scissor plot for wing 1 and wing 2 of the final design respectively. In the generation of these plots the longitudinal wing position was kept fixed, as the two different wings are planned to be used interchangeably without altering the rest of the aircraft. The blue, solid line represents the aft limit of the aircraft's centre of gravity as dictated by the stability criteria. The forward c.g. limit due to the controllability requirement is indicated by the dashed red line. The range over which the c.g. of the aircraft travels during operation has to be between these two limits. For an optimum design the canard should be just large enough to satisfy the stability and contrallability requirement, as a larger than necessary canard is only adding additional weight.

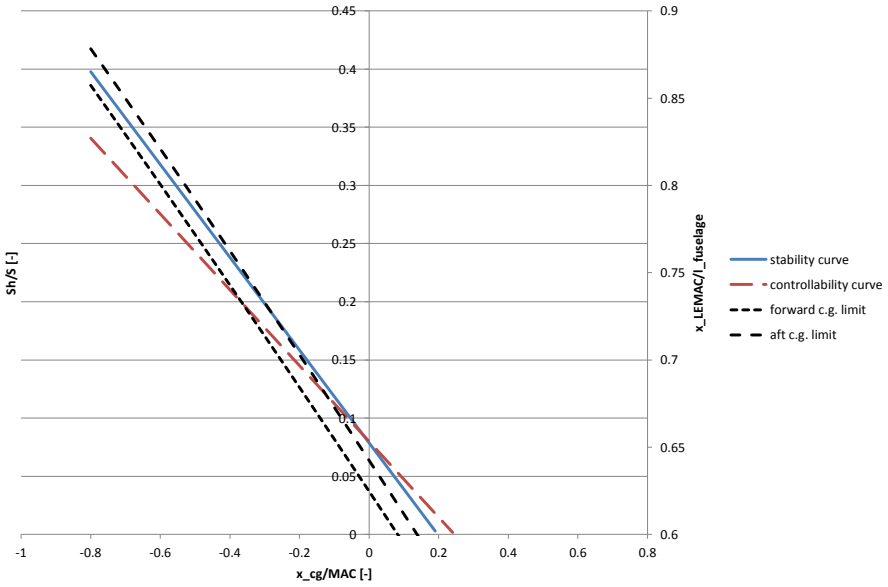

Figure 11.5: Match of c.g.-range and X-plot used in determining the canard surface area and the longitudinal wing position for wing 1.

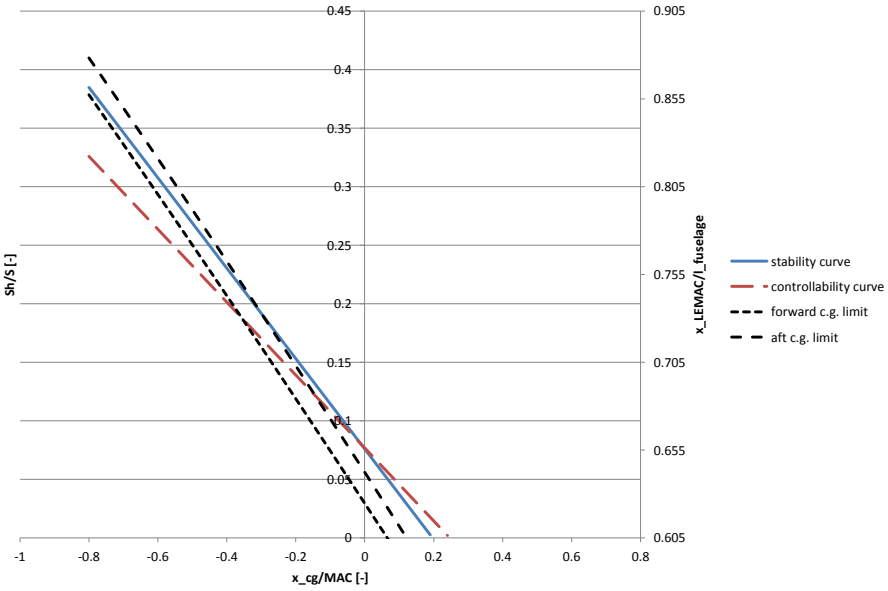

Figure 11.6: Match of c.g.-range and X-plot used in determining the canard surface area and the longitudinal wing position for wing 2.

As seen in Figs. 11.5 and 11.6, the intersection of the c.g.-range and the c.g. limits is at a canard/wing surface area ratio of $S_h/S = 0.195$ and a corresponding longitudinal wing position of $x_{LEMAC}/L_{fuselage} = 0.733$. Furthermore, the two graphs appear to be almost identical with only a small difference in the c.g.-range. This is due to the fact that except for the wing the aircraft is indeed identical, which results in only a small shift in the centre of gravity at OEW. The most important conclusion of the comparison of the two figures is that the two wings can indeed be used interchangeably. The canard surface is sufficient to guarantee both stability and controllability for both wing geometries.

With the result that the aircraft at this stage was deemed stable, the landing gear position and height were determined based on tip over criteria and tail (or prop) strike during take-off rotation. As mentioned in section 9.3, the clearance angle to avoid prop strike is dependent on the angle of attack during landing. The landing angle of attack required is $\alpha_{land} = 11°$. The corresponding clearance angle, the tip over criteria, as well as the resulting landing gear positions, height and track are displayed in Table 11.3.

Table 11.3: Landing gear limitations and final dimensions

Parameter	Value	Unit
Long. tip-over angle ϕ	15	°
Lat. tip-over angle Φ	55	°
Long. ground clearance θ	16	°
Main gear position x_{main}	4.13	m
Nose gear position x_{nose}	1.73	m
Landing gear height h_{lg}	1.34	m
Landing gear track w_{lg}	2.2	m

With the landing gear positioned and sized for stability the iterative process is concluded. The next section outlines the stresses within the structure and subsequent sizing chosen for load bearing components along with the performance analysis of the aircraft on a simulated track.

11.2 Structural sizing and performance analysis

Due to the fact that certain aspects of the results fall outside the iterative process, they are discussed here for clarity. These analyses required input from the the iterative steps however did not output results that immediately affected the iteration. The particular aspects include the stress analysis on wing and fuselage and thus also sizing of the truss and wingbox structures, as well as the performance analysis using the trajectory optimisation tool to determine race times obtained through simulating a race through RBAR circuits.

To begin with, the wingbox structure is analysed using input data from aerodynamics such as lift and drag distribution. With the estimated wing and vertical stabiliser component weight, a weight distribution is generated and can be seen together with the lift distribution in Fig. 11.7.

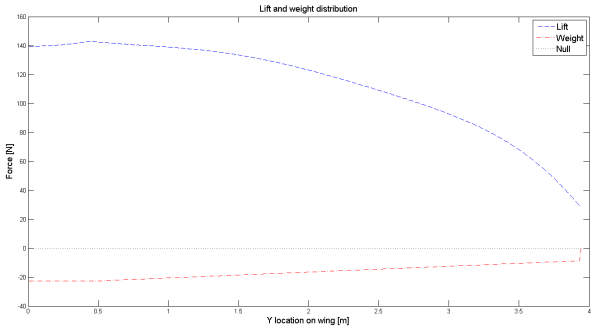

Figure 11.7: Load diagram of lift and wing weight distribution at n = 15

Before proceeding to the final shear forces and moments, a closer look is provided at the rudder and aileron. Both the aileron as the rudder introduce additional moments and shear forces along the wing. In Fig. 11.8 the moment generated by the aileron is shown for wing 1. Both moments, $M_{x,aileron}$ as $M_{y,aileron}$ may act in opposite direction, depending on the deflection of the aileron. For the ultimate load case, this is when deflected downward, generating

a positive force in vertical direction, resulting in a positive $M_{x,aileron}$ and negative $M_{y,aileron}$.

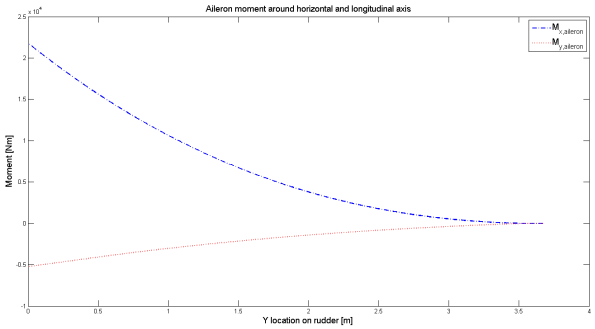

Figure 11.8: Moment induced by maximum rudder deflection around horizontal axis

In addition to the aileron, the rudder must be taken into account as well. For the asymmetric rudder, a resulting moment around the horizontal axis of the wingbox is generated. This moment varies along the rudder height and is shown in Fig. 11.9. If the rudder is deflected outward a positive moment is introduced by the upper part of the rudder, whereas the lower part of the rudder generates an negative moment. The resulting moment $M_{x,rudder}$ is thus positive. The additional moments: $M_{y,rudder}$ and $M_{z,rudder}$ are positive and negative subsequently.

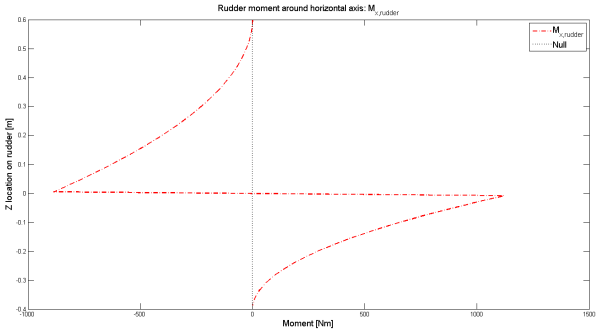

Figure 11.9: Moment induced by maximum rudder deflection around horizontal axis

Having shortly reflected upon the additional shear forces and moments induced by the aileron and rudder, an overview of all shear forces and moments will be provided for both wing planforms in section 10.5. In addition to this table a graph of the shear forces and moments as induced along the wing span is provided for wing 1 Fig. 11.10.

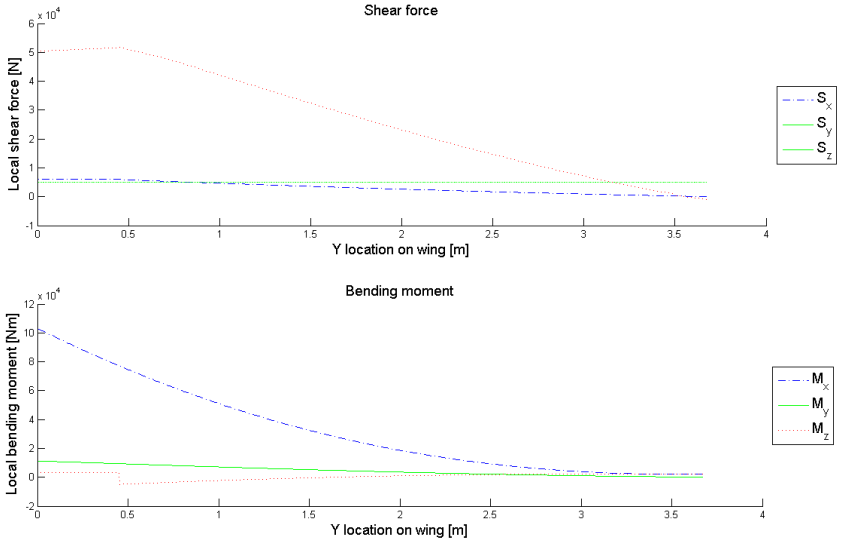

Figure 11.10: Shear forces and moments induced along semi-wingspan of the wingbox of the main wing (1)

With the computation of the shear forces and moments, the Von Mises, shear and normal stresses have been calculated and the maximum stresses are provided in Table 11.4. A stress distribution along the wingbox can be seen in Fig. 11.11. It is apparent that aileron and rudder deflection have a noticeable influence on the overall stresses within the structure.

Table 11.4: Maximum stresses present in wingbox

	Wing 1	**Wing 2**
Dimension	Value	
Y_{max} [MPa]	302.18	302.30
σ_y [MPa]	$\pm$ 246.4	$\pm$ 297.11
τ_{xz} [MPa]	-32.74	-31.874

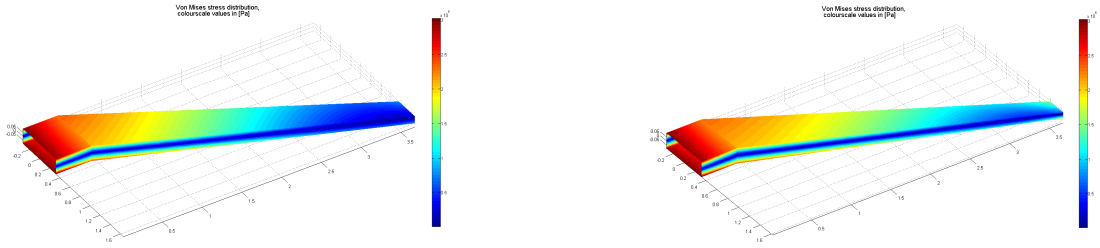

(a) Wing 1 **(b) Wing 2**

Figure 11.11: Von Mises stress in wingbox of wing 1 and 2

The above results have been obtained after multiple internal iterations for which a minimum structural weight had to be achieved. The wingbox geometry has been adapted to meet the ultimate yield stress of the chosen material. Where the material chosen for the wingbox is Epoxy/HS carbon fibre, UD composite, quasi-isotropic laminate, as defined in CES Edupack 2013 [40]. Due to the low density, high specific strength and sufficient impact strength

this material is considered to be the best in terms of specific properties. In addition, the quasi-isotropic composite is capable of handling stresses in multiple directions thus giving it an advantage over bi-axial, woven or singular uni-directional composites. The material characteristics are provided in Table 11.5.

Table 11.5: Material characteristics of epoxy/HS carbon fibre, QI

Characteristic	Value	Unit
Density ρ	1565	kg/m^3
Price	31.1	*e*/kg
Yield strength Y	302.5	MPa
Tensile strength σ_t	302.5	MPa
Compressive strength σ_c	599.5	MPa
Impact strength *Izod*	51.5	kJ/m^3

Adapting the wingbox geometry to meet the material yield stress is a complex process. The resulting geometry as well as shear centre and centroid of the wingbox have been provided in Table 11.6 and Figs. 11.12a and 11.12b. The resulting wingbox weight and material cost are provided in Table 11.7. It must be noted that weight and cost are indicated for a single wingbox, thus for one side of the wing and therefore have to be multiplied by 2 in order to get the weight and cost for the whole wing. The results and discussion with respect to the canard are added in appendix D, for the interested reader.

Table 11.6: Dimensions of the main wing wingbox structure

	Wing 1		Wing 2	
Dimension	At root [mm]	At tip [mm]	At root [mm]	At tip [mm]
t_f	12.0	5.90	14.5	5.60
t_r	6.90	3.40	9.50	3.70
t_t	5.90	2.90	6.20	2.40
t_b	5.90	2.90	6.20	2.40
w_{root}	650.0	315.9	644.2	247.1
h_{root}	192.6	93.60	190.9	73.20
η	-37.4	-18.2	-25.9	-9.90
ξ	0.00	0.00	0.00	0.00
X	-28.3	-13.7	-24.1	-9.20
Z	0.00	0.00	0.00	0.00

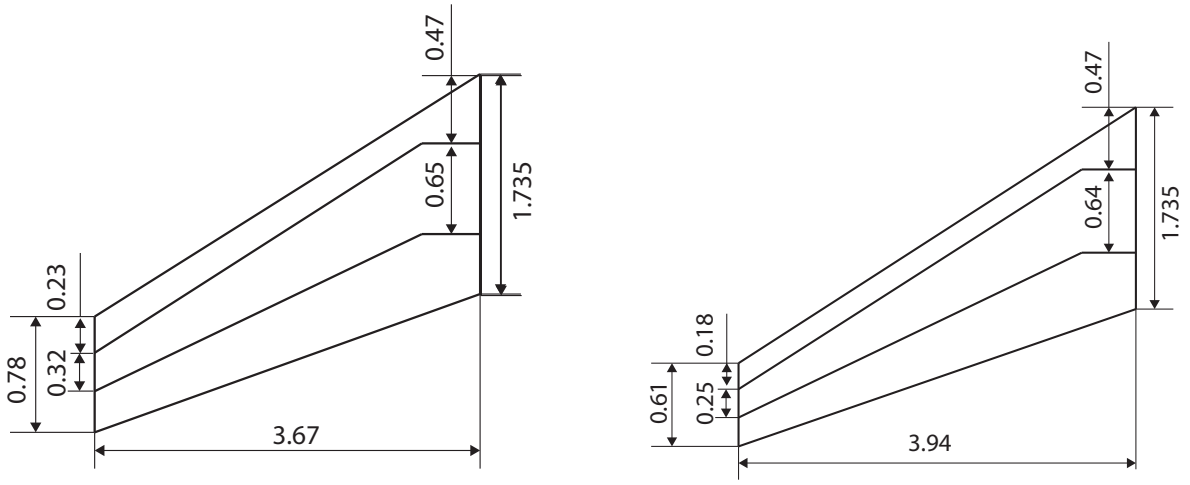

(a) Wing 1 **(b) Wing 2**

Figure 11.12: Sketch of wing 1 and wing 2 including the wingbox, not to scale

Table 11.7: Weight and material cost of the main wingbox structure

Dimension	Wing 1	Wing 2
$W_{wingbox}$ [kg]	41.22	44.375
$Cost_{wingbox}$ [€]	1281.81	1380.08

With the stress analysis for the wing complete and subsequent wingbox sizing and material choices made, the fuselage structure can be analysed. The methodology as described in section 10.3 is applied in order to determine areas with critically high stresses. Due to the multiple load cases applied on the fuselage, each separate loading case will be shown in order to help the reader understand how the eventual Von Mises stress distribution was determined.

First the stresses due to the lift of the canard and wing are shown, the reader should recall the fuselage was modelled as a beam clamped at its c.g. and thus the moments are highest around the c.g. location as can be seen below in Fig. 11.13a and Fig. 11.13b:

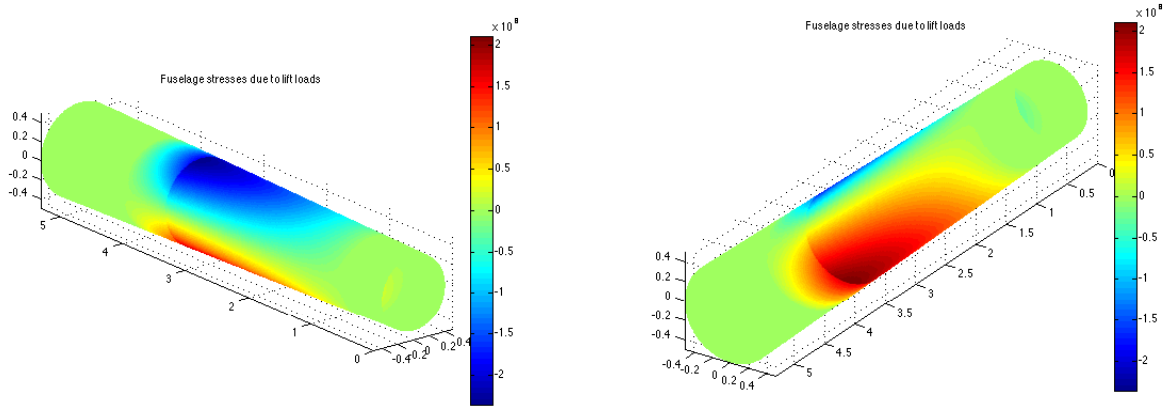

(a) Top view **(b) Bottom view**

Figure 11.13: Stresses due to canard and wing lift moments about c.g. [Pa]

The torsion introduced due to aileron deflection as well as the direct stresses due to the engine thrust introduce stresses into the fuselage as can be seen in Fig. 11.14a and Fig. 11.14b respectively. Note that both forces are constant along the length (z- axis) of the fuselage, however the stresses vary as a result of varying the cross section which is a result of the simplified fuselage shape. This is explained in more detail in section 10.3.

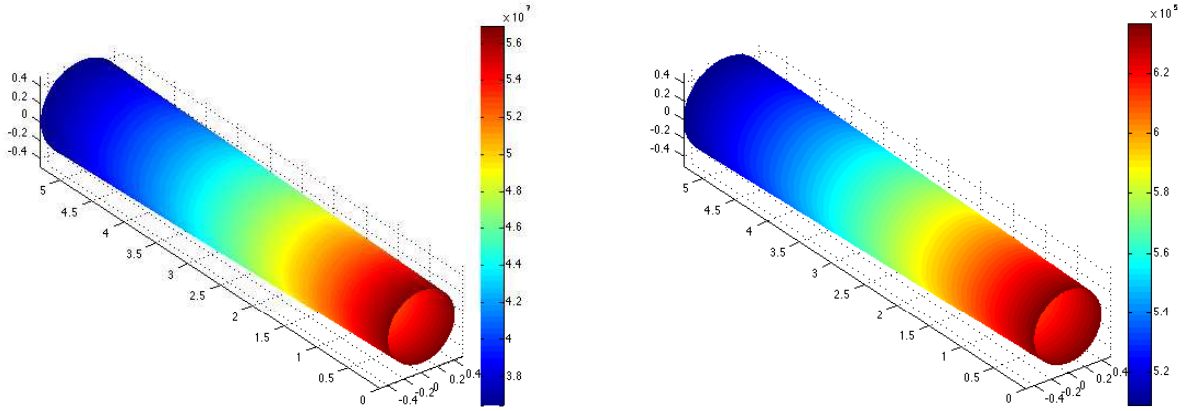

(a) Torsion **(b) Engine thrust**

Figure 11.14: Stresses due to torsion and engine thrust loads in fuselage [Pa]

The final load case to be super positioned is the moment due to the wing and canard being 'clamped' into the fuselage. Once again this moment leads to compressive and tensile stresses and thus a top and bottom view of the fuselage is given.

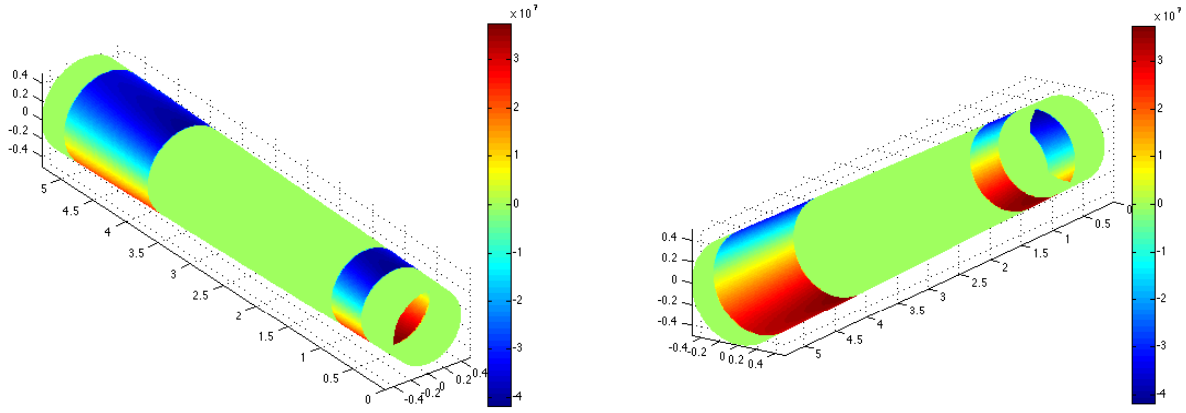

(a) Top view **(b) Bottom view**

Figure 11.15: Stress in fuselage due to clamping wing and canard at root chord

With all the stresses due to individual load cases shown above now known, the Von Mises analysis can be conducted to determine which points have the most critical stresses. The Von Mises results are shown in Fig. 11.16 and Fig. 11.17.

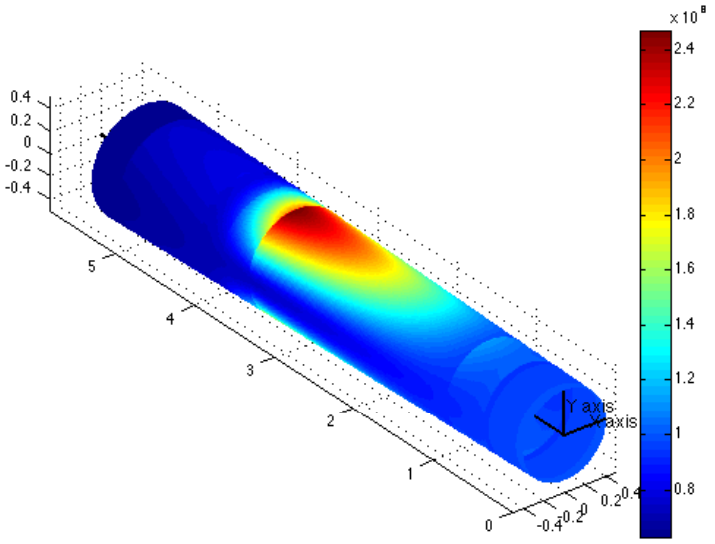

Figure 11.16: Von Mises stress in fuselage, top view [Pa]

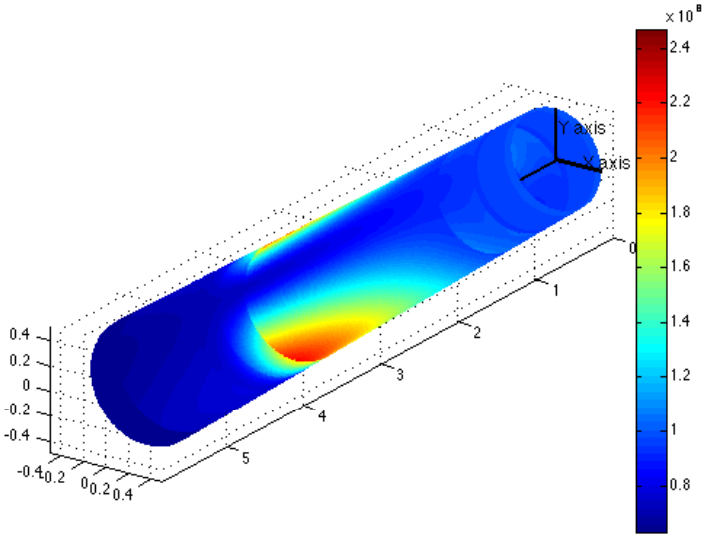

Figure 11.17: Von Mises stress in fuselage, bottom view [Pa]

Clearly the most critical stress occurs at the c.g. location which illustrates that the bending moments about the y-axis of the aircraft due to wing and canard lift are the most crucial. Indeed the stress distribution also indicates that the wing and canard lift moment stresses are higher than the other load cases. This stress analysis is used to size the truss structure, specifically in the section around the c.g. of the fuselage where it is critical to size a structure capable of bearing the loads given that they are highest at this point.

In order to size the truss structure first the fractions of the length, width and height of the fuselage (f_{lf}, f_{wf} and f_{hf} respectively) were estimated in such way that the structure would fit within the skin of the fuselage. These values are presented in Table 11.8.

Table 11.8: Fractions of the fuselage dimensions in which the fuselage structure can be mounted

Variable	Value	Unit
f_{lf}	0.85	-
f_{wf}	0.6	-
f_{hf}	0.6	-

After the fractions were established the main dimensions (which can be seen in Figs. 11.18 and 11.19) of the fuselage truss structure were determined based on the stresses that were obtained from the stress analysis as shown in Fig. 11.16. Specifically it was the buckling loads and direct stresses that primarily influenced the diameter and length of the trusses used. The Von Mises stress was analysed along the length of the fuselage and the truss rods were sized to take the resulting stresses under both tension and compression. The stresses used for the analysis were the most critical stresses found in the particular section that was being sized. The final values are shown in Table 11.9. It must be clear that the bottom view and top view of the fuselage structure also consists of horizontal, vertical and diagonal rods. The values L_{f_s}, h_{f_s} and w_{f_s} resulted from the dimension fractions of the structure.

The value for the average diameter of the rods, D_{rod}, was taken after a stress analysis on the interaction of the wing with the fuselage structure. The Von Mises stress was analysed along the length of the fuselage and the truss rods were sized to take the resulting stresses under both tension and compression i.e. buckling. The stresses used for the analysis were the most critical stresses found at the fuselage wing intersection. The other values were a result of the other departments and are shown in Table 11.9.

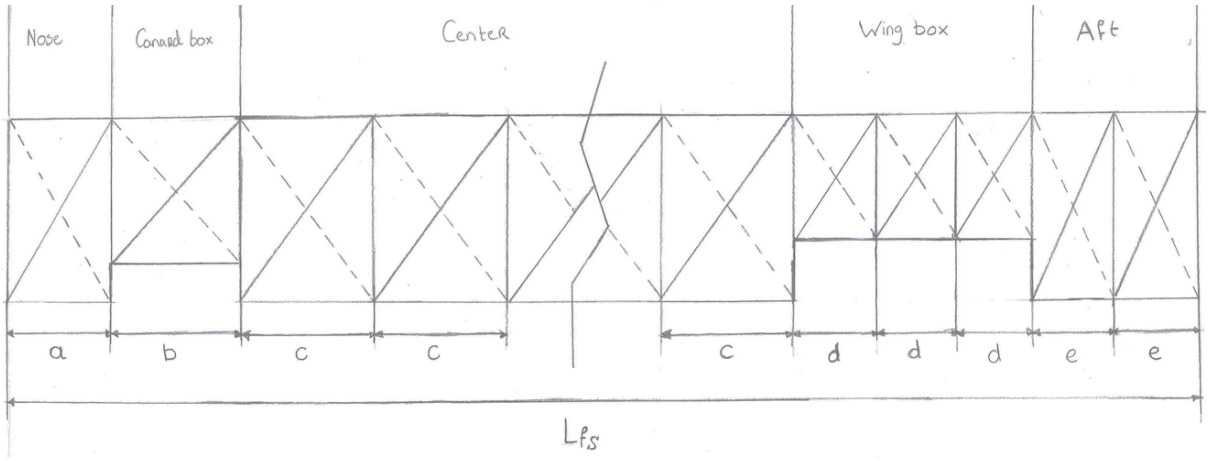

Figure 11.18: Drawing of the preliminary truss structure with the five parts indicated on the top

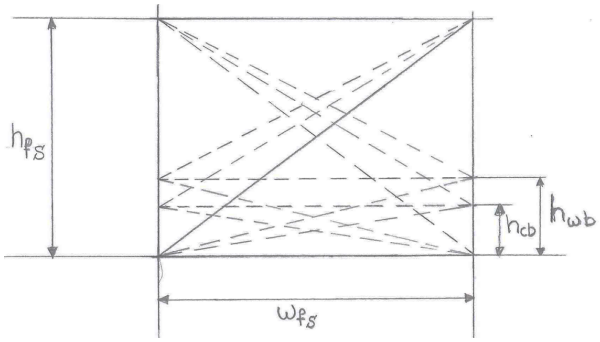

Figure 11.19: Drawing of the preliminary truss structure front view

Table 11.9: Main dimensions of the fuselage truss structure

Dimension	Value [mm]
h_{cb}	90
h_{wb}	196
h_{f_s}	540
w_{f_s}	600
L_{f_s}	4505
D_{rod}	11

Hereafter, the dimensions of all the different parts and number of sections per part were determined in order to provide enough stiffness for the entire aircraft. The number of section and the values for all the sections for the two wings are shown in Table 11.10.

Table 11.10: Sub dimensions for the aircraft fuselage structure

Part	Length [mm]	#Sections	Sec. width	Value [mm]
Nose	250	1	a	250
Canardbox	265	1	b	133
Center	2761	7	c	394
Wingbox	660	3	d	220
Aft	569	2	e	285

With all the dimensions known the mass moment of inertia (I_{yy}) and the mass of the fuselage structure (m_{struc}) could be determined, which are presented in Table 11.11

Table 11.11: Mass and moment of inertia of the aircraft

Parameter	Wing 1	Wing 2	Unit
I_{yy}	989	981	[kgm^2]
m_{struc}	71.6	71.6	[kg]

Table 11.12: Performance characteristics of the aircraft

Parameter	Wing 1	Wing 2	Unit
Rate of climb	24.7	25	m/s
Roll rate	420	398	°/s
Pitch rate	93.8	94.2	°/s

This table shows that the mass of the structure (71.6 kg) was lower than estimated with the class II weight estimation of 77 kg. This difference is present due to the fact that the skin thickness is not added in this fuselage weight but also because of the quite primitive fuselage structure design. This structure is never going to have a rectangular shape. Therefore the weight and mass moment of inertia of the fuselage structure are not the final structural parameters but have to be refined during further development.

At this final stage, using the results of all disciplines gives insight into the feasibility of the performance requirements. It can only be done now, as the computation relies on many input factors such as the wing geometry, fuselage size and the aircraft's internal structure. In Table 11.12, an overview is given for the ROC, roll rate and pitch rate of the aircraft.

With the knowledge of the aerodynamic, structural, stability and performance parameters the concept can be entered into the trajectory optimisation tool and a race simulation can be used to determine how well the concept performs on a simulated track.

As stated earlier due to customisability and modularity demands, two wings have been designed. The significant difference between the wings is that one provides a better rate of climb, whereas the other is optimised for roll rate. To test both, they are subjected to fly both the sample and Abu Dhabi track in the trajectory optimiser. With the Abu Dhabi track being the "tighter" track with gates that are placed closer together. The results are displayed as the times obtained by both wings on both tracks as shown in Table 11.13. For convenience the fastest time per track is highlighted. A promising result is that one of the wings is faster than its counterpart on one track whilst slower on the other track. From this it can be concluded that the customisable wing component is indeed advantageous for competitive air racing.

Table 11.13: Results of two designed wings on two separate tracks

Wing	Track	Total time [sec]
Wing 1	Sample	29.6989
Wing 2	Sample	**29.4795**
Wing 1	Abu Dhabi	**24.1683**
Wing 2	Abu Dhabi	24.4462

For comparison, the airspeed and altitude graphs for both wing configurations on both tracks are shown in Figs. 11.20 and 11.21. The detailed results on all parameters can be found in appendix E.

It can be seen in Figs. 11.20a and 11.20b that wing 2 remains at higher airspeed for the same altitudes from approximately 15s onwards, where a pull-up manoeuvre takes place. The conclusion can be drawn that due to the lower drag, the bleed-off rates are lower.

Flying the Abu Dhabi track, on the other hand, gives a different result as can be seen in Figs. 11.20b and 11.21a. Due to the lower drag of Wing 2, it is faster on the first part of the track (0-10s). However, during the S-turns that follows, it loses due to its lower roll-rate.

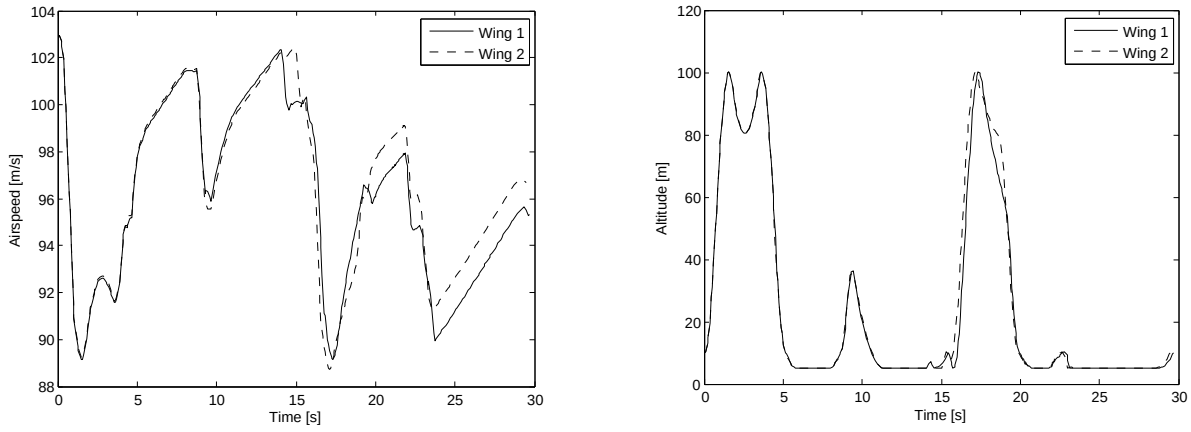

(a) Speed versus time

(b) Altitude versus time

Figure 11.20: Results for wing 1 and wing 2 on the sample track

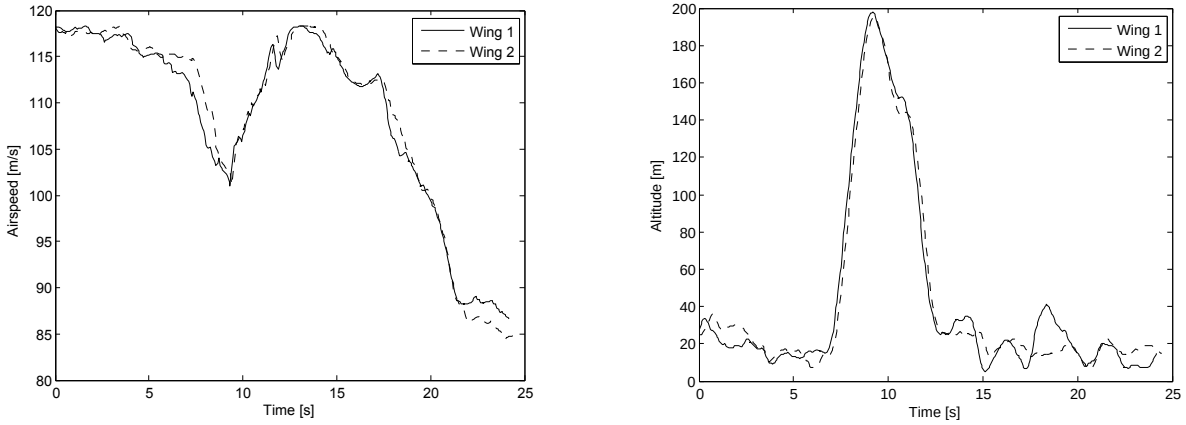

(a) Speed versus time

(b) Altitude versus time

Figure 11.21: Results for wing 1 and wing 2 on the Abu Dhabi track

During the Abu Dhabi race in late February of 2014, the pilots flew one lap in about 28-30 seconds [12] [43]. These times are somewhat slower than what the trajectory optimiser outputs. Likely due to simplifications in the formulas and the fact that it is how a computer controlled aircraft would fly the track, a realistic comparison can be made. However, it does provide a very good method to analyse the performance of both aircraft configurations.

11.3 Concept outline

Having experienced one iteration step in section 11.1, the reader is now taken through the final parameters, sizing and design of the Avinya concept. In Tables 11.14 and 11.15, the final values can be found. It is not certain that a value has changed, nevertheless all values for the same parameters of the starting point are presented. Doing so, both the starting point and the final point of this iterative process.

Table 11.14: Component weight for the final design point

	Wing 1		Wing 2	
Component	**Weight [kg]**	**c.g. [m]**	**Weight [kg]**	**c.g. [m]**
Canard	48	0.71	48	0.71
Fuselage	77	2.44	77	2.44
Engine	225	4.8	225	4.8
Fuel system	11	3.65	11	3.65
Flight controls	48	3.04	48	3.04
Electrical & instrumentation	15	1.8	15	1.8
Wing	106	4.43	112	4.43
Landing gear	18	3.65	18	3.63
Vertical tail	12	5.03	13	5.12
OEW	560	3.77	567	3.78
MTOW	708	3.42	714	3.4.

Table 11.15: Parameters for the final design point

Parameter	Wing 1	Wing 2	Unit
Aerodynamics			
$C_{L_{max}}$	1.54	1.56	-
C_{D_0}	0.0239	0.0240	-
C_{L_α} (wing)	0.0686	0.0699	1/°
$C_{m_{ac}}$ (wing)	-0.037	-0.038	-
C_{L_0} (wing)	0.148	0.151	-
C_{L_α} (canard)	0.0739	0.0739	1/°
C_{L_w} (landing)	0.88	0.89	-
C_{L_c} (landing)	1.29	1.30	-
ΔC_{L_c}	0.30	0.31	-
$\alpha_{landing}$	11	11	°
δ_e	10	10	°
Wing			
S	9.23	9.23	m^2
b	7.34	7.88	m
c_r	1.735	1.735	m
c_t	0.78	0.61	m
A	5.835	6.725	-
λ	0.450	0.356	-
$\Lambda_{1/4}$	25	25	°
x_{LEMAC}	3.885	3.913	m

Parameter	Wing 1	Wing 2	Unit
Canard			
S_c	1.800		m^2
b_c	3.4		m
c_{r_c}	0.529		m
c_{t_c}	0.529		m
A_c	6.42		-
λ_c	1		-
Λ_c	0		°
Landing gear			
x_{ng}	1.73		m
x_{mg}	4.13		m
h_{lg}	1.34		m
w_{lg}	2.2		m
Vertical tail			
S_v	0.80	0.77	m^2
b_v	1.0	1.0	m
c_{r_v}	1.08	1.05	m
c_{t_v}	0.55	0.52	m
λ_v	0.51	0.49	-
Stick force			
F_e	264.5	252.3	N

Using all the parameters that were the outcome of the final iteration, a CATIA model has been produced. Figure 11.22 shows the 3D view from both the front and back of the aircraft. A technical drawing of this model is shown in Fig. 11.23, which presents the front, top and left side view. In addition, the drawing indicates all major dimensions for one configuration.

(a) Front view

(b) Back view

Figure 11.22: Front and back view renders of the final aircraft design

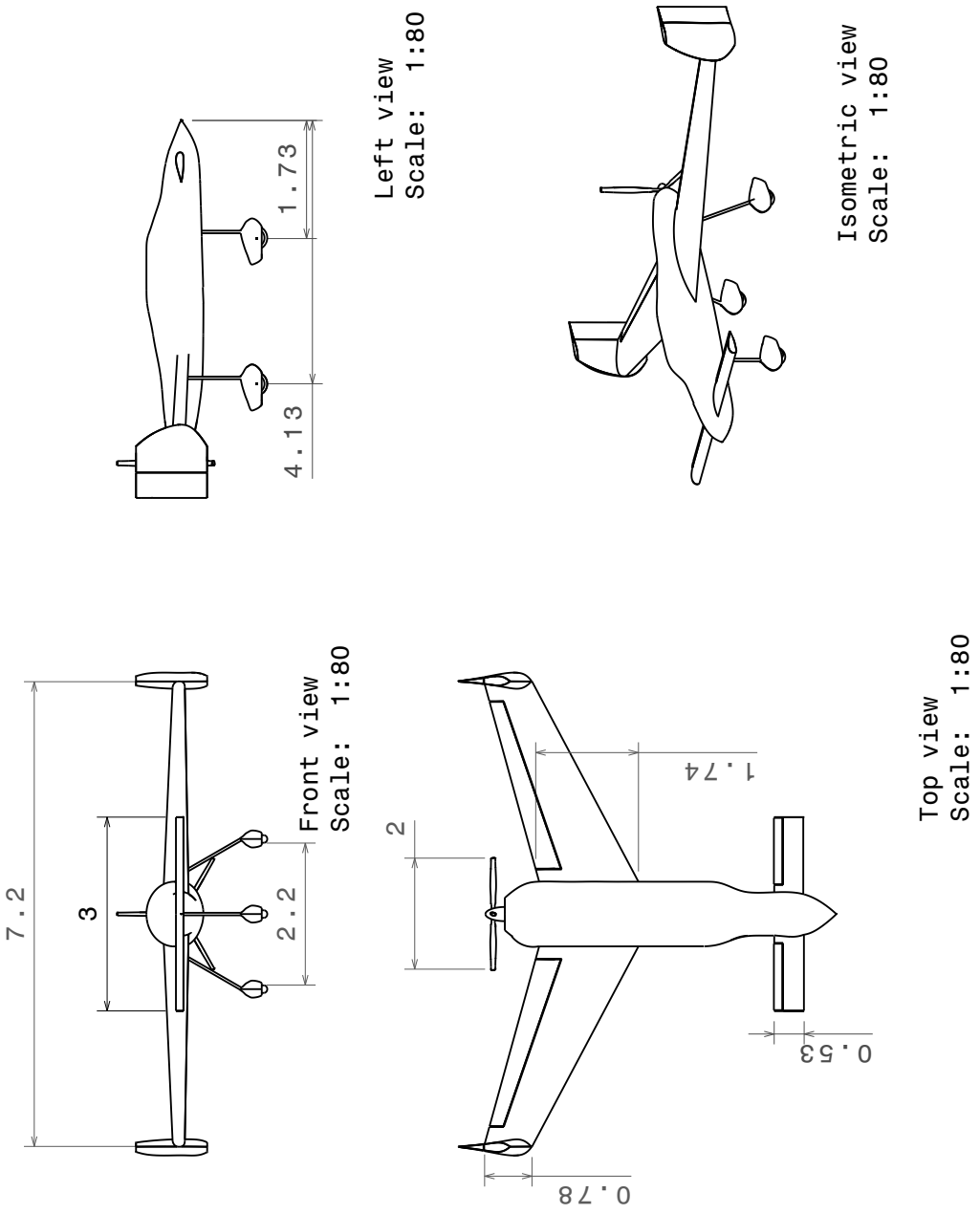

Figure 11.23: Technical drawing of final aircraft design

Part III

Future development

Chapter 12 - Requirement and feasibility analysis

Now that the conceptual design is set it is necessary to judge whether or not the design complies with all requirements and constraints set at the beginning of the project. If a parameter does not comply, the feasibility analysis (section 12.2) elaborates on the need and what steps need to be taken to fix this.

12.1 Requirement compliance

In Table 12.1 an overview that combines both the client requirements and Red Bull regulations is given for each of the wings of the aircraft. Herein the requirement value and whether is complies or not is given.

Table 12.1: Requirement compliance matrix

Requirement	Value	Wing 1	Wing 2
Maximum speed	$>$ 230kts	✓	✓
Maximum rate of climb	$>$ 4700 ft/min	✓	✓
Maximum roll rate	$>$ 420°/s	✓	×
Maximum load factor	$\pm$10g	✓	✓
Empty mass	$<$ 700kg	✓	✓
Empty mass	$>$ 540kg	✓	✓
Race mass	$>$ 698kg	✓	✓
Stall speed	$<$ 61 kts	✓	✓
Take-off distance	$<$ 500m	✓	✓
Landing distance	$<$ 500m	✓	✓
Wing span	$7-8.5$m	✓	✓

There are two requirements on the empty mass. The first is given by the client to compete with the other aircraft, the second originates from the regulations to keep the aircraft safe. As can be seen, only wing 2 does not comply with all requirements. The maximum roll rate for wing 2 is 398°/s and thus lower than the required 420°/s.

12.2 Feasibility analysis

From Table 12.1, it can be seen that wing 1 complies with every constraint, whilst wing 2 does not, due to its lower roll rate. However, as found in the sensitivity analysis roll rate is not the most important factor in designing the aircraft for the fastest track time. Due to this reason, it was decided to lower the maximum roll rate in order to reduce the drag of the aircraft.

If the client requires a higher roll rate for wing 2, the wing could be altered by lowering the wing span. Doing this means that the aspect ratio of the wing has to be lowered. As shown by wing 1 this is feasible and the roll requirement can be achieved. However, both wings are designed for the purpose of choosing the appropriate one per race. Therefore, if analysis shows that a higher roll rate is required for a particular race, the client can choose to fly with wing 1.

Table 12.2: Aircraft statistics and main characteristics

Characteristic	Sukhoi Su-31	Zivko Edge 540	MXS-R	Extra 300L/S	Extra 330LX	Corvus Racer 540	Avinya Wing 1	Avinya Wing 2
V_{ne} [kts]	243	230	230	220	220	243	230	
V_{stall} [kts]	57	51	58	55	55	50	51	
Max. ROC [m/s]	24	18.8	17.78	16.25	16.25	18	24.7	25.0
Max. roll rate [°/s]	401	420	420	400	420	440	420	398
Max. load factor [g]	$-10, +12$	± 10	± 14	± 10	± 11	± 12	± 10	
OEW [kg]	700	531	572	672	660	685	560	567
MTOW [kg]	1050	703	726	820	820	700	708	714
Price [$]	320,000	295,000	410,000	245,000	407,500	250,000	300,000*	

* Production cost price

Comparing Avinya to the current market, a conclusion can be drawn with respect to the feasibility of the aircraft. The current market along with the Avinya's parameters can be seen in Table 12.2. Evaluating the parameters of Avinya, it can be seen that is has a competitive maximum and stall speed. The maximum rate of climb is far higher than the rest, whilst the roll rate is competitive. More specifically, wing 1 does meet the requirement while wing 2 has a slightly lower roll rate which allows for lower drag and a higher rate of climb. The maximum load factor is lower than some competitors, however as the regulations of 2014 have changed there is no need for a load factor of 12. Therefore, it was possible to achieve a very low weight.

The price of the aircraft is based on the production costs and is thus not equal to the retail price. As an extra income is necessary in order to cover the development and testing costs, this price will higher depending on the number of units.

Chapter 13 - Manufacturing and assembly plan

The concept is finished and found to be feasible, but before the aircraft can be build, a detailed design has to be made and a manufacturing plan set-up. The entire process of manufacturing and assembling the aircraft and the related resource acquisition and management procedures are visualised in Fig. 13.1. This chapter reflects upon the manufacturing of the main components, as well as providing an assembly plan on how the main components are combined into an aircraft. First, in section 13.1 methods on how to manufacture the main components are discussed after which, in section 13.2, an overview of the Avinya assembly is provided.

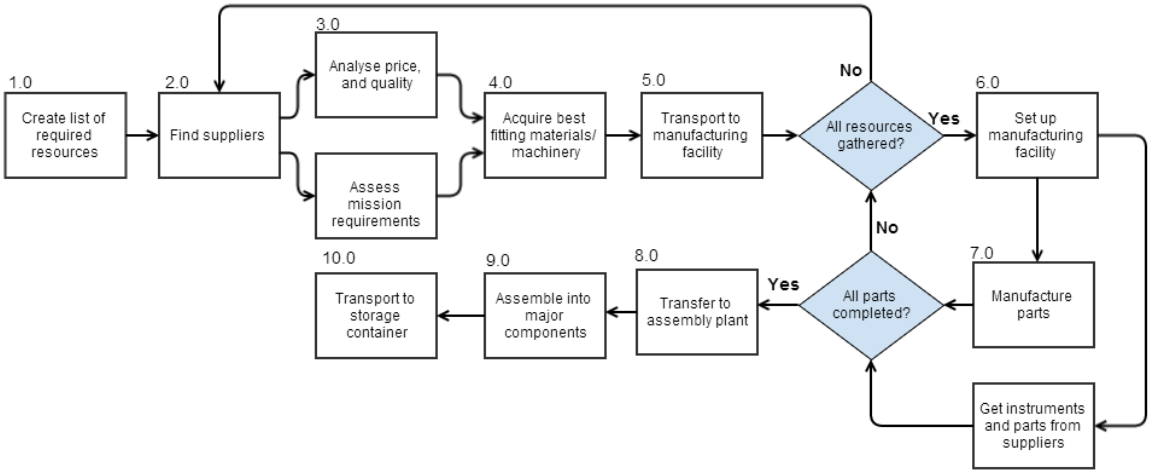

Figure 13.1: The resource acquisition and manufacturing of Avinya

13.1 Manufacturing of components

When manufacturing the main components of the aircraft, one has to account for the availability of materials and their standardised sizes, in order not to drive material (and manufacturing) costs up. Asides from this, the required raw material volume has to be multiplied by a factor of at least two in order to account for the material loss during production and required material for repairs during the life-time of Avinya. In the following section an overview of the designed components with their considered manufacturing methods is provided and discussed.

The material components of Avinya mainly exist of epoxy/HS carbon fibre composites and low alloy steel, AISI 4130. Only the manufacturing techniques feasible for these materials are analysed.

13.1.1 Manufacturing of epoxy/HS carbon fibre composites

The options for manufacturing of composites are restricted to the processes stated in Table 13.1. Pultrusion, for example, is one of the processes that cannot be applied specifically for the wingbox, as it is a tapered wingbox with decreasing thickness, width and height towards the root.

For both the wingbox (canard, rudder and wing) as well as the aerodynamic airfoil/fuselage coverings of Avinya it is decided to use autoclave molding, shown in Fig. 13.2, combined with hand lay-up and the use of prepregs as well as the use of vacuum bagging. The main advantage of this is that a high quality product with high strengths can be achieved and the environmental impact can be minimised during manufacturing. Avinya being a unique aircraft, produced in a small batch of maximum 5 aircraft, can be supported by research centres, such as universities, to

Table 13.1: Overview of manufacturing processes for carbon fibre composites [40].

Process	Advantage	Disadvantage
Automatic tape placement, ATP	Use of prepregs, resulting in minimised resin use. High achievement of accuracy, quality and repeatability.	Relative cost index (per unit) is very high and it is a slow process.
Filament winding	Axisymmetric hollow parts, such as tubes can be produced with relative ease and resulting in high strength products. Relative cost index is low to medium.	Only for axisymmetrical parts and requires low viscosity resins that are more hazardous.
Pultrusion	Typically used for rods, tubes, I-beams, Relative cost index is low.	Only for long shapes with constant cross section and thin walls.
Autoclave molding	Used for achieving high fiber volume, vacuum allows for extraction of environmentally unfriendly solvents.	Relative cost index is high.
Hand lay-up	Tooling cost are not very high. Most widely used for (unique) products in small batches.	Relative cost index is high. Requires low viscosity resins that are more hazardous. Open mold process.
Vacuum/pressure bag	High quality dense products, tooling cost are not very high (vacuum pump required). Relative cost index better than for ex. hand lay-up.	Semi- open mold process, disposal of bagging might be environmentally harmful.
Resin transfer molding (vacuum assisted), RTM/VARTM	Can be used for complex shapes. Relative cost index is low to medium. Worker exposure to chemical environment reduced. Mold costs low, economic for small batches.	Quality not very high, fibre to resin ratio worse. Use of dry fibers, mechanical properties not defined until after testing.

decrease cost resulting from the use of an autoclave. Note that the wingbox has to be manufactured in parts, being front and rear spar and the connecting skins. These will be bonded by the use of adhesives and connecting flanges as produced by pultrusion. Riveting of composites is not desirable, as it significantly weakens the structure. The moulds required for the process can be re-used for the remaining aircraft in the batch.

Asides from shaping the structure, the product can undergo additional surface treatments, such as painting, printing, polishing, texturing or coating. These will aid especially the aerodynamic airfoil/fuselage coverings.

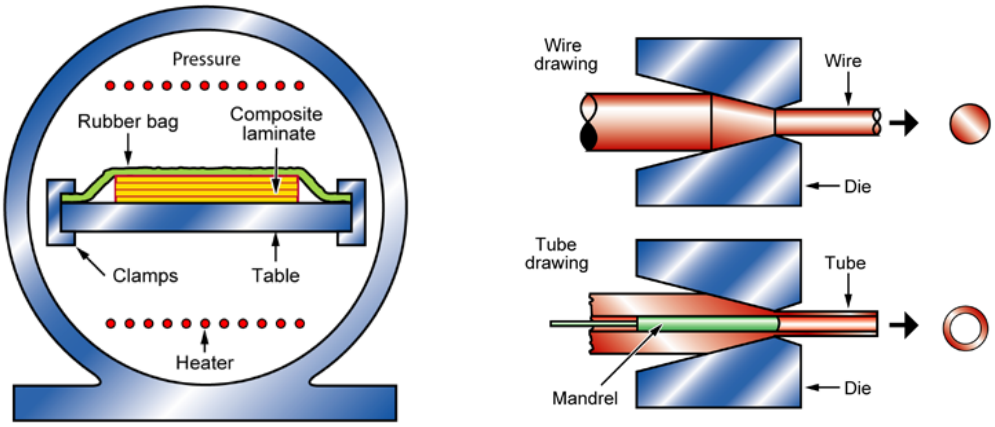

(a) Autoclave process **(b) Drawing process**

Figure 13.2: Selected manufacturing processes for wingbox and fuselage construction [40]

13.1.2 Manufacturing of components out of low alloy steel, AISI 4130

The options for manufacturing of steel products are restricted to the processes stated in Table 13.2. A wide variety of processes can be applied, thus choosing a manufacturing process is highly depending on the final product requirements as well as geometry.

Table 13.2: Overview of manufacturing processes for low alloy steels [40].

Process	Advantage	Disadvantage
Drawing	Relative cost index (per unit) low. Typically used to making seamless tubes, rods.	Limited to long shapes with uniform cross sections (square, cylindrical), only for ductile metals.
Extrusion	Relative cost index (per unit) low. Typically used for aircraft structural parts, tubing.	Limited to long shapes with uniform cross sections (square, cylindrical), only for ductile metals.
Forging/rolling	Complex shapes possible, typically used for highly stressed mechanical parts, such as crankshafts, connecting rods. Homogeneous (but anisotropic) internal structure, good mechanical properties and structural integrity.	Relative cost index medium. Over-spray of lubricants. Tolerances and surface finish usually poor, in need of further processing.
Sheet forming	Most commonly used with metals, steels, for automobile body parts, panels.	High tooling costs. Thickness limited to available sheet size.
Machining	Wide variety of machining disciplines. Both axi-symmetric as non-symmetric products.	Wide variety of relative cost index, very low to very high. Highly depending on complexity of product.

Since the fuselage structure consists of a tubular space frame, drawing or extrusion are highly suitable manufacturing processes, shown in Fig. 13.2. Relative cost index is low as well and since the fuselage structure consists of simple tubing, the fuselage can be produced fast. In combination with high quality welding, such as TIG, structural integrity of the frame can be ensured. In addition, maintainability and repairability are factors that do benefit from this manufacturing process.

13.2 Assembly of components

If all components have been produced, assembly can be initiated. A flow diagram is created to visualise a possible assembly method for the Avinya aircraft. It is applicable for both an aircraft that has not yet participated in the RBAR, and an aircraft being transported from one race track to another, and shown in Fig. 13.3.

In Fig. 13.3 multiple steps have been assigned to ensure integrity and functionality of the main components. The canard is assembled and installed subsequently from the engine support as it has to balance the structure and prevent it from tipping over during assembly. The engine is installed with it's wiring and control systems, batteries and/or fuel compartment (depending on type of engine, these components have different proportions). After which the wing, aileron, vertical stabiliser and rudder are installed and checked for functionality. Lastly, the propeller is installed and the whole aircraft is checked on operationability. Once that is successfully completed, all fairings/covers are installed and a licensed aircraft inspector has to approve of the aircraft.

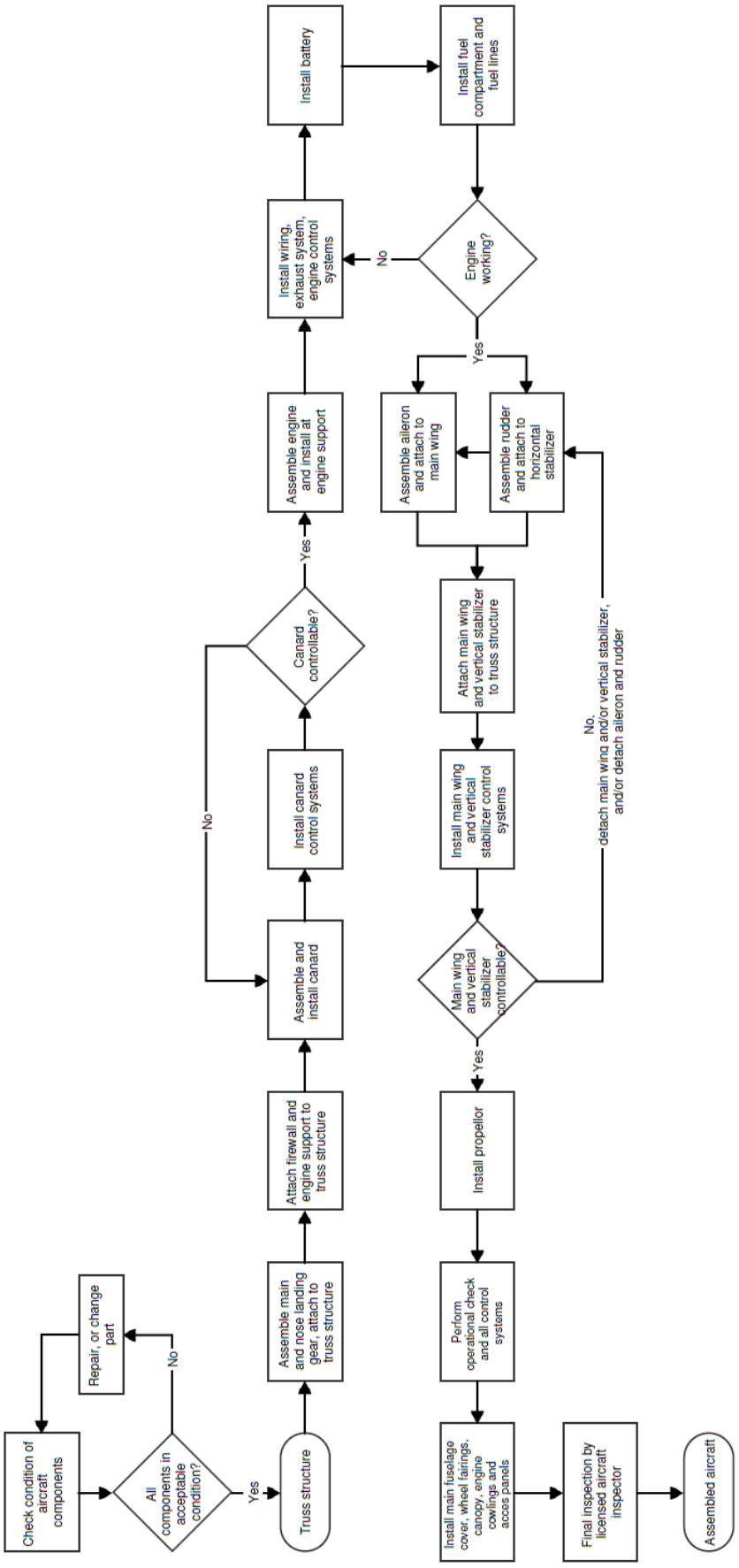

Figure 13.3: Assembly flow diagram

Chapter 14 - Planning for future processes

To make sure the manufacturing plan can be performed in time, a planning has to be made. This planning contains the detailed design, manufacturing and testing of the aircraft. These tasks have to be completed before Avinya can compete in the Red Bull Air Races.

First the detailed conceptual design has to be finished including a more detailed production plan. Again several iteration loops between the five technical departments will take place. While the detailed design phase is still going, work places and tools have to be arranged so the manufacturing can start directly once the design is finished. If the aircraft is manufactured several tests such as a stress test have to be performed on the ground, before going on the first flight test for certification. The last step before competing in the air races is to convince Red Bull that Avinya does add value to the race, while still being safe. An overview of these activities is given in Fig. 14.1.

The corresponding Gantt chart of the activities can be found in Fig. 14.2. In this Gantt chart it is assumed that multiple persons are working full time on the aircraft. Starting off with ten, while increasing over time for the more detailed stages. There is no special time reserved for contingency, but the assigned time to each task is longer than needed. So more contingency can be build in when generating the detailed Gantt charts. According to this planning the aircraft will be finished in September 2016, it will be certified, registered and ready to sell to the client in November 2018.

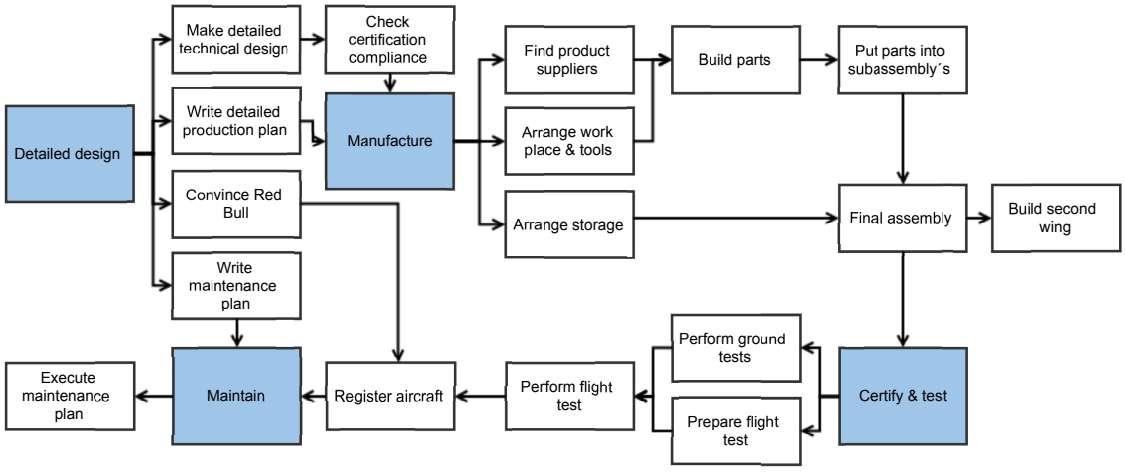

Figure 14.1: Overview of tasks performed after the conceptual design phase

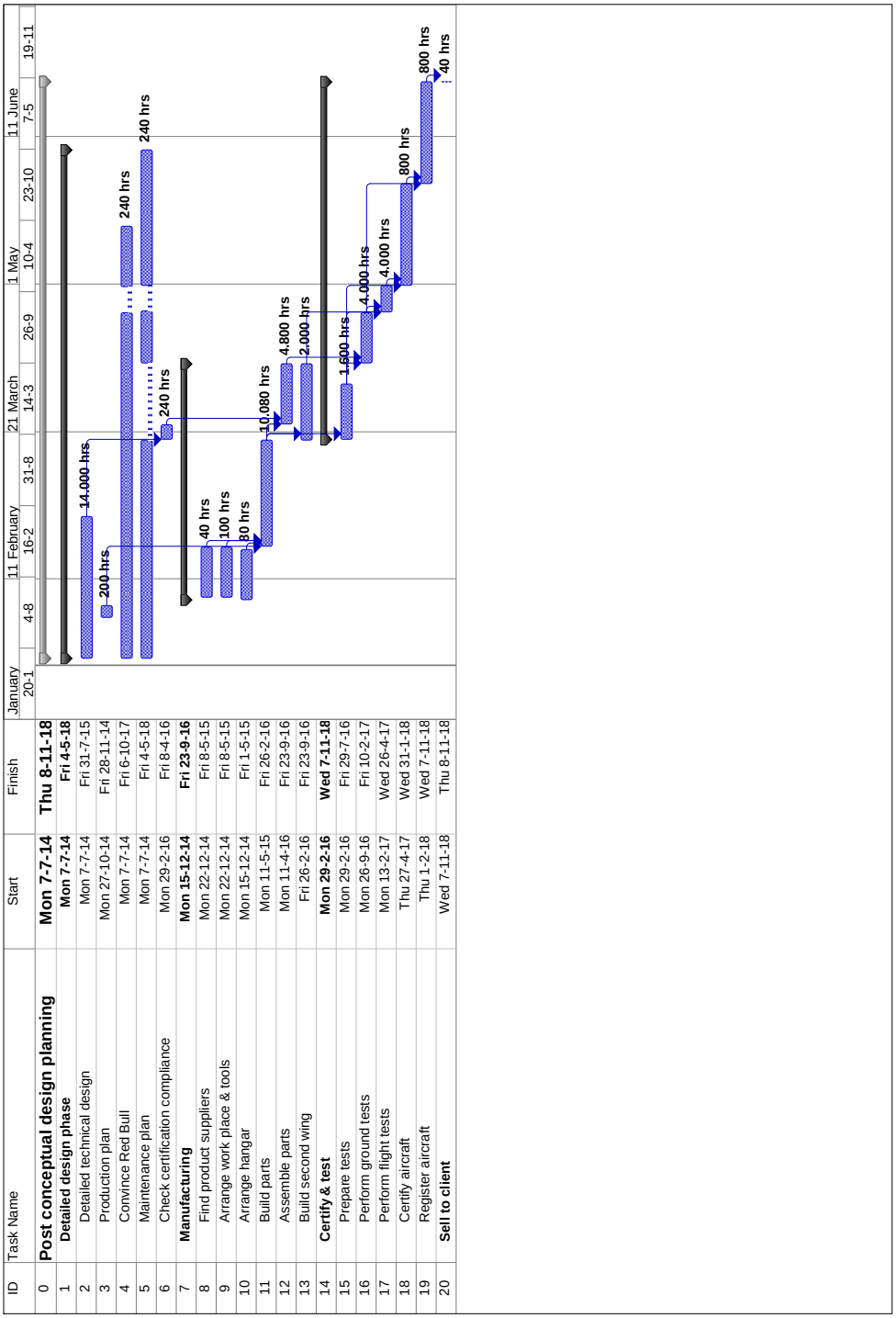

Figure 14.2: Gantt chart of the tasks after the conceptual design phase

Chapter 15 - Life cycle cost

A planning is made for the detailed design, manufacturing and testing. During these phases money will be spend on labour and materials. Also in the later stages of the aircraft life costs will be made. This section elaborates upon all these costs.

In order to produce a competitive aircraft, not only the performance but also the cost must be competitive. “As over 70% of the total life cycle cost of a product is committed at the early design stage, designers are in a position to substantially reduce the life cycle cost of the products they design, by giving due consideration to life cycle cost implications of their design decisions.” [44]. In order to keep costs down it is imperative when going from the conceptual design to the final design phase to carefully analyse the life cycle costs so that during the detailed design the cost implications can be taken into consideration. This chapter identifies the three product development life cycles, their stages and costs in section 15.1 and then organises the total product cost in a cost breakdown structure in section 15.2. A more detailed life cycle cost estimation will need to be done in the detailed design.

15.1 Life cycles

There are three parallel life cycles that need to be considered in life cycle product design: the product life cycle, the process life cycle, and the logistic support life cycle. The three life cycles are displayed in Fig. 15.1.

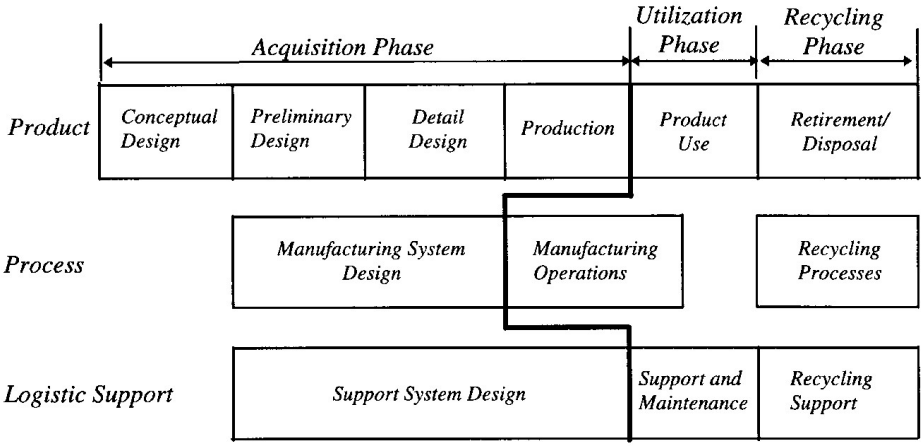

Figure 15.1: Parallel life cycles in product development [44]

The life cycle of the product starts with the identification of the design requirements, this has been done in the Baseline report. It continues with the design, the customer use, support, and finally, disposal stage. These topics are adressed in the mid-term report and this report.

The process life cycle starts with the manufacturing system design based on the preliminary product design. This consists of planning the production, layout of the production location, selection of equipment, and planning of the process. For information on this phase the reader is directed to chapter 13.

The logistic support life cycle, which deals with the logistic support operation, should also be started at the preliminary design phase. It involves the development of support for the design and production phases, support for the customer, maintenance or maintenance support during the life of the product, and support for product recycling or disposal.

An overview of all the associated costs for the life cycle stages are displayed in Fig. 15.2.

	Company Cost	Users Cost	Society Cost
Design	Market Recognition Development		
Production	Materials Energy Facilities Wages, Salaries Etc.		Waste Pollution Health Damages
Usage	Transportation Storage Waste Breakage Warranty Service	Transportation Storage Energy Materials Maintenance	Packaging Waste Pollution Health Damages
Disposal/ Recycling		Disposal/ Recycling Dues	Waste Disposal Pollution Health Damages

Figure 15.2: Associated costs to product life cycle stages [44]

15.2 Cost breakdown structure

The cost breakdown of the Avinya concept is a decomposition of the life cycle cost into various categories. The cost breakdown structure is depicted in Fig. 15.3

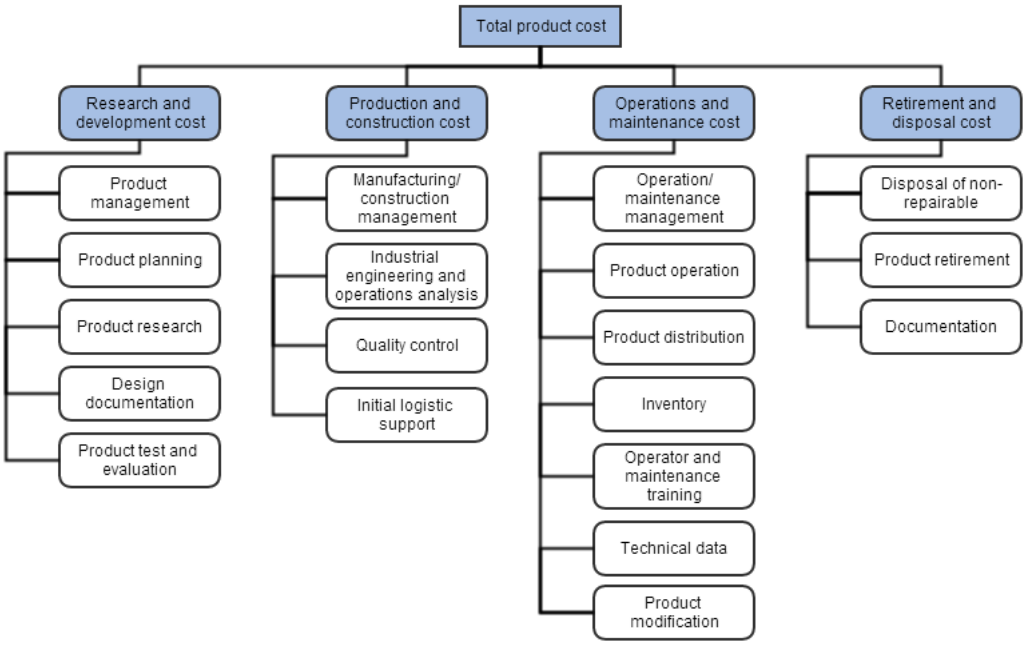

Figure 15.3: Cost breakdown structure of the Avinya concept

Chapter 16 - Reliability, Availability, Maintainability and Safety characteristics

The costs were determined based on the assumption that no major mistakes are made. In this chapter the RAMS characteristics of the project will be discussed to limit the amount of unforeseen costs. This will be done by discussing the separate parts one by one starting with the reliability and ending with the safety. This RAMS is a future plan and will be operative in further stages of the plan.

16.1 Reliability

In this section a list of critical functions will be given that influence the reliability of the aircraft. For example it is important to find likelihood that a engine failure occurs during the mission time. To establish a proper reliability management a reliability and maintainability plan is produced and shown below [45]. This plan will ensure that the aircraft will ensure quality and be reliable during its entire lifetime.

16.1.1 Reliability and maintainability plan

RELIABILITY MODELLING

Reliability block diagrams will be constructed in order to model the reliability for the aircraft and all its subsystems. This model will be continuously updated to the current state of the design. The reliability block diagram will have to be agreed on by all the stakeholders and will be controlled by the future project RAMS engineer.

RELIABILITY PREDICTION AND APPORTIONMENT

The reliability prediction will be carried out, covering all areas of design following the guidelines set out in the RBAR regulations ([1]) and the FAA certification ([46]). The reliability of the aircraft will be submitted to the client and will be discussed. If applicable redundancy will have to be added regarding preventing actions, compensating factors or the effects on safety in order to assure quality and safety throughout its lifetime.

FAILURE MODES, EFFECTS AND CRITICALITY ANALYSIS

Software will have to be used to create and record the failure modes, effects and critical analysis. Again if applicable extra redundancy will have to be added regarding preventing actions, compensating factors or the effects on safety in order to assure quality and safety throughout its lifetime.

FAULT TREE ANALYSIS

A fault tree analysis will be done on equipment designs where a high occurrence of failures is present. The high failure sensitive parts will discovered during the analysis.

RELIABILITY TESTING

Reliability of the actual aircraft will have to be tested using an integrated test programme. The main features of the test approach will be :

- Reliability of the engine
- Reliability of control surfaces
- Reliability of the landing gear
- Reliability of the structural integrity

FAILURE REPORTING AND RAMS MONITORING

During further design and development phase of the project will perform failure reporting, analysis and corrective actions. Failure reporting action will be taken on all failures that occur on hardware and the software used on the

tests and trials performed during the detailed design and development phase of the project. Also failures during production testing will be reported and managed. The results of the failure reporting will be monitored during all the tests.

PRODUCTION RELIABILITY ASSURANCE
To assure the quality of the product, a plan needs to be produced that describes the methods that will be applied in advance and during production. This will ensure that the production systems will achieve the wanted reliability level.

MAINTAINABILITY ANALYSIS AND DEMONSTRATION
To ensure that the requirements will be met, the maintainability will be analysed and measured during detailed design and development respectively. Preventive maintenance methods will have to be established and performed using the reliability issues found earlier.

IN-SERVICE RAMS MONITORING
While the aircraft is in service the RAMS will have to be monitored, to ensure the reliability and quality throughout its life-time. Shortcomings or failures will have to be investigated and corrective changes smoothly integrated.

16.2 Availability and maintainability actions

The availability expresses the ratio between delivered and expected service. This ratio can be improved by adding redundancies in for example the engine. Having a second engine would ensure a higher probability that the aircraft will be able to compete in an upcoming race when engine #1 fails. For this reason a good reliability planning will induce a greater availability of the aircraft. Another factor that will have a positive effect on the availability of the aircraft is the widely availability of the materials that are used in the aircraft. Since the use of composite materials is not new anymore and Avinya does not use any exotic materials, the availability of the aircraft is not negatively affected.

The maintainability of the aircraft is also influenced by the choice of materials and structures used. Since Avinya has composites wings with a composite wingbox, the accessibility during maintenance is more difficult. These structures will have to be checked for integrity with help of x-ray crack detection technologies. The truss structure used on the other hand is easier for maintainability than for example a monocoque structure and also ensures better accessibility for e.g. the engine. Either way the aircraft should under go maintenance checks and inspections, scheduled and non-scheduled.

Scheduled
Scheduled inspections include pre-race inspections as well as post-race by the pilot [1]. The scheduled inspections consist of:

- Radio, transponder and race specific equipment check
- Check of all required safety equipment (Harness, helmet, parachute, spare air)
- Check the structural integrity of the wingbox and fuselage structure
- Check the structural integrity of the landing gear
- Check engine and propeller
- Check the control surfaces
- Etc.

Non-scheduled
After a G load excess the regulations also states that extra non-scheduled inspection has to be performed [1]. These

non-scheduled inspections consist of:

- Inspection for bending of fuselage structure
- Inspection for bending and fractures at wing and empennage attach bolts
- Engine mount inspection for cracking and distortion
- Check composite parts for delamination
- Inspect flying surface skins for rippling and distortion
- Etc.

16.3 Safety

To ensure safety while operating Avinya, proper safety engineering is necessary. Therefore, a hazard analysis will have to be performed to all areas of design responsibility. These hazard can be an engine failure of the jamming of a control surface. System and subsystems have to be analysed for hazards which have not been examined before, including component fault modes, critical human errors and hazards. These events will all have to be shown in an event tree and if applicable eliminate or reduce impact by adding redundancies or supporting mechanisms. Finally a hazard tracking will have to be done. This will be applied to all conditions which could possibly produce catastrophic effects. They will be identified and eliminated of reduced up to a level at which the client thinks it is acceptable. It will be ensured that the hazard tracking is done properly maintained and available for the client.

Chapter 17 - Sustainability considerations

Besides the maintainability and reliability of the aircraft, sustainability is nowadays seen as important as well. The sustainability considerations for the Avinya span three phases of the aircraft life: manufacturing, operations and end of life disposal. In the manufacturing phase the key considerations are the materials used and the processes applied, namely ensuring that minimal pollution is created and that the sustainability of the material choices are factored into material choice. The operations phases focuses on the possible integration of an electric engine as well as a more environmentally sustainable method of producing the smoke needed during the races. Finally, the end of life evaluates options for material disposal and aircraft disassembly such that components and materials can be re-used.

17.1 Manufacturing

Currently techniques are available to produce carbon fibre from the waste that is produced during fractional distillation of oil [47]. This is advantageous given that the raw material would otherwise be wasted and thus would be a great source from which to obtain carbon fibres. It is however of vital importance that the carbon fibres obtained are of a suitable grade for the aerospace industry and specifically, the Avinya concept. Thus, whilst it is important to ensure the material is obtained responsibly from a (more) sustainable process, the low series number and high performance demands of this aircraft mean the quality of the fibres are simply non-negotiable.

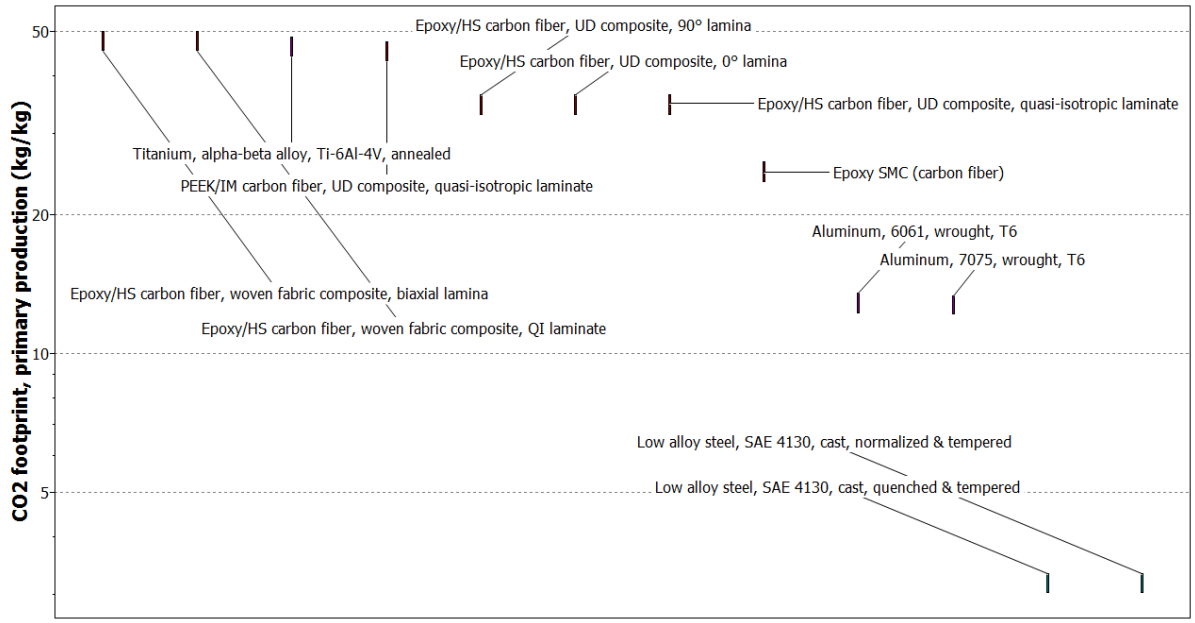

Figure 17.1: CO^2 footprint for primary production of selected materials

In addition the manufacturing of carbon fibres (through for example dry spinning) produces many air pollutants such as “volatilized residual monomer, organic solvents, additives, and other organic compounds used in fibre processing” [48]. Of course steel and iron manufacture also emit significant pollutants such as organic carbon, cyanide, fluoride and zinc [49]. Given that the design includes significant amounts of carbon fibre and steel, including waste management in the manufacturing process is key to ensuring minimal pollutants being released into the atmosphere. Accounting for the current research being done and funding being provided for example by Boeing (1.89 million British pounds) [50] into pollution reduction during carbon fibre manufacture it would be wise to make use of these methods. Furthermore the option of using pre-existing facilities should be explored given the low series number of the aircraft and the significant costs of setting up a fabrication plant or factory. Whilst the

factory set up by Boeing in collaboration with BMW in Wackersdorf has state of the art facilities and sustainable techniques, it is likely going to be set up for large series production and thus not suitable for this type of aircraft. It may be better to keep manufacturing local, for example at Fokker aerostructures or Airborne as this would limit emissions in transporting parts and potential labour back and forth.

17.2 Operations

The RBAR regulations require that oil be burnt at not less than 2.5 litres per minute in order to produce the smoke needed during the race [1]. This process in itself is very wasteful, particularly if traditional fossil fuel based oil is used. The exploration of an alternative system based on for example vegetable oil/bio-diesel could potentially reduce the harmful emissions. In particular sulphur emissions are non existent with such a fuel [51]. Whilst a bio-diesel based replacement could potentially be directly implemented into the current system, a more radical change would be to replace the system entirely and include a water vapour based smoke generator. Currently no such system is available which could be directly implemented into a RBAR type aircraft, thus this technology will have to be designed and incorporated by the manufacturers and is left as a future development discussion.

An additional option to reduce localised emissions and thus ensure more sustainability would be to incorporate an electric engine.

First the feasibility of the electric engine needs to be examined. To this end it needs to be seen whether current batteries can provide the energy density necessary to power such a mission. The energy required is computed by examining the typical aircraft mission. This involves taking off and climbing at close to full power for approximately 2 minutes, followed by a 15 minute cruise to the race track, where a 1 minute burst of maximum power is used to compete and finally the mission is ended by another 15 minute cruise back to the home base.

Thus the power needed is broken up as follows:

- 2 minutes at 90% power
- 15 minutes at 70% power
- 1 minute at 100% power
- 15 minutes at 70% power

Given that maximum power is 235 kW, this amounts to a total of 93.2 kWh of energy needed. When including battery efficiency of 0.8, propeller efficiency of 0.9 and shaft efficiency of 0.95 the total energy needed becomes 136.3 kWh. With current lithium-ion cells producing a maximum of approximately 0.17 kWh/kg [52], it can be seen that 802 kg of cells would be needed which is simply not feasible on such an aircraft. In order to have the same amount of battery weight as current fuel weight the specific energy of the batteries would need to exceed 1.9 kWh.

The inherent advantage of such a configuration is that the batteries can be placed near the c.g. of the aircraft and thus no c.g. shift takes place during flight which results in more predictable behaviour for the aircraft. Furthermore instant torque availability means concepts like these have large potential for future development provided the energy source can be found to power it. However currently it is the energy source that is holding back this concept.

17.3 End of life disposal

When looking at the two major material components in the Avinya design, namely carbon fibre and steel, it is clear that the end of life disposal of the metal components is far easier given its ability to be melted down and re-used. Carbon fibre on the other hand is usually incorporated into a ‘matrix’ made up of another material and this significantly complicates the recycling process. Currently the majority of CFRP waste is landfilled [53]. Furthermore carbon fibre recycling is currently considered as “non-existent” [40] however research has resulted in some techniques such as pyrolysis and mechanical recycling which recovers large portions of the original material

[54]. Of course some of the original material is lost in this process and the quality is not always at the same grade as it was prior to recycling. However it remains the most promising avenue for end of life disposal should it be required.

Chapter 18 - Technical risk assessment

While the aircraft has to be sustainable, even more important is to limit the risks during flight. During the design and manufacturing of the project several risks occurred and had to be handled in order to limit the delay of the design. In the detailed design phase the same risks can happen and the same mitigation strategy will be applied. Since this procedure is known, it is now more important to look at the technical risks associated with the execution of the mission. These pertain to any potential hazards or occurrences that would reduce the ability of the aircraft to perform its mission successfully.

The technical risks can have a critical impact, since failure of one of the components can lead to failure of the entire aircraft, with a possible aircrash and related effects as consequence. Due to the fact that the consequences are so serious the likelihood of the events have to be as small as possible in order to avoid too large risks. Therefore it appears that the likelihood is not particularly high. The consequence and likelihood of all the risks can be found in the risk map in Fig. 18.1.

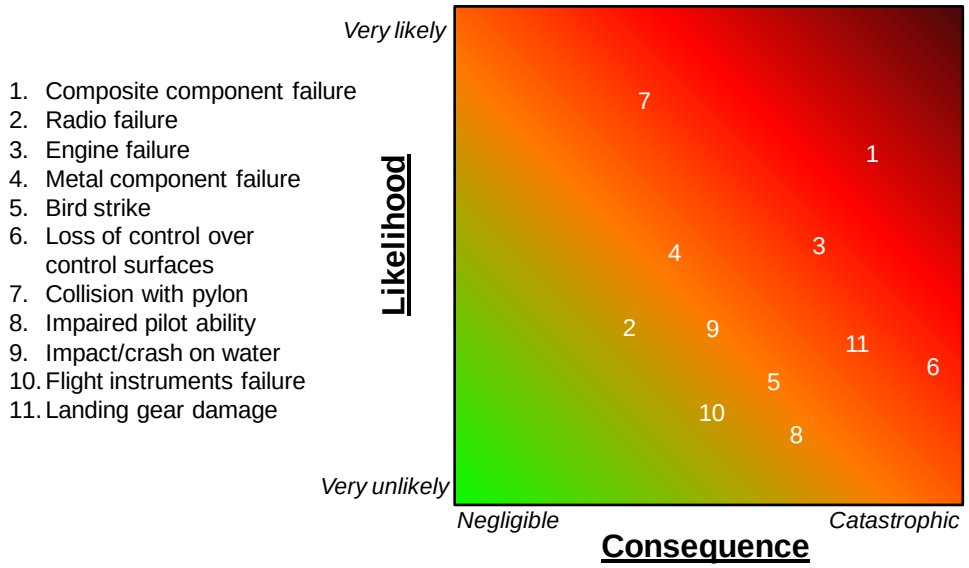

Figure 18.1: Risk map of mission risks

Although the likelihood of the risks is kept as small as possible, they can still occur. To limit the consequences when a risk is happening, it is critical that the pilot and the team know how to react. Also some events can be mitigated by pre-race checks, which have to be performed by members of the race team or organisational body of RBAR. The risks with a relatively high likelihood or consequence are described in the risk register in Table 18.1. In this risk register the cause, risk event, consequence and mitigation strategy are described.

Table 18.1: Mission risk register

#	Cause	Technical risk event	Consequence	Mitigation strategy
1	Delamination of composite structures	Composite component failure	Aircraft flight capability compromised	Regular inspection
2	Critical radio component failure	Radio failure	No communication to ATC authorities/team	Add backup system for redundancy
3	Critical engine component failure	Engine failure	Race has to be aborted, glide to safety	Regular inspection and service, practice engine failure procedures
4	Fatigue of metal structures	Metal component failure	Aircraft flight capability compromised	Regular inspection
5	Birds in the track area	Bird strike	Damage to aircraft, inhibited flight capability	Birds of prey used to clear course, noise used to scare away birds
6	Mechanical system failure	Loss of control over control surfaces	Aircraft controllability (critically) reduced	Regular inspection, add redundant systems as back ups
7	Pilot error	Collision with pylon	Possible aircraft damage	None
8	Pilot sickness	Impaired pilot ability	Dangerous/fatal situations in flight	Open communication with team and pre-race check
9	Pilot error/mechanical error	Impact/crash on water	Damage to aircraft, injury to pilot	Raise pylon height (already done for 2014)
10	Pitot/static vent blocked	Flight instruments failure (altimeter, airspeed indicator)	Abandon race	Pre- flight check, practice procedures
11	Impact/material fatigue/delamination	Landing gear damaged	Unable to perform regular landing procedure	Find a soft field to land on, accept risk and land on regular runway

Chapter 19 - Communication and hardware interactions

This chapter elaborates on all the interactions between various components in the aircraft. Sections 19.1 to 19.3 present the electrical, hardware, communication and data handling diagrams.

19.1 Electrical block diagram

The aircraft contains several systems which require electricity. A short description and overview are given in this section.

Aside from the essential systems, most electrical systems aboard the aircraft are due to the regulations of Red Bull. These state that four cameras need to be installed and are recording during flight. Doing so, the audience can see the pilots manoeuvres from various angles on big screens during the event. In addition, the recordings are used to broadcast the event through various media channels such as television and Internet streams.

In order to broadcast the recordings and correspond with the pilot, a communication link to the to the ground station needs to be established. For this purpose, a camera control and transmission (CCT) box has to be installed in the aircraft [1, art.10.1]. Furthermore the position, time, acceleration, pressure, engine data, angles and angular velocity of pitch, roll and yaw have to be sampled, stored and/or transmitted [1, art.9.9]. The power needed to measure, sample and store this data is provided by a battery. All of these sensors and systems are checked pre-flight to make sure they are working properly.

To provide power to the electrical systems and charge the battery during flight, an alternator is installed to convert the mechanical energy from the engine to electricity. On ground, the battery is charged by making use of the ground system.

Normally, an aircraft is started using an electrical ignition. However, regulations state that no electrical ignition is allowed and only magnetos should be installed to start the engine as stated by the regulations [1, art.7.1]. This ignition system will be kept separate from the rest of the electrical circuit of the aircraft to ensure the engine will keep running in the unfortunately event of alternator or battery failure. The aircraft will have two magnetos, each fitted to one of the two spark plugs.

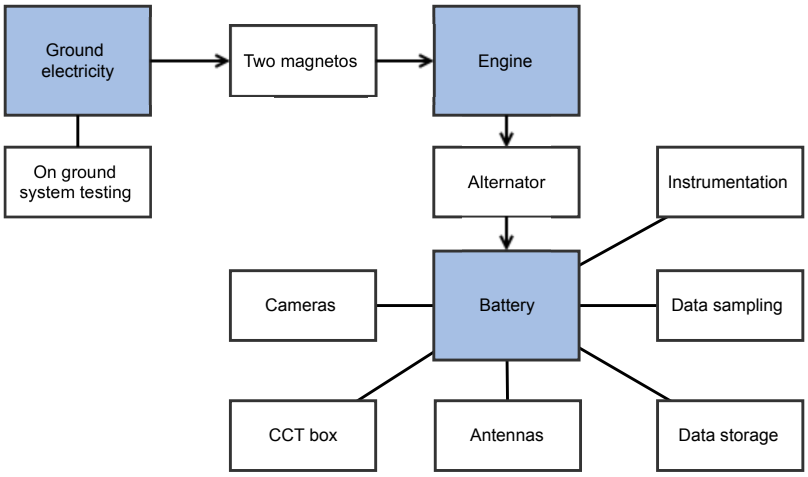

Figure 19.1: Electrical block diagram

19.2 Aircraft hardware interaction

Aside from the electrical systems in the aircraft, several non-electrical hardware parts are interlinked. As regulations restrict the use of Fly-By-Wire systems [1, art.6.4], the aircraft's mechanisms are directly connected to the pilot's controls. In Fig. 19.2, the pilot inputs with respect to the hardware interactions in the aircraft are shown. It has a very minimal set-up in order to save weight and have the best flying characteristics possible.

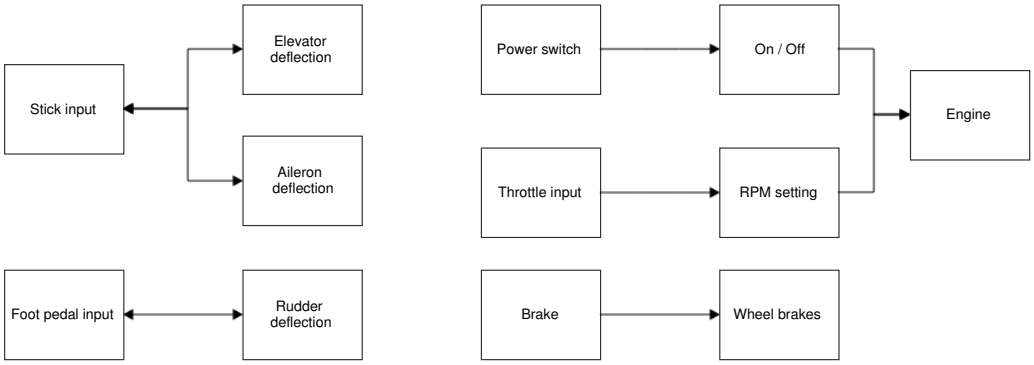

Figure 19.2: Hardware diagram indicating the interactions in Avinya

19.3 Communication and data handling

Even though the electrical circuit is in place, all the data needs to be processed and stored. This is largely for the jury of the race to make sure the pilots comply with all regulations.

The communication flow diagram shows the flow of data through the system and to and from its environment. The flow within the system is very one dimensional as the aircraft operates mechanically. The pilot input and the associated system action, as well as the interaction of the system with its environment can be seen in Fig. 19.3.

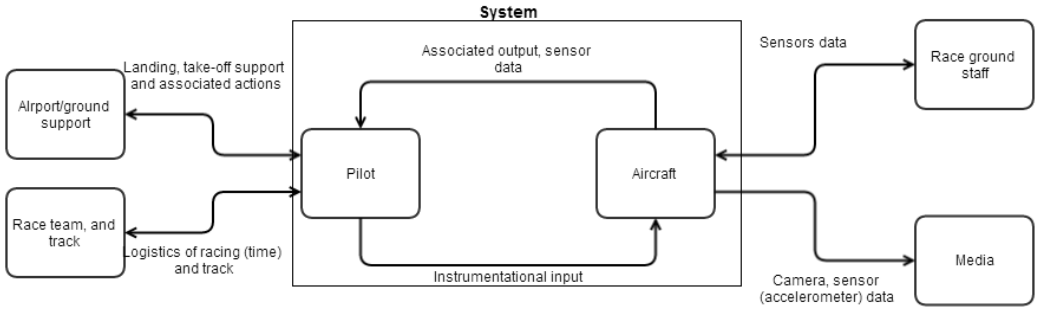

Figure 19.3: Communication to and from the environment

The major influential groups while operating the aircraft are the race authorities, the team and the media. The pilot and ground authorities communicate using Controller-Pilot Data-Link Communications as described by Rankin and Mattson [55], which includes communication management, control clearance data link, and microphone checks. During the actual race, the main flying guidelines are communicated between the pilot and race team via headphones. Furthermore the sensor data is communicated to the ground staff using antennas. These antennas are provided by Red Bull and checked after installation to guarantee they work. Finally the camera data and g loads are sent to the ground allowing the media to report the races live.

Chapter 20 - Conclusion and recommendations

In this chapter the conclusion of the report is presented, followed by recommendations for the future development of the project. In section 20.1 the final design of Avinya is described, accompanied by technical drawings and the most important performance characteristics. Section 20.2 outlines the future work that needs to be performed to complete the project and states the limitations of the current technical analysis. Recommendations are made to validate or improve design before the next phase of the project can be started.

20.1 Conclusion

The purpose of this project was to design a lightweight and customisable aerobatic race aircraft with a set of performance characteristics that exceeds those of RBAR competiters. This report focuses on the work done in the previous weeks where Avinya progressed from a conceptual design into a detailed design that is able to meet the requirements set by the clients. A rendering of the final Avinya design can be seen in Fig. 20.1.

(a) Front view

(b) Back view

Figure 20.1: Front and back view renders of the final aircraft design

The final design of Avinya is based purely on aerobatic racing and hence flying the challenging courses featured in the RBAR world championship in the fastest possible time. Therefore performance and trajectory optimisation has been an integral part of the aircraft design. Ultimately a design with modular wings was chosen to have the fastest aircraft on different types of tracks. The design features a canard with an elevator, followed by a sweptback main wing with vertical tails mounted at the wingtips and a pusher propeller at the rear. The propeller is powered by a

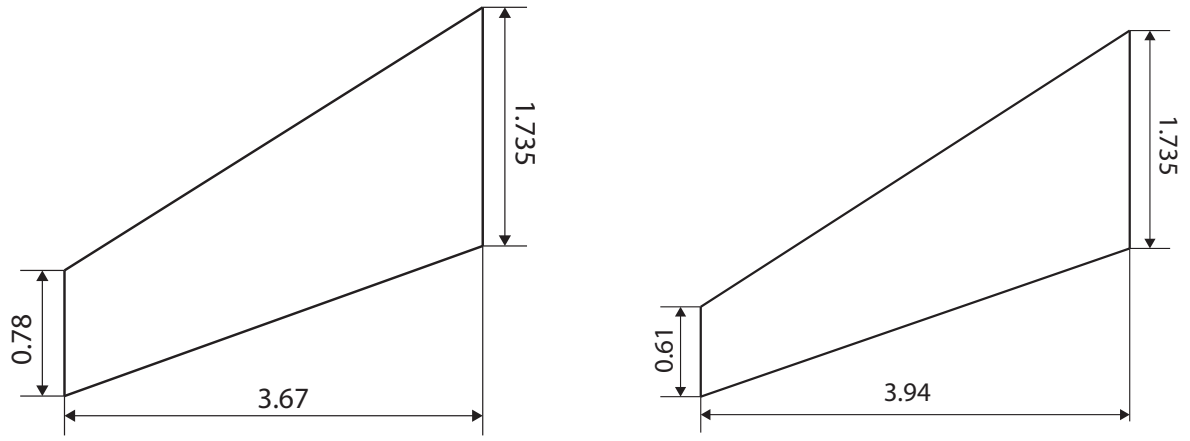

(a) Wing 1 **(b) Wing 2**

Figure 20.2: Sketch of wing 1 and wing 2, not to scale

piston engine, which is standardised in the current RBAR season. It was found, however, that the engine can be replaced by an electric model without major implications on the overall design. This would greatly improve the sustainability of the design, especially if combined with a less wasteful alternative for the current smoke system. The aircraft structure consists of a steel tubular space frame, while the skin and wings are made from carbon fibre composites. The approximate weight of the fuselage structure is equal to 71.6 kg, whereas the weight of the wingbox of wing 1 and 2 is estimated to be 41.2 and 44.4 kg respectively. Avinya features a fixed tricycle landing gear with a nose wheel and aerodynamic fairings to reduce parasite drag.

The OEW of the aircraft is equal to **560 kg**, while the $MTOW$ is **708 kg**. Both these weights are very competitive when compared to the aircraft currently competing in the RBAR. The two modular wings of Avinya are designed such that the surface area and the root chord are the same. The first is obviously to keep the lifting capabilities of the two different aircraft approximately equal and the latter is for assembly purposes. A visual representation of the different wing planforms is given in Fig. 20.2. When the aircraft is equipped with wing 2 rather than wing 1, the OEW, and hence the $MTOW$, is 7 kg larger due to a larger structural weight. As can be seen in Fig. 20.2, wing 2 has a larger aspect ratio and given the same surface area, a larger wingspan. This is a result of the fact that wing 2 is optimised for aerodynamic efficiency and rate of climb, at the expense of maximum roll rate. The performance analysis on the final design showed that Avinya equipped with wing 1 meets all requirements set by the clients as well as the regulations. When the aircraft is equipped with wing 2 the climb rate is larger, at the expense of not meeting the roll rate requirement. The geometrical parameters and performance characteristics of Avinya are presented in Table 20.1. The trajectory optimisation analysis showed that wing 1 performs better at tight tracks that involve a lot of turning and rolling manoeuvres, whereas wing 2 excels in tracks with longer straights and more climbing manoeuvres such as the half Cuban eight. A stability analysis was performed on the aircraft in flight, as well as on the ground. This resulted in the sizing and placement of stabilising surfaces such as the canard and vertical tailplanes, as well as the undercarriage to provide a coherent and integral design. The final design of Avinya is a synthesis of all different design aspects and is able to fulfil the goal set out at the start of the project. Technical drawings showing the overal design of Avinya, equipped with wing 1 can be found in Fig. 20.3.

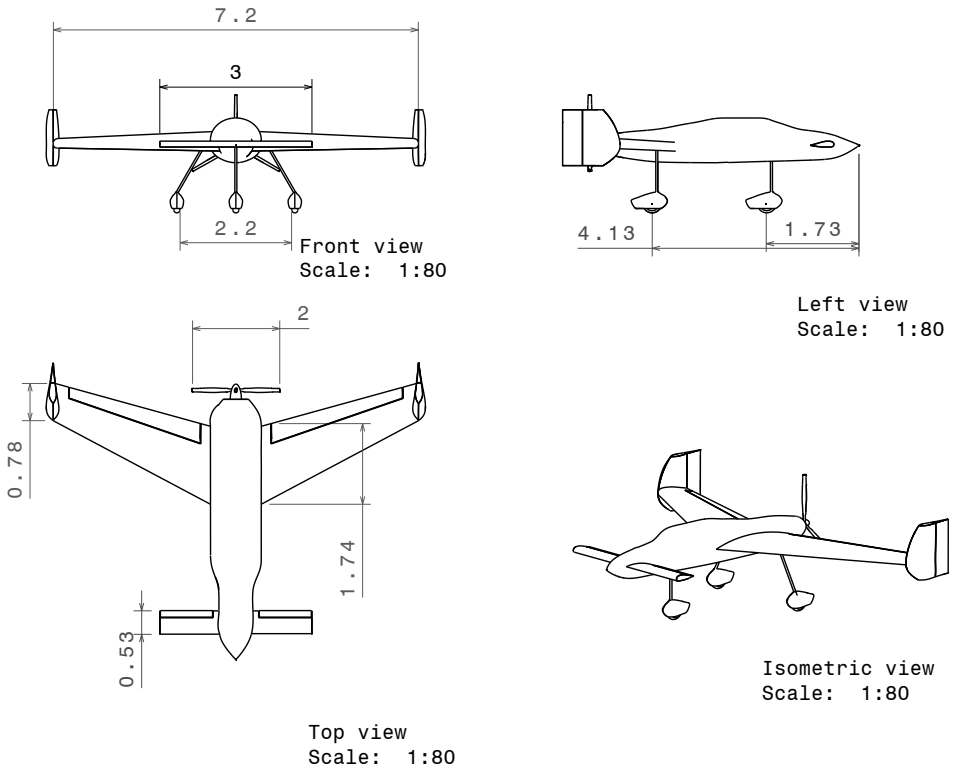

Figure 20.3: Technical drawing of final aircraft design

Table 20.1: Parameters and performance characteristics of the final design

Parameter	Wing 1	Wing 2	Unit
OEW	560	567	kg
$MTOW$	708	714	kg
S_c	1.8	1.8	m^2
S	9.23	9.23	m^2
b	7.34	7.88	m
A	5.84	6.73	-
c_r	1.74	1.74	m
λ	0.45	0.36	-
p	420	398	$^\circ/s$
ROC	24.7	25.0	m/s
q	93.8	94.2	$^\circ/s$

20.2 Recommendations

For the future development of the project, the most important tasks are to produce a design that describes the aircraft in full detail, a detailed manufacturing plan and to test the aircraft extensively. Wind tunnel tests will be necessary to obtain accurate values of aerodynamic and stability coefficients. This will also aid in validating the XFLR5 software to ensure that accurate approximations of characteristics such as lift distribution are obtained. Additionally this will give a more accurate estimate of the performance and allows design aspects such as balancing of control surfaces to be performed. However, before putting the design into a wind tunnel, a CFD analysis has

to be performed. This can be used to confirm the estimated aerodynamic coefficients which in turn provides the opportunity to iterate with a higher accuracy.

Furthermore the structural analysis presented in this report needs to be validated and improved if needed using advanced analysis tools such as finite elements analysis for the structural design. When the first prototype of the aircraft has been produced, static and flight tests will have to be conducted to validate the structural integrity and to perform a flutter analysis. The static tests in particular will allow the stresses in the fuselage and wing skin as well as in the wingbox and truss structure to be accurately determined. It would be useful to apply strain gauges in a wheatstone bridge configuration in order to determine the strains as well as subsequent stresses at limit loads. Furthermore the buckling criteria on the various structural components also needs to be tested and given the fact that carbon fibre is used, ensuring the directions of the loads conform to the predicted load paths and directions is vital.

Additionally, small changes in the design have to be made in order to reduce the stick forces. The force found from the elevator deflection is suitable for general aviation aircraft, but is too high for aerobatic aircraft. Probably the best way to reduce this force is by attaching balancing spades to the elevator. Research has to be done on whether this is actually the best method and on the size of these spades needed.

An important factor to note is that even though the modular wing design can give the aircraft an edge in competition, it does cause complications in terms of certification and testing. Basically all procedures need to be performed for two different aircraft. This is especially the case for the pilot, who has to put a lot of effort into familiarising himself with the aircraft. In order to have enough faith in the aircraft to perform the difficult manoeuvres at low altitudes, the pilot will have to make many hours of test flying with both wing configurations.

Furthermore research and development on a system that can replace the current oil based smoke system with a water vapour version or biodiesel version would be beneficial for sustainability and something that could be implemented across all aircraft flying the RBAR. In addition to this, the material selection which was conducted also considered environmental aspects such as processing (both in terms of ease and pollution), however more depth is necessary in order to determine exactly where materials are sourced from and where the processing shall occur.

Finally, as the design does not comply to the current RBAR regulations, a vital part of the future project development is to convince the race committee to change the regulations to allow Avinya to enter the competition by the year 2020. This will involve extensive testing, especially to demonstrate that aspects such as pilot safety are incorporated into the design.

Bibliography

[1] Red Bull Air Race Committee. *Red Bull Air Race World Championship - Regulations Part A to E*. Race Committee, March 2010 .

[2] Don George. Aircraft engines parts. `http://www.dongeorgeaircraft.com/lycoming.htm`. [Last accessed; 01/07/2014].

[3] Boeing. Pallets and containers. `http://www.boeing.com/assets/pdf/commercial/startup/pdf/CargoPalletsContainers.pdf`. [Last accessed; 19/05/2014].

[4] Erik Kay. Red bull air race rises to logistics challenge. `http://www.redbull.com/cs/Satellite/en_air/Article/Red-Bull-Air-Race-Rises-To-Logistics-Challenge-021242745716250`. [Last accessed; 19/06/2014].

[5] H. van der Plas and H. G. Visser. Trajectory optimisation of an aerobatic air race. *The Aeronautical Journal*, 113(1139), 2009.

[6] Red Bull GmbH. Abu dhabi race track gate coordinates. [Email correspondence], .

[7] Max D. Morris. Factorial sampling plans for preliminary computational experiments. *Technometrics*, 33(2), 1991.

[8] F. Campolongo, J. Cariboni, and A. Saltelli. Sensitivity analysis: the morris method versus the variance based measures. *Technometrics*, 2003.

[9] Jan Roskam. *Airplane design - Part 1: Preliminary Sizing of Airplanes*. Roskam Aviation and Engineering Corporation, 1985.

[10] RC Hibbeler. *Engineering mechanics: Dynamics*. Prentice Hall, 2004.

[11] J.A. Mulder, W.H.J.J. van Staveren, J.C. van der Vaart, E. de Weerdt, C.C. de Visser, A.C. in t Veld, and E. Mooij. *Flight Dynamics, Lecture Notes*. Delft University of Technology, 2013.

[12] Red Bull GmbH. Regulation amendments and abu dhabi race track data. [Email correspondence], .

[13] S. Gudmundsson. *General aviation aircraft design*. Butterworth-Heinemann, 2014.

[14] M.H. Sadraey. *Aircraft design, a systems engineering aproach*. J. Wiley & Sons, 2013.

[15] D.P. Raymer. *Aircraft Design: A Conceptual Approach*. American Institute of Aeronautics and Astronautics, Inc., 1992.

[16] David Gillespie. *An introduction to computational fluid dynamics*. Oxford University, 2014.

[17] Mark Drela. Xfoil: An analysis and design system for low reynold number airfoils. "`http://web.mit.edu/drela/Public/papers/xfoil_sv.pdf`". [Last accessed; 14/06/2014].

[18] D.J. Auld and K.Srinivas. Vortex lattice method (3-d). "`http://www-mdp.eng.cam.ac.uk/web/library/enginfo/aerothermal_dvd_only/aero/vlm/vlm.html`". "[Last accessed; 04/06/2014]".

[19] Brian Maskew. Program vsaero theory document. "`http://ntrs.nasa.gov/archive/nasa/casi.ntrs.nasa.gov/19900004884.pdf`", 1987. [Last accessed; 12/06/2014].

[20] Xflr5: Analysis of foils and wings operating at low reynolds numbers. "https://engineering.purdue.edu/~aerodyn/AAE333/FALL10/HOMEWORKS/HW13/XFLR5_v6.01_Beta_Win32(2)/Release/Guidelines.pdf", 2009. [Last accessed; 12/06/2014].

[21] S.S. Dodbele, C.P. van Dam, and P.M.H.W. Vijgen. *Nasa contract report 3970: Design of fuselage shapes for natural laminar flow*. NASA, 1986.

[22] Sighard F Hoerner. *Fluid-dynamic drag: practical information on aerodynamic drag and hydrodynamic resistance*. Hoerner Fluid Dynamics Midland Park, NJ, 1965.

[23] Th. Lutz and S. Wagner. *Numerical shape optimization of natural laminar flow bodies*. International Council of the Aeronautical Sciences and the American Institute of Aeronautics, Inc., 1998.

[24] Seif A.A. Zedan, M.F. and S. Al-Moufadi. *Drag reduction of airplane fuselages through shaping by the inverse method*. American Institute of Aeronautics and Astronautics, Inc., 1993.

[25] Jan Roskam. *Airplane design - Part III: Layout Design of Cockpit, Fuselage, Wing and Empennage: Cutaways and Inboard Profiles*. Roskam Aviation and Engineering Corporation, 1985.

[26] MX Aircraft. Mxs specifications. "http://www.mxaircraft.com/mxs-specifications.php", 2014. [Last accessed; 16/06/2014].

[27] AVCO Corporation. Enigne data 540 series engine. "http://www.lycoming.com/Lycoming/PRODUCTS/Engines/Certified/540Series/EngineData.aspx", 2014. [Last accessed; 17/06/2014].

[28] Marilyne Lino. Numerical investigation of propeller-wing interaction effects for a large military transport aircraft. "http://www.lr.tudelft.nl/fileadmin/Faculteit/LR/Organisatie/Afdelingen_en_Leerstoelen/Afdeling_AEWE/Aerodynamics/Contributor_Area/Secretary/M._Sc._theses/doc/Lino_100827_Thesis.pdf", 2010. [Last accessed; 16/06/2014].

[29] Sadraey M. Drag force and drag coefficient. "http://faculty.dwc.edu/sadraey/Chapter%203.%20Drag%20Force%20and%20its%20Coefficient.pdf", 2009. [Last accessed; 13/06/2014].

[30] Jan Roskam. *Airplane design - Part V: Component Weight Estimation*. Roskam Aviation and Engineering Corporation, 1985.

[31] JWR Taylor. *Jane's All The World's Aircraft*. Jane's Publishing Company, 1982.

[32] Dr.ir. Gianfranco La Rocca. Design of unconventional solutions for stability and control: V-tail and canard (addendum 2). AE3221-I - Systems Engineering and Aerospace Design. [Last accessed; 17/06/2014].

[33] Warren F. Phillips. *Mechanics of Flight*. John Wiley and Sons Inc., 2004.

[34] Snorri Gudmundsson. *General Aviation Aircraft Design: Applied Methods and Procedures*. Elsevier Inc., 2014.

[35] Blair B. Gloss. *The effect of canard leading-edge sweep and dihedral angle on the longitudinal and lateral aerodynamic characteristics of a close-coupled canard-wing configuration*. Langley Research Center, NASA, 1974.

[36] Jan Roskam. *Airplane design - Part II: Preliminary Configuration Design and Integration of the Propulsion System*. Roskam Aviation and Engineering Corporation, 1985.

[37] Jan Roskam. *Airplane design - Part VI: Preliminary Calculation of Aerodynamic, Thrust and Power Characteristics*. Roskam Aviation and Engineering Corporation, 1985.

[38] Chunyun Niu. *Airframe structural design: practical design information and data on aircraft structures*. Conmilit Press, 1988.

[39] RC Hibbeler. *Engineering Mechanics: Statics*. Prentice Hall, 2004.

[40] *CES EduPack 2013 version 12.2.13*. Granta Design Limited, 2008.

[41] M. Becker, R. Boersma, G. Datema, R. Grandia, A. Krikken, and J. Tuitert. *Simulation, verification and validation of aircraft wing structural analysis tool*. Technical University of Delft, 2014.

[42] United States Navy. *A-7 corsair pilot's flight operating manual*. Periscope film LLC, 2008.

[43] Red Bull GmbH. Final 4 results. `http://www.redbullairrace.com/en_US/article/final-4-results-abu-dhabi`, . [Last accessed; 19/06/2014].

[44] Gu P. Asiedu, Y. Product life cycle cost analysis: state of the art review. *International journal of production research*, 36 (4), 1998.

[45] Patrick O'Connor and Andre Kleyner. *Practical reliability engineering*. John Wiley & Sons, 2011.

[46] "Federal Aviation Administration". Faa registry - aircraft - make / model inquiry. `http://registry.faa.gov/aircraftinquiry/AcftRef_Inquiry.aspx`. [Last accessed; 18/06/2014].

[47] J.F. Jenck. Products and processes for a sustainable chemical industry: a review of achievements and prospects. *Royal Society of Chemistry*, 6(11), 2004.

[48] US environmental protection agency. Emission factors for synthetic fiber manufacturing. `http://www.epa.gov/ttnchie1/ap42/ch06/final/c06s09.pdf`. [Last accessed; 17/06/2014].

[49] The World Bank. Iron and steel manufacturing industry - pollution prevention guidelines. `http://www.environmental-expert.com/articles/iron-and-steel-manufacturing-industry-pollution-prevention-guidelines-13` [Last accessed; 17/06/2014].

[50] Pickering. S. Innovations in recycled carbon fibre for sustainable manufacturing. `http://www.nottingham.ac.uk/nimrc/research/sustainablemanufacturing/recycledcarbonfibre.aspx`. [Last accessed; 17/06/2014].

[51] B.S. et al MacDonald. Determination of sulfur in biodiesel by x-ray fluorescence spectroscopy. `http://www.astm.org/COMMIT/E48_MacDonald.pdf`. [Last accessed; 17/06/2014].

[52] Isidor Buchmann. The high power lithium-ion. `http://batteryuniversity.com/learn/article/the_high_power_lithium_ion`. [Last accessed; 29/06/2014].

[53] S.J. Pickering. Recycling technologies for thermoset composite materials current status. *Composites Part A: Applied Science and Manufacturing*, 37(8), 2006.

[54] Soraia Pimenta. Recycling carbon fibre reinforced polymers for structural applications: Technology review and market outlook. *Waste Management*, 31(2), 2011.

[55] JM Rankin and PR Mattson. Controller interface for controller-pilot data link communications. In *Digital Avionics Systems Conference, 1997. 16th DASC., AIAA/IEEE*, volume 2, pages 7–1. IEEE, 1997.

Appendix A - Complete list of requirements

This appendix contains the complete set of requirements used throughout the DSE. The main report does not contain all the requirements, as some were used only during the concept generation at an earlier design stage.

In appendix A the complete list of stakeholders and the corresponding requirements is displayed.

Table A.1: Stakeholder requirements

Stakeholders	**Requirements**
Aircraft industry	- The aircraft shall comply to all rules and regulations - The aircraft shall be safe and sustainable
Red Bull	- The competitive environment should be such that the competition is successful
Scientific community	- Publication of process, results and discoveries of the project shall be done according to scientific standards.
Media	- The aircraft shall be doing attracting manoeuvres - The aircraft shall be clearly visible
Red Bull Air Race	- The design shall comply with the Red Bull Air Race Regulations - The aircraft shall promote motorsports spirit
Competitors	- The aircraft shall have better performance characteristics than its competitors
Suppliers	- The products shall be ordered in time - The money for supplies has to be paid
Transport company	- The aircraft shall be able to withstand transport loads - The aircraft shall have the possibility to be transported
Customers	- The aircraft shall win the competition - The aircraft shall fall within cost limits
Airport	- The aircraft shall be able to land and take-off within the airport premises
General public	- The aircraft shall be visually and audibly appealing - The aircraft shall be safe to be observed from the race venue - The aircraft shall demonstrate good flying performance
Sponsors	- The aircraft shall obtain high ranking in the competition - The aircraft shall bear the sponsors' logo - The aircraft shall promote the image of the company
DSE group	- The DSE group shall improve engineering, communication and presentation skills - The DSE group shall learn to work as a team
TU Delft	- The DSE group shall apply their knowledge obtained during the bachelor studies in designing the aircraft - High quality report that follows guidelines and deadlines. - Sustainability shall be considered during the design process

The mission profile for one race in the Red Bull Air Race is shown below in Fig. A.1. Each phase is explained in more detail in Table A.2.

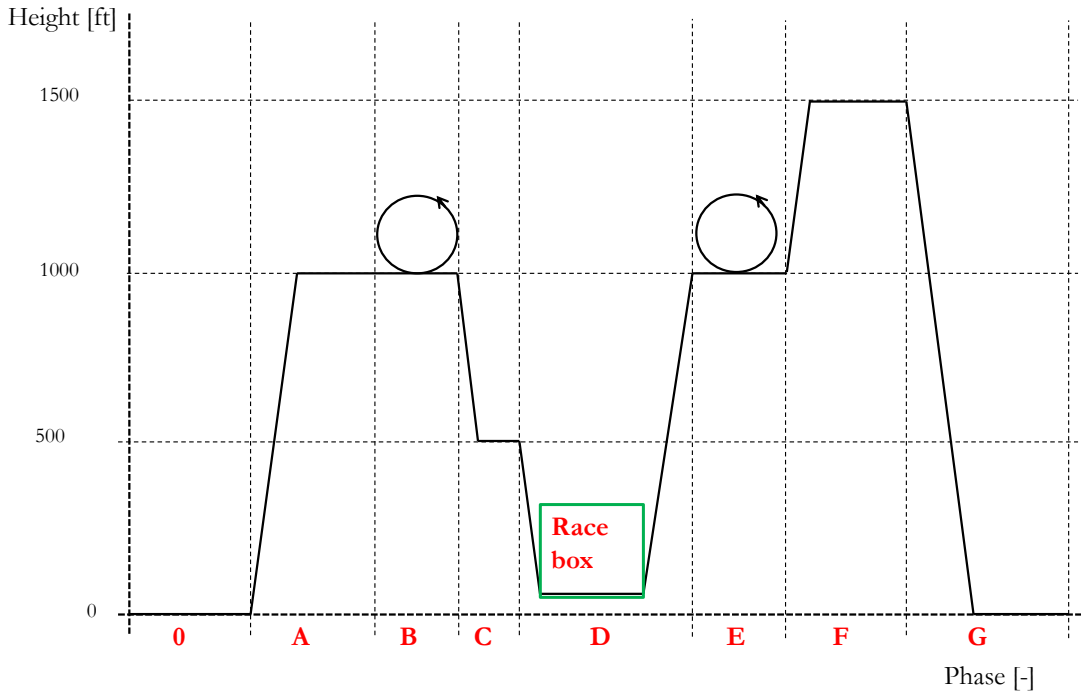

Figure A.1: Mission profile for an aerobatics racer

Table A.2: Mission profile for an aerobatic racer in the Red Bull air race conforming to the regulations of 2014 [1]

Phase	Action
0	Engine start-up and taxiing
A	Take-off and climb to 1000 [ft] and cruise to HOLD 1
B	HOLD 1
C	'30 seconds hold'(HOLD 2) last short hold just before the race
D	Fly to race Box; Immediately leave race box and climb to 1000 [ft]
E	and cruise to HOLD 3
F	Airport tower gave landing clearance; climb to 1500 [ft] and cruise to airport
G	Land aircraft; Engine shutdown

Additionally, a break down structure for the functions that need to be performed by the aircraft is presented in Fig. A.2.

All of the above is then used to generate the requirement discovery tree shown in Fig. A.3.

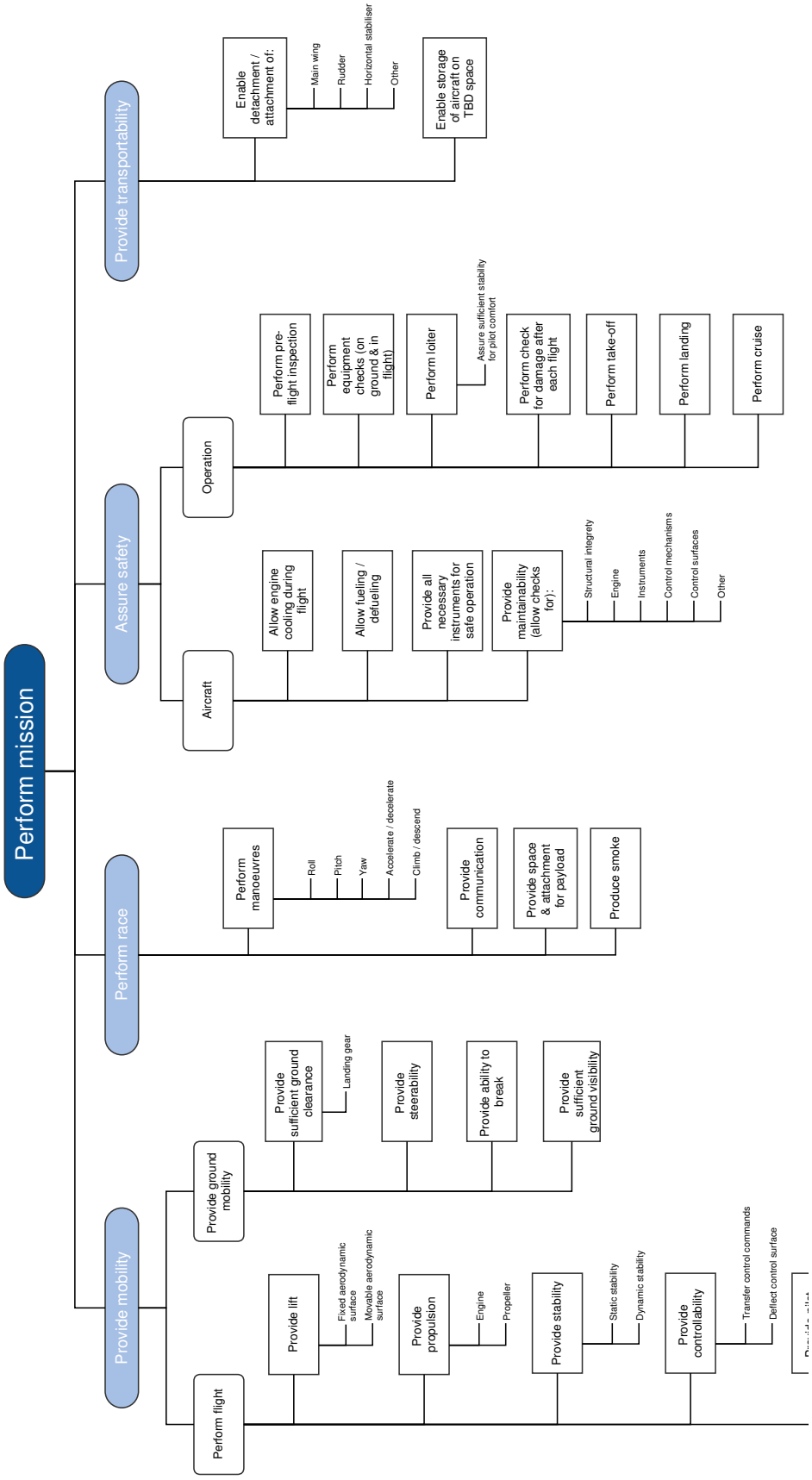

Figure A.2: Functional break down structure for a aerobatics race aircraft

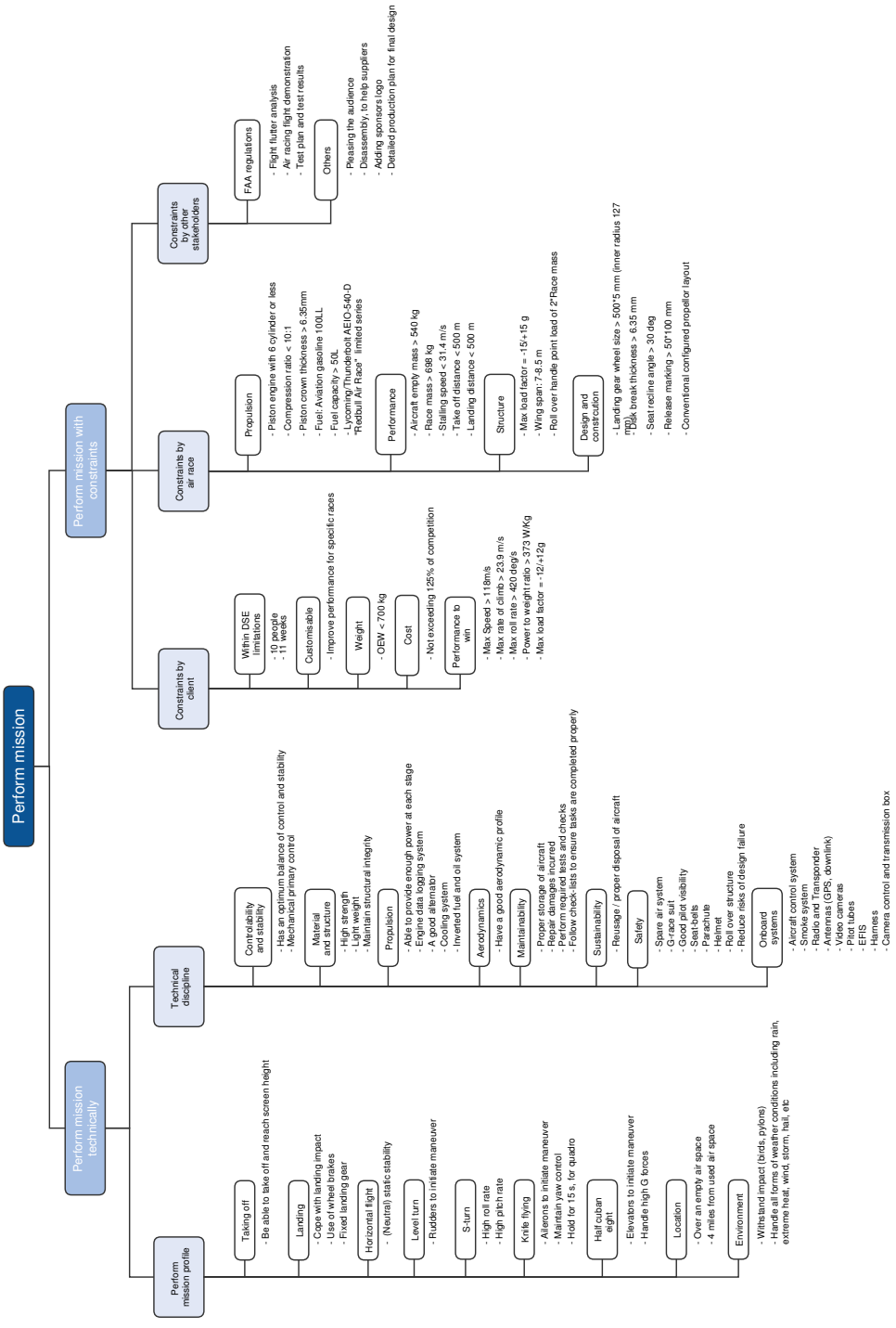

Figure A.3: Requirement discovery tree used for the generation of the requirements of the Avinya race aircraft.

Appendix B - 3D analysis polar graphs

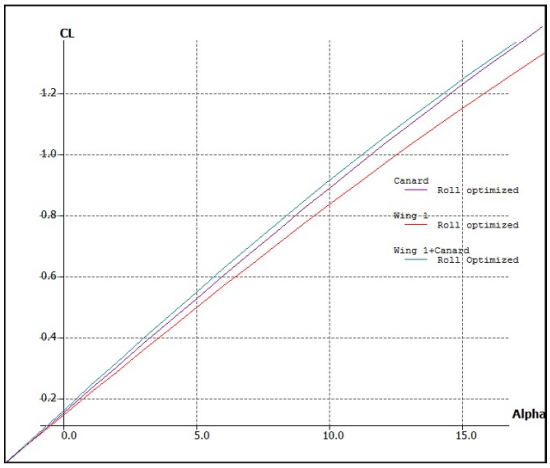

(a) C_L-α **curve**

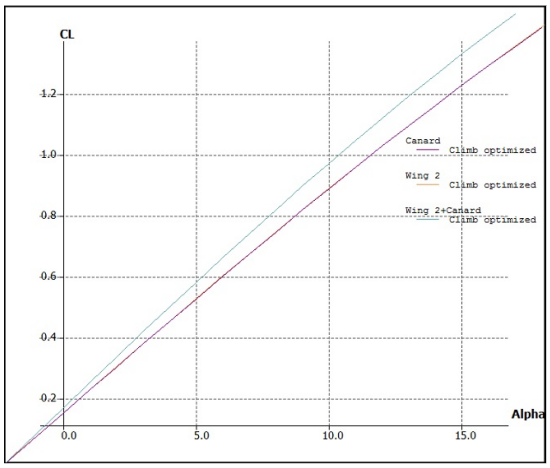

(b) C_L-α **curve**

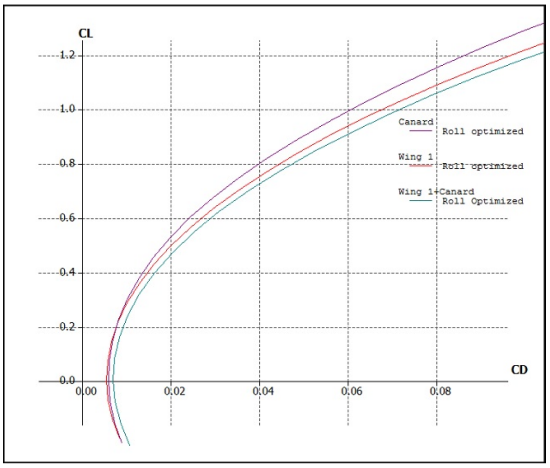

(c) Drag Polar

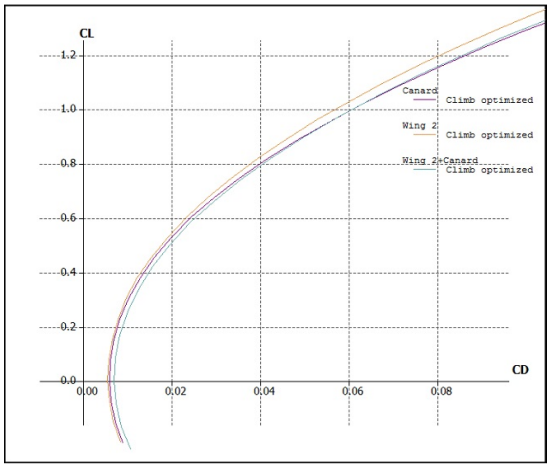

(d) Drag Polar

Figure B.1: Polar graphs for 3D analysis

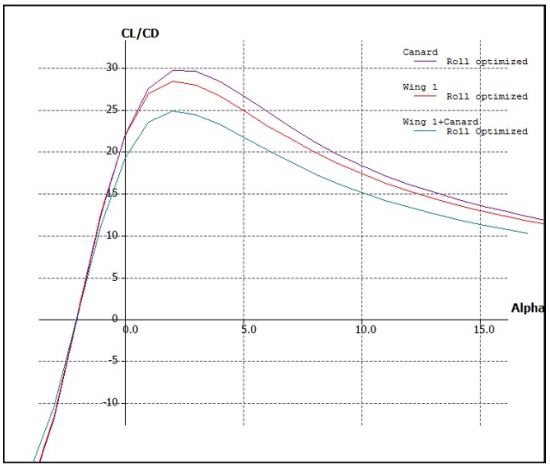

(e) L/D against α

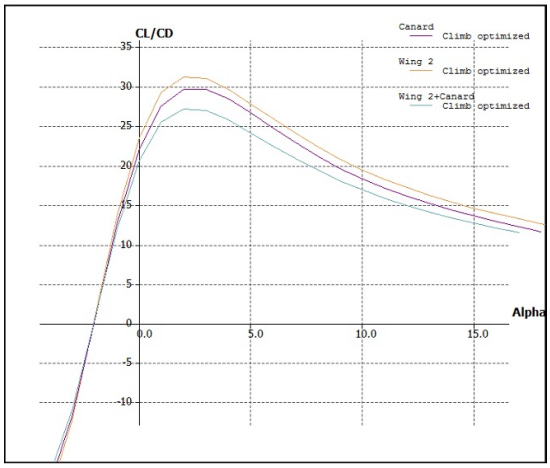

(f) L/D against α

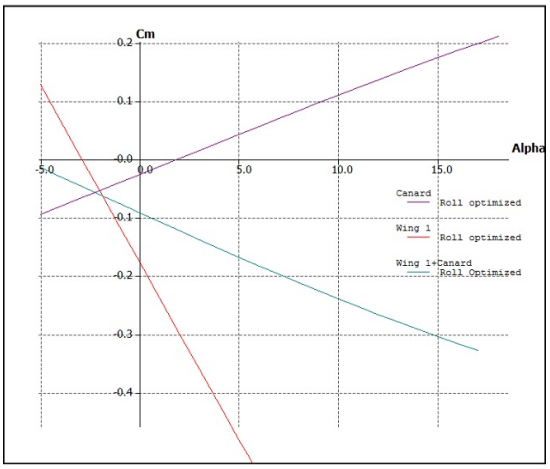

(g) C_m-α curve

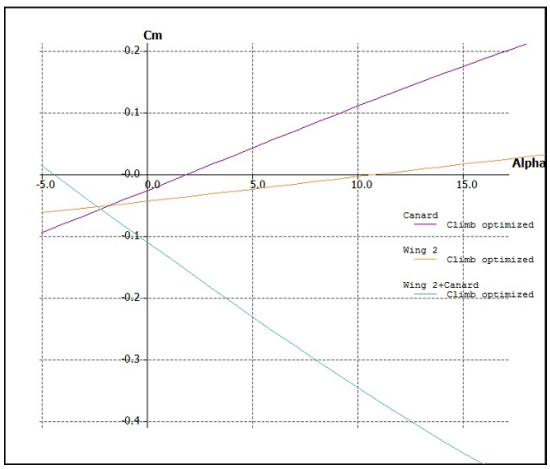

(h) C_m-α curve

Appendix C - Material characteristics

Several abbreviations are used in Table C.1, these are: *CF* for carbon fibre, *QI* for quasi-isotropic, *BA* for bi-axial, *Uni* for uni-directional, *deg* for degree, *Spec.* for specific, *c* and *comp.* for compressive, and *t* for tensile.

Table C.1: Characteristics of common aerospace materials

Material	Density ρ [kg/m^3]	Tensile modulus E_t [MPa]	Comp. modulus E_c [Mpa]	Tensile strength σ_t [Mpa]	Comp. strength σ_c [Mpa]
PEEK/IM carbon epoxy (67%) QI	1560	56600	56600	466.5	466.5
Epoxy/HS CF (62%) QI	1575	46200	46200	549.5	569.0
Epoxy/HS CF (62%) BA	1575	65700	60300	768.5	796.0
Epoxy/HS CF (62%) UNI 0 deg	1565	141500	127000	1955.0	1550.0
Aluminium 6061-T6	2700	71000	73600	270.0	248.5
Aluminium 7075-T6	2800	72500	76650	507.0	465.5
AISI Steel 4130	7850	118050	118050	812.5	702.5
Titanium Ti-6Al-4V annealed	4430	115000	118500	1031.0	964.0

Material	Spec. modulus (t) E_t/ρ [Mpa/kg]	Spec. modulus E_c/ρ [Mpa/kg]	Spec. strength (t) σ_t/ρ [Mpa/kg]	Spec. strength σ_c/ρ [Mpa/kg]	Spec. cost €$/kg$ [Euro/kg]
PEEK/IM carbon epoxy (67%) QI	36.28	36.28	0.299	0.299	94.65
Epoxy/HS CF (62%) QI	29.33	29.33	0.349	0.361	44.40
Epoxy/HS CF (62%) BA	41.71	38.29	0.488	0.505	44.40
Epoxy/HS CF (62%) UNI 0deg	90.42	81.15	1.249	0.990	31.45
Aluminium 6061-T6	26.30	27.26	0.100	0.092	2.00
Aluminium 7075-T6	25.89	27.38	0.181	0.166	2.07
AISI Steel 4130	15.04	15.04	0.104	0.089	0.50
Titanium Ti-6Al-4V annealed	25.96	26.75	0.233	0.218	20.90

Appendix D - Canard wingbox sizing

The results regarding calculated shear forces, moments, structural weight and geometry with respect to the sizing of the canard wingbox are shown here. The process and results as performed for the main wing, shown in chapters 10 and 11, is repeated for the canard, while taking into account the change in sweep, elevator, planform geometry and aerodynamic distributions.

The shear and moments as induced on the wing are shown in Fig. D.1, whereas the stresses as found after multiple iterations for a geometry as described in Table D.2 are shown in Table D.1.

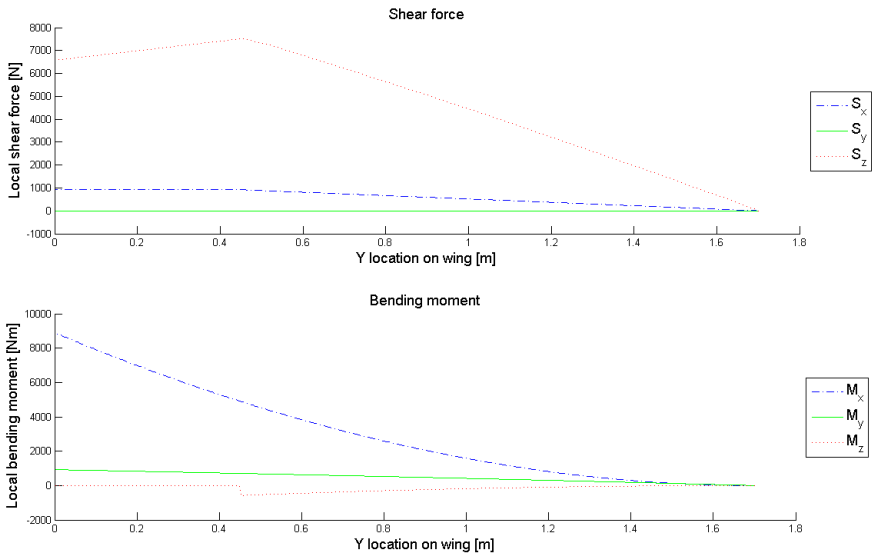

Figure D.1: Shear forces and moments induced along semi-wingspan of the wingbox of the canard

Table D.1: Maximum stresses present in canard wingbox

	Canard
Dimension	Value
Y_{max} [MPa]	302.48
σ_y [MPa]	$\pm$ 296.9
τ_{xz} [MPa]	-33.50

In Fig. D.2 the Von Mises stress as calculated along the wingbox of the canard is shown. One notices the gradually increasing stress distribution as result of moment arm and elevator deflection.

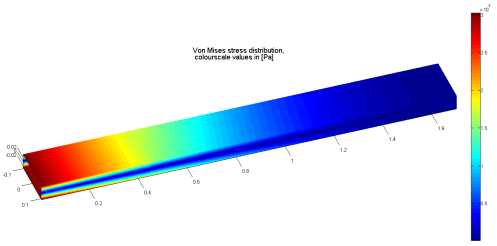

Figure D.2: Von Mises stress in wingbox of the canard with maximum deflection of elevator

Table D.2: Dimensions of the canard wingbox structure

Dimension	Canard
t_f	10.32
t_r	8.73
t_t	5.55
t_b	5.55
w_{root}	214.3
h_{root}	63.50
η	-3.56
ξ	0.00
X	-3.01
Z	0.00

The resulting cost and weight of the canard wingbox is shown in Table D.3, where one might notice the difference in calculated weight with respect to estimated in the class II estimation. The difference is both explained by the absence of skin weight and moments induced by sweep.

Table D.3: Weight and material cost of the canard wingbox structure

Dimension	Wing 1
$W_{wingbox}$ [kg]	9.55
$Cost_{wingbox}$ [€]	296.96

Appendix E - Detailed trajectory results

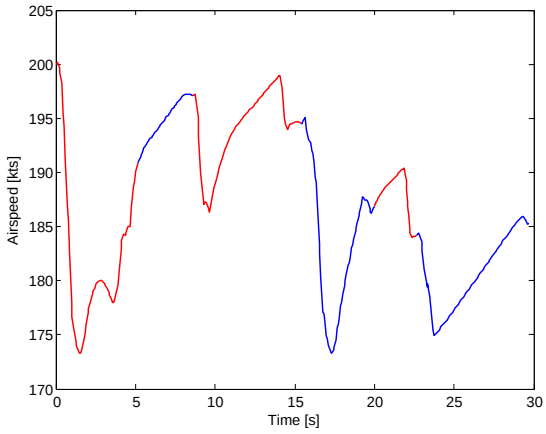

(a) Airspeed versus time

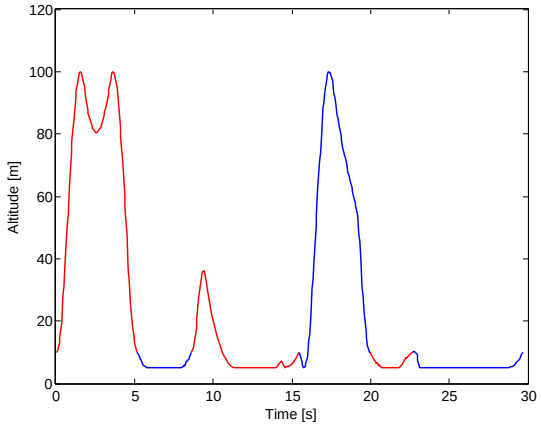

(b) Altitude versus time

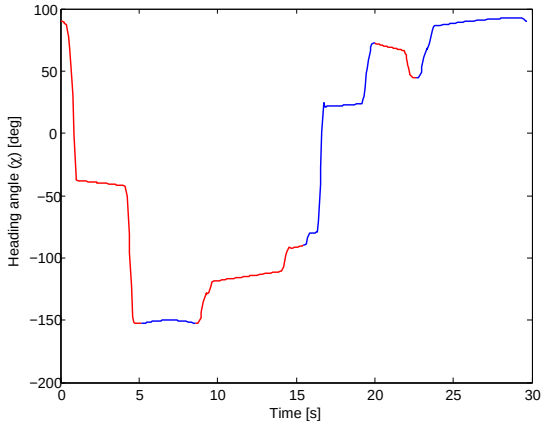

(c) Heading angle versus time

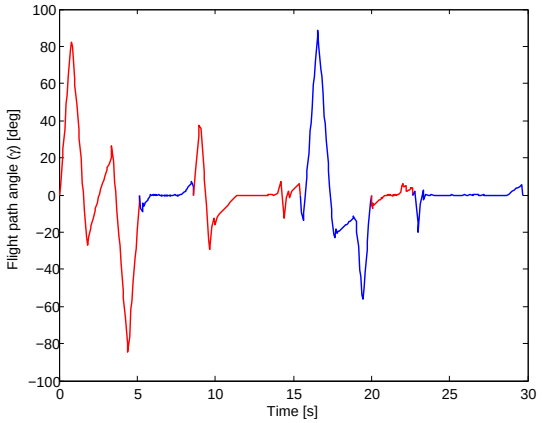

(d) Flight path angle versus time

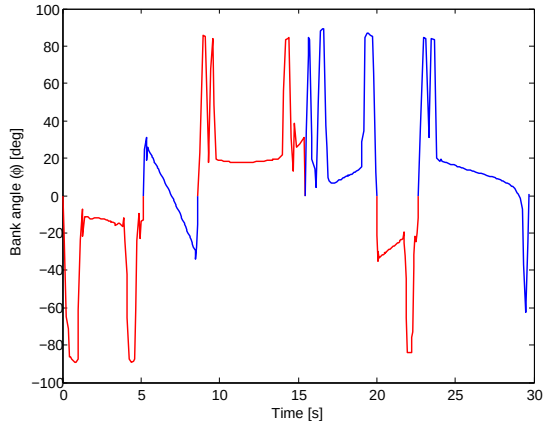

(e) Bank angle versus time

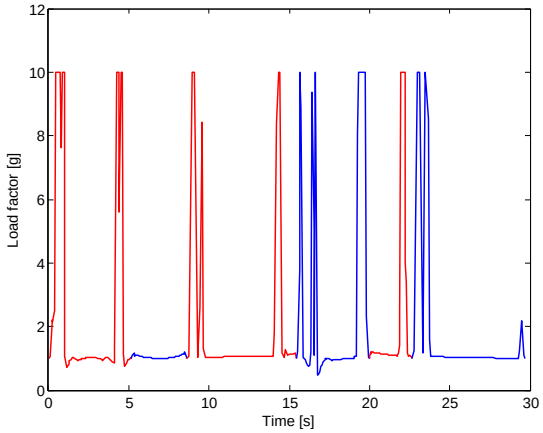

(f) Load factor versus time

Figure E.1: Sample track results for wing 1

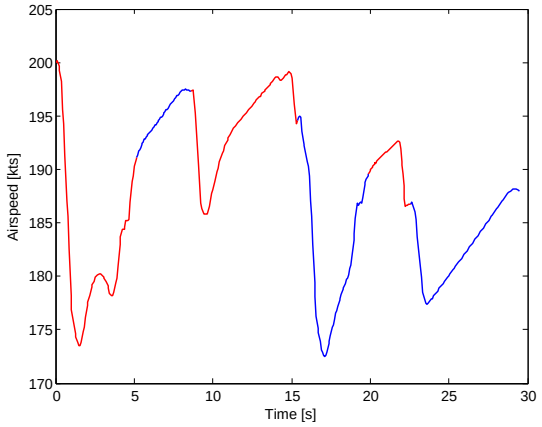

(a) Airspeed versus time

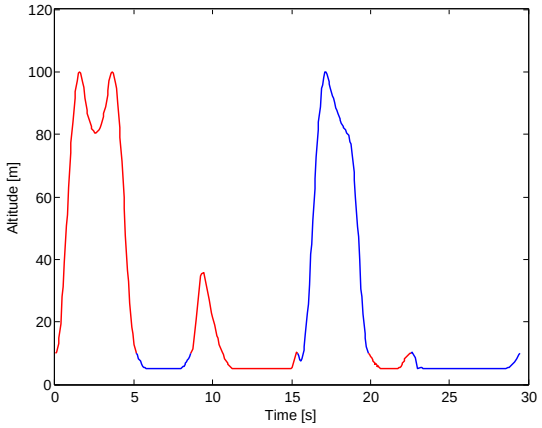

(b) Altitude versus time

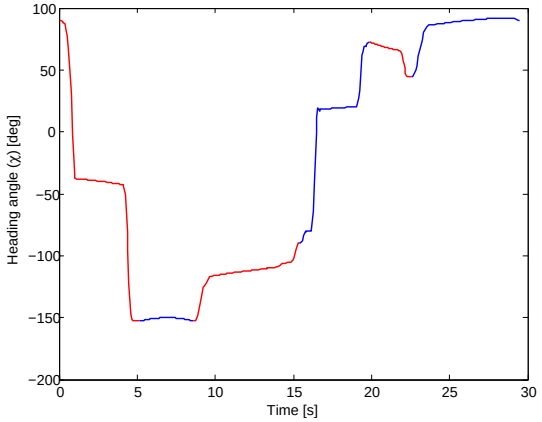

(c) Heading angle versus time

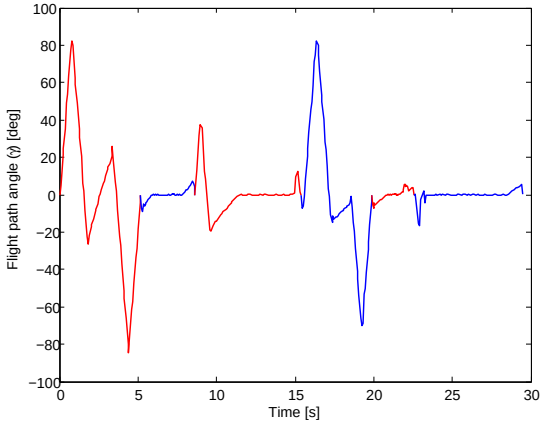

(d) Flight path angle versus time

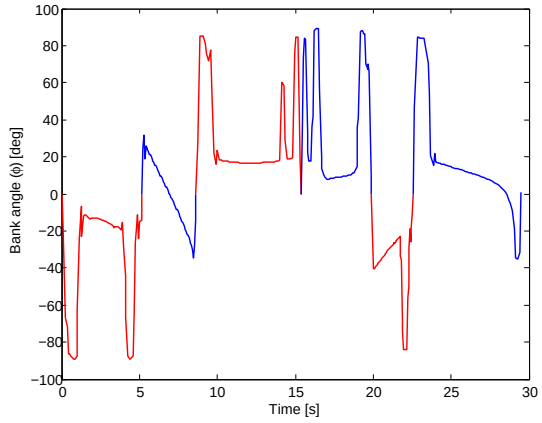

(e) Bank angle versus time

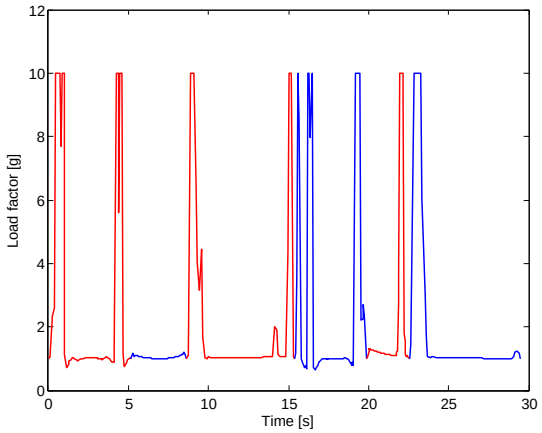

(f) Load factor versus time

Figure E.2: Sample track results for wing 2

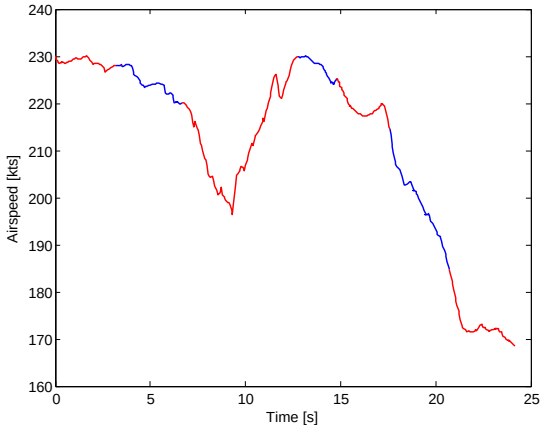

(a) Airspeed versus time

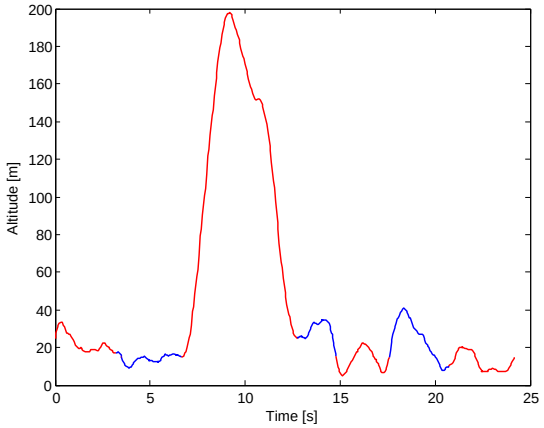

(b) Altitude versus time

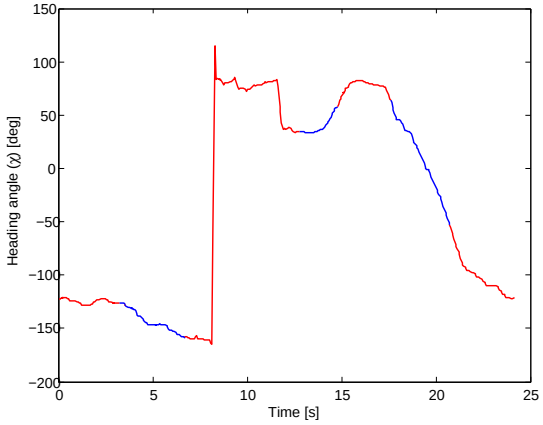

(c) Heading angle versus time

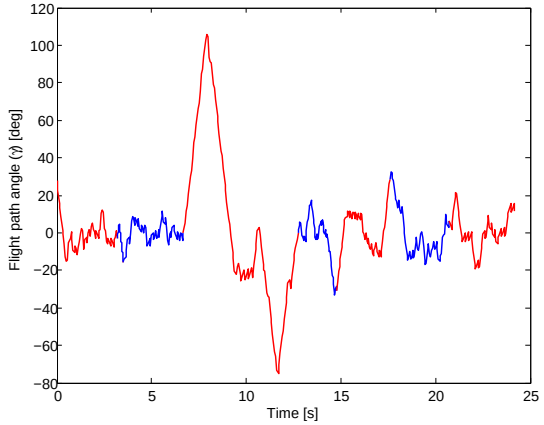

(d) Flight path angle versus time

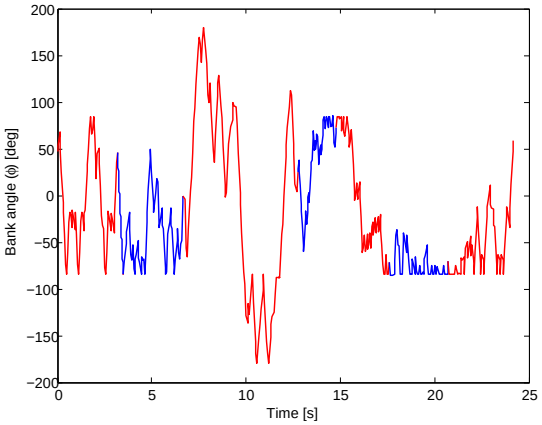

(e) Bank angle versus time

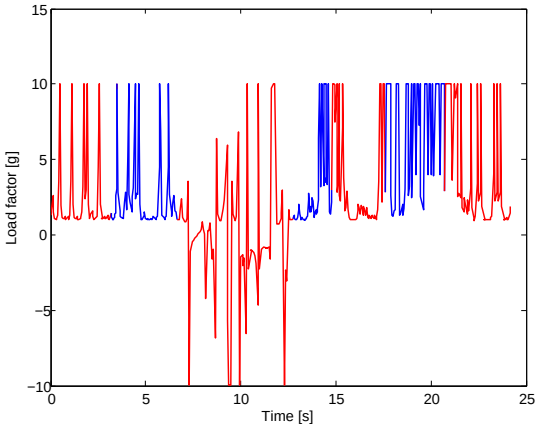

(f) Load factor versus time

Figure E.3: Abu Dhabi track results for wing 1

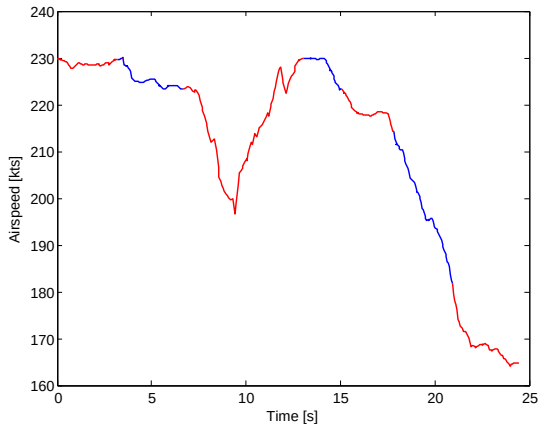

(a) Airspeed versus time

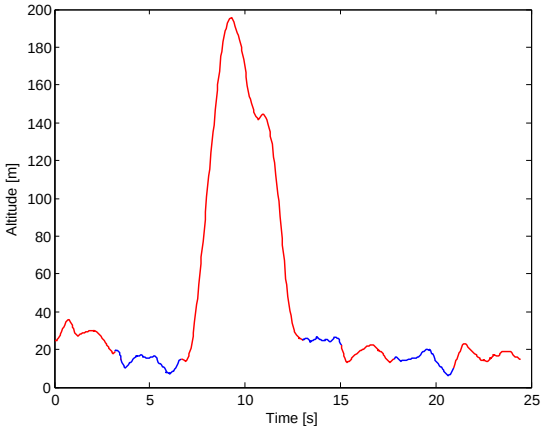

(b) Altitude versus time

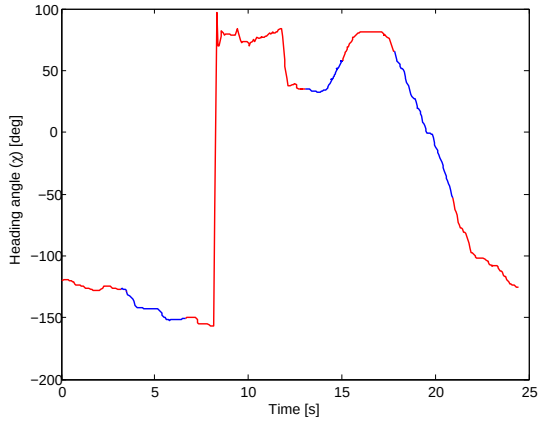

(c) Heading angle versus time

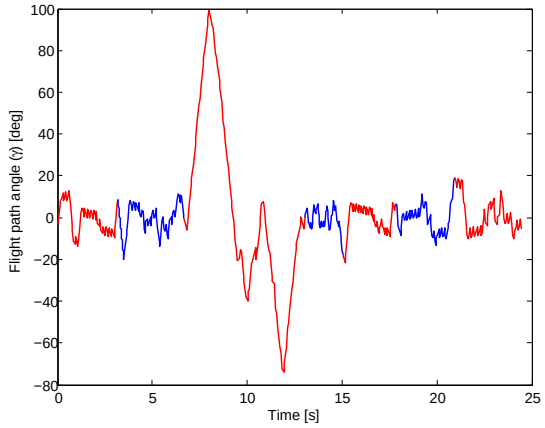

(d) Flight path angle versus time

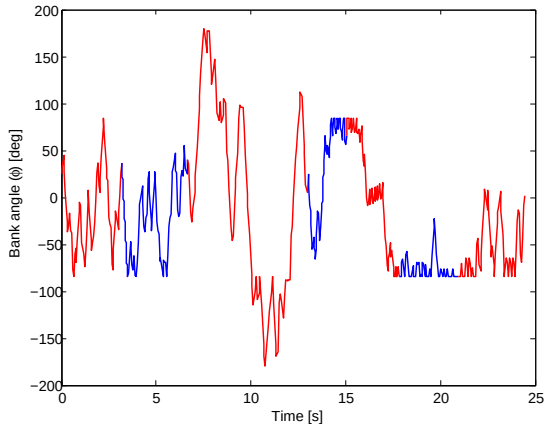

(e) Bank angle versus time

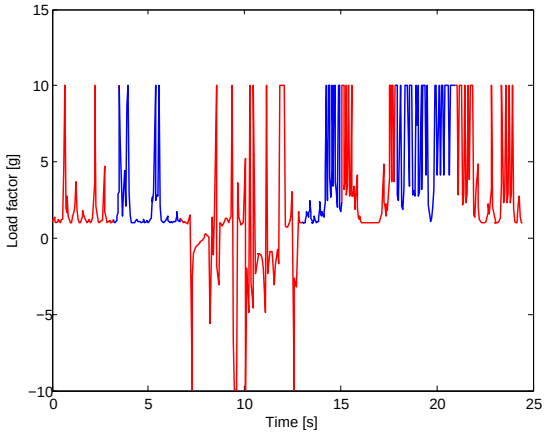

(f) Load factor versus time

Figure E.4: Adbu Dhabi track results for wing 2

Appendix F - Pilot Dimensions

Table 2.1 Dimensions and Weights for Male Crew Members as Shown in Figure 2.1

A	B	C	D	E	F	G	H	I	K	L
1,600	870	230	300	620	350	435	850	140	760	300
1,750	920	255	335	685	390	475	950	150	805	330
1,900	990	280	370	750	430	515	1,050	160	875	360

A	M	N	O	P	Q	R	S	T	U
1,600	300	50	200	190	260	80	25	20	20
1,750	325	60	220	200	270	90	30	30	20
1,900	350	70	240	210	280	100	30	30	20

Body width across shoulders: 533 mm, across elbows: 561 mm and across hips: 457 mm.

Body component weights are for a male pilot with a weight of 179.3 lbs.

Body Component	Number in Figure 2.1	Weight in lbs.
Head and neck	1	15.0
Upper torso	2	49.0
Lower torso	3	28.0
Upper legs	4	39.9
Lower legs and feet	5	29.8
Upper arms	6	9.9
Lower arms and hands	7	7.7
Total		179.3

Notes:

1. All dimensions in mm. (1 in.=25.4 mm.)
2. The c.g. of the 'upright' pilot of Figure 2.1 is at point P.
3. For pilot positions differing from the upright, the new c.g. can be computed with the help of the table to the left.
4. All weights include helmet and flight clothing.
5. For a female pilot multiply all weight data by 0.81.
6. Data source: Design Requirements for the RAF and RN (England).

Figure F.1: Dimensions and weights for male crew members as shown in Fig. 8.6 in subsection 8.3.2